Growth and Structure of DIP Thin-Films
and
Au Contacts on DIP Thin-Films

Von der Fakultät für Physik der Universität Stuttgart
zur Erlangung der Würde eines Doktors der
Naturwissenschaften (Dr. rer. nat.) genehmigte Abhandlung

Vorgelegt von Arndt Christian Dürr aus Frankfurt am Main

Hauptberichter: Prof. Dr. H. Dosch
Mitberichter: Prof. Dr. D. Schweitzer

Eingereicht am: 28. Juni 2002
Tag der mündlichen Prüfung: 15. Oktober 2002

Institut für Theoretische und Angewandte Physik der Universität Stuttgart

2002

Seht ihr den Mond dort stehen,
er ist nur halb zu sehen,
und ist doch rund und schön.
So sind auch manche Sachen,
die wir getrost belachen,
weil unsre Augen sie nicht sehn.

Matthias Claudius

Contents

Chapter 1

Deutsche Zusammenfassung

1.1 Motivation

Organische Materialien mit halbleitenden Eigenschaften erfahren zur Zeit wachsende Aufmerksamkeit auf Grund ihres Potentials als Material in einer Vielzahl von elektronischen und optoelektronischen Anwendungen. In den letzten Jahren wurden bereits Feldeffekttransistoren, Leuchtdioden und Solarzellen auf Basis organischer Halbleiter realisiert.

Viele organische Moleküle werden zur Herstellung von Halbleiterstrukturen verwendet. Dies wirft grundlegende physikalische Fragen über die Eigenschaften von dünnen Schichten solcher Moleküle auf. Zentraler Gegenstand dieser Fragen sind u.a. ihr Wachstumsverhalten, ihre kristallographische Struktur, sowie ihre elektrischen und optischen Eigenschaften. Besonderes Interesse wird dabei *planaren aromatischen Molekülen* entgegengebracht, zum Beispiel einigen Phthalocyaninen, Pentacen-Derivaten, oder Perylen-Derivaten. Ihr vergleichsweise geringes molekulares Gewicht, sowie ihre thermische Stabilität gegen Polymerisierung und Fragmentierung (je nach Molekül bis zu mehreren 100°C) erlauben Sublimation unter UHV-Bedingungen. Dadurch ergibt sich die Möglichkeit, dünne kristalline Schich-

ten dieser Moleküle mittels organischer Molekularstrahlepitaxie (OMBE) herzustellen, d.h. unter maximal kontrollierbaren und reproduzierbaren Wachstumsbedingungen.

1.2 Struktur und Wachstum von DIP-Schichten

Vor kurzem untersuchte Münch die Ladungsträgerbeweglichkeit in dünnen Filmen des planaren Perylen-Derivats Diindenoperylen (DIP). Bei der Charakterisierung der Filme an Laborröntgenquellen stellte sich heraus, dass dünne DIP-Filme eine hohe strukturelle Ordnung entlang der Probennormalen und sehr geringe Mosaizitäten aufweisen [1]. Obwohl die Herstellung einfach ist und DIP-Filme interessante elektrische und strukturelle Aspekte aufweisen, gibt es bis heute nur wenige systematische Studien über ihre physikalischen und strukturellen Eigenschaften.

Ein Ziel dieser Arbeit ist daher die systematische und detaillierte Untersuchung des Wachstumsverhaltens und der hohen strukturellen Ordnung dieser Schichten unter Verwendung *hochauflösender* Röntgenstreuung an Synchrotronquellen. Eine quantitative Analyse der Röntgendaten ermöglicht Einblicke sowohl in den Wachstumsmechanismus als auch in die Schichtdickenabhängigkeit der out-of-plane Struktur.

1.2.1 Struktur und Thermisches Verhalten

Probenherstellung

Im Hinblick auf die Untersuchung der Struktur und des thermischen Verhaltens dünner DIP-Filme wurden zunächst DIP-Schichten verschiedener Dicke (ca. 70 Å bis ca. 9000 Å) bei stets gleicher Substrattemperatur (145°C) und

gleicher Rate (12 Å/min) auf thermisch oxidierten (4000 Å Oxid) Siliziumsubstraten, außerdem auf Saphirsubstraten mit $(11\bar{2}0)$-Orientierung, im UHV ($p \leq 2 \times 10^{-9}$ mbar) hergestellt.

I – Detaillierte Bestimmung der DIP-Elektronendichte entlang der Probennormalen, $\rho_{el}(z)$, mit Hilfe der Master-Formel

Einige dieser Proben wurden an der europäischen Synchrotronquelle ESRF in Grenoble mittels spekulärer Röntgenstreuung charakterisiert, wobei Bragg-Reflexe der DIP-Schichten bis zur 9. Ordnung (d.h. $q_z \approx 3.5$ Å^{-1}) gemessen wurden. Die Auswertung der gemessenen Daten erfolgte mit Hilfe eines semikinematischen Streumodells. Dieses erlaubt die Anpassung der gemessenen Daten über den gesamten q_z-Bereich, wobei Interferenzerscheinungen zwischen der vom Substrat- und der vom DIP-Film gestreuten Röntgenwelle ausgenutzt werden, um das Phasenproblem in der Röntgenstreuung (teilweise) zu umgehen. Auf diese Weise wurde die Elektronendichte unterschiedlich dicker DIP-Schichten entlang der Probennormalen ($\rho_{el,DIP}(z)$) mit hoher Präzision bestimmt.

Weitere strukturelle Informationen der dünnen Schichten wurden in TEM- und AFM-Messungen gewonnen. Ellipsometrische Untersuchungen lieferten Daten zur optischen Bandlücke der halbleitenden DIP-Schichten (Abschnitt 7.1).

II – Temperaturverhalten der DIP out-of-plane Struktur

Ein wichtiger Aspekt im Hinblick auf technologische Anwendungen ist die thermische Stabilität der dünnen funktionalen Schichten, sowie die Frage nach dem thermischen Ausdehnungskoeffizienten. Beide Punkte sind für die Anwendung von organischen Molekülen in Halbleiterelementen relevant, zum einen hinsichtlich der maximalen Betriebstemperature, zum an-

deren, weil eine stark unterschiedliche thermische Ausdehnung die Funktion und damit die Lebensdauer metall-organischer Kontakte beeinträchtigen kann. Deshalb wurde die thermische Stabilität von DIP-Schichten, ihr Ausdehnungskoeffizient entlang der Probennormalen, sowie ihr Desorptionsverhalten an einigen Proben mittels Röntgenstreuung untersucht (am Hamburger Synchrotron-Labor HASYLAB).

III – Röntgenmessungen unter streifendem Einfall und Ellipsometriemessungen zur Bestimmung von in-plane Gitterkonstanten

Um die in-plane Struktur von DIP-Schichten zu bestimmen, wurden ergänzende Messungen mittels Braggstreuung unter streifendem Einfall (GID) an hauseigenen Röntgenquellen durchgeführt. Der Schwerpunkt dieser Untersuchungen lag dabei auf DIP-Schichten, die auf orientierten (Saphir-) Substraten aufgewachsen worden sind. Zusätzlich wurden zwei auf Saphirsubstraten gewachsene DIP-Schichten in unterschiedlichen azimuthalen Orientierungen mit Hilfe von Ellipsometrie gemessen.

Ergebnisse

Im Folgenden werden die Ergebnisse zu den oben unter I–III angeführten Strukturuntersuchungen beschrieben.

I – Allgemeine (strukturelle) Ergebnisse und detaillierte Ergebnisse von der DIP-Elektronendichte $\rho_{el}(z)$

- Die allgemeinen strukturellen Eigenschaften der im Rahmen dieser Arbeit hergestellten DIP-Filme zeichnen sich durch eine für organische Dünnschichtsysteme ungewöhnlich geringe Mosaizität aus, die bei allen Proben deutlich unter 0.015° lag und in den besten Filmen

nur 0.0087° betrug. Die Größe der Mosaizität scheint dabei durch die Welligkeit des Substrats geprägt zu sein. Der hohe Ordnungsgrad in den Schichten wurde sowohl in spekulärer Röntgenstreuung als auch in Querschnitts-TEM-Messungen nachgewiesen. Besonders deutlich zeigt sich der hohe Ordnungsgrad in den TEM-Bildern, in denen einzelne DIP-Monolagen als hell-dunkle Streifenpaare abgezählt werden können. Die Röntgenspektren zeigen im Bereich kleiner Winkel ausgeprägte Kiessig-Interferenzen (aus denen sich die Gesamtschichtdicke D_{DIP} ergibt). Spekuläre DIP Bragg-Reflexe bis zur 9. Ordnung weisen auch hier auf die hohe kristalline Ordnung im Film hin. Um die Bragg-Reflexe herum sind ausgeprägte Laue-Oszillationen zu erkennen, die auf eine lateral homogene kohärente Schichtdicke (D_{coh}) schließen lassen. Aus den Röntgenspektren ergibt sich eine out-of-plane Gitterkonstante von $d_{DIP} \approx 16.5$ Å. Ein Vergleich der Periodizitäten der Laue-Oszillationen und der Kiessig-Interferenzen offenbart, dass die DIP-Filme über ihre gesamte Schichtdicke kristallin geordnet sind ($D_{DIP} = D_{coh}$). AFM-Messungen an den DIP-Filmen zeigen große flache Terrassen mit Längen bis zu mehreren 100 nm, die durch monomolekulare Stufen der Höhe 16.5 Å voneinander getrennt sind. Zusätzlich wurde die optische Bandlücke durch Ellipsometrie zu $E_{g\,,\,opt.} = 2.2 \pm 0.1$ eV bestimmt[1].

- Die Analyse der spekulären Röntgendaten mit Hilfe des semikinematischen Streumodells ergibt, dass die Gitterkonstante d_{DIP} mit zunehmender Schichtdicke bis $D_{DIP} \approx 670$ Å abnimmt und dann bei $d_{DIP} = 16.56 \pm 0.02$ Å konstant bleibt. Die relative Abnahme der Gitterkonstante von $D_{DIP} = 126$ Å bis $D_{DIP} = 670$ Å beträgt 0.54%.

[1] In Kooperation mit M. I. Alonso und M. Garriga, Institut de Ciencia de Materials de Barcelona, CSIC, 08193 Bellaterra, Spanien.

- Weiterhin wurde festgestellt, dass die mittlere Elektronendichte $\rho^0_{DIP}(z)$ im DIP-Film mit zunehmender Schichtdicke bis $D_{DIP} \approx 400$ Å ansteigt und anschließend mit $\rho^0_{DIP}(z) = 0.39$ el/Å^{-3} konstant bleibt. Da das Produkt $d_{DIP} \times \rho^0_{DIP}(z)$ als Funktion der Schichtdicke nicht konstant ist, muss eine Änderung in der in-plane Struktur für $D_{DIP} \gtrsim 400$ Å angenommen werden.

- Die oszillierende Elektronendichte im DIP-Film entlang der Probennormalen ($\rho_{DIP}(z)$) konnte mit großer Präzision bestimmt werden. Hierbei wurde $\rho_{DIP}(z)$ als Fourier-Reihe dargestellt, wobei die Fourieramplituden durch die Intensität der DIP Bragg-Reflexe gegeben sind und die Fourierphasen sich in Folge der Spiegelsymmetrie des DIP-Moleküls auf Fouriervorzeichen (+ oder -) zurückführen lassen. Es stellte sich heraus, dass die Elektronendichte $\rho_{DIP}(z)$ mit der Periodizität der Gitterkonstanten um den Wert ρ^0_{DIP} oszilliert und dass der Elektronendichtekontrast $\rho^{max}_{DIP}/\rho^{min}_{DIP}$ je nach Schichtdicke einen Wert bis zu 1.9 annimmt. Dieser hohe Wert erklärt auch, warum in TEM-Bildern überhaupt einzelne DIP-Monolagen sichtbar sind.

II – Ergebnisse des Temperaturverhaltens der out-of-plane Struktur

- DIP-Filme weisen eine thermische Stabilität bis $T = 155°\text{C} \pm 10°\text{C}$ auf. Höhere Temperaturen führen zur lateral homogenen Desorption des Films (z.B. durch einen Lage-für-Lage-Prozess). Letzteres konnte durch den Vergleich der Intensität des ersten DIP Bragg-Reflexes mit der kohärenten Schichtdicke und der Gesamtschichtdicke in Abhängigkeit von der Anlass-Temperatur nachgewiesen werden: alle drei Größen nehmen für $T > 150°\text{C}$ bei konstanter Mosaizität gleichmäßig ab.

- Der thermische Ausdehnungskoeffizient parallel zur Molekülebene

(d.h.: senkrecht zur Substratoberfläche bedingt durch die (annähernd) aufrecht stehenden Moleküle) beträgt im Temperaturintervall der thermischen Stabilität (Raumtemperatur bis $T \approx 160°C$) $\alpha_{\parallel} = (75.8 \pm 4.5) \times 10^{-6}$ 1/K. Für den thermischen Ausdehnungskoeffizienten senkrecht zur Molekülebene (d.h.: parallel zur Substratoberfläche) wird auf Grund theoretischer Überlegungen und experimenteller Daten an ähnlichen Molekülsystemen ein zwei- bis vierfach höherer Wert erwartet; allerdings liegen für $\alpha_{\perp}$(DIP) keine Messdaten vor.

- Werden die DIP-Filme Temperaturen $T \geq 160°C$ ausgesetzt, so sind zwei irreversible Strukturänderungen zu beobachten. Die erste Änderung ereignet sich für $160°C \leq T \leq 200°C$. In diesem Temperaturintervall steigt der Wert der Gitterkonstanten d_{DIP} zunächst langsamer an als durch $\alpha_{\parallel}$ beschrieben und sättigt schließlich trotz steigender Temperaturen. Eine weitere Temperaturerhöhung resultiert in einer zweiten Strukturänderung, die sowohl von einem rasanten Anstieg der Desorptionsrate begleitet wird als auch von einer drastischen Zunahme der Gitterkonstante. In diesem Temperaturbereich erreicht der thermische Ausdehnungskoeffizient Werte von $\alpha_{\parallel} = 1100 \times 10^{-6}$ 1/K. Er gleicht damit Werten, die an organischen Molekülkristallen aus Alkylketten in der Nähe eines Phasenübergangs beobachtet wurden.

- Die Desorptionsrate bei $T = 195°C$ konnte durch Auswertung der Oszillationsperiode der Laue-Oszillationen in Abhängigkeit von der Zeit abgeschätzt werden. Sie beträgt ungefähr 1 ML/min (Monolage/min).

III – Ergebnisse der in-plane Struktur

- Alle untersuchten DIP-Filme sowohl auf amorphen SiO_2-Substraten als auch auf orientierten Saphiroberflächen zeigen Bragg-Reflexe, die eindeutig der DIP-Schicht zugeordnet werden können. Diese Reflexe liegen

bei

(i) $q_{\|} \approx 1.47$ Å^{-1} ($d_{\|} \approx 4.28$ Å)

(ii) $q_{\|} \approx 1.715$ Å^{-1} ($d_{\|} \approx 3.65$ Å).

- Einer der DIP-Filme auf einem Saphirsubstrat zeigte bei diesen Impulsüberträgen azimuthale Orientierung, die auf eine Domänenstruktur mit mindestens 4 Domänen hinweist. Ellipsometriemessungen an diesem Film ergaben ebenfalls eine (schwache) azimuthale Anisotropie. Ein weiterer DIP-Film auf einem Saphirsubstrat zeigte in Ellipsometriemessungen sogar eine ausgeprägte azimuthale Anisotropie, die auf eine Ausrichtung der Moleküle auf die Hauptachsen des Substrats hindeuten.

1.2.2 Wachstumsverhalten und Skalenexponenten

Um das Entstehungsverhalten sowohl von Dünnschichtstrukturen als auch der Probenmorphologie zu verstehen, ist es notwendig, den zugrundeliegenden Wachstumsprozess zu kennen. Neben atomistischen Wachstumsmodellen, die Monte-Carlo Simulationen heranziehen, um die Entwicklung der Dünnschichtmorphologie zu beschreiben, hat sich in den letzten zwei Jahrzehnten ein Ansatz zur statistischen Beschreibung des Wachstumsverhaltens etabliert. Hierbei wird der Wachstumsprozess mit Hilfe von Kontinuumsmodellen beschrieben, die zur Charakterisierung unterschiedlicher Wachstumsszenarien durch einen Satz 'universeller' Skalenexponenten, α, β und $1/z$ führen. Das zugrundeliegende Konzept geht davon aus, dass die Oberfläche der dünnen Schichten ein selbstaffines Verhalten aufweist, d.h. dass insbesondere die Oberflächenrauhigkeit σ als Funktion der untersuchten lateralen Längenskala L und der Schichtdicke D gegeben ist (siehe z.B. Refs. [2, 3]):

$$\sigma(L,D) \sim \begin{cases} L^{\alpha} & \text{für} \quad D \gg cL^{\alpha/\beta} \\ D^{\beta} & \text{für} \quad D < cL^{\alpha/\beta} \end{cases} \tag{1.1}$$

c bezeichnet eine Proportionalitätskonstante.

Der 'inverse dynamische' Skalenexponent, $1/z$, entspricht dem Quotienten β/α.

Obwohl 'kleinen' halbleitenden organischen Molekülen eine große Bedeutung für den Einsatz in zukünftigen Halbleiterbauteilen zukommt und viele Studien zur Struktur organischer Dünnschichtsysteme existieren, gibt es bis heute nur sehr wenige Studien, die den Wachstumsprozess organischer Schichten im Rahmen der Theorie selbstaffiner Oberflächen mit Skalenexponenten untersucht haben (z.B. Refs. [4–7]).

Eine weitere Zielsetzung dieser Arbeit war daher die Bestimmung der Skalenexponenten α, β und $1/z$ für DIP-Schichten.

Methoden

Zur Bestimmung der oben aufgeführten Skalenexponenten wurde an den bereits zur Bestimmung von $\rho_{el,DIP}(z)$ verwendeten Proben neben der spekulären Röntgenreflektivität zusätzlich die diffuse Röntgenstreuung (an der ESRF) in Rockingscans gemessen. Ferner wurde die Oberflächenmorphologie einzelner Proben (70 Å $\leq D \leq$ 9000 Å) mit Non-Contact-AFM bestimmt.

Die statistische Auswertung der AFM-Bilder mittels der Höhen-Differenz-Korrelationsfunktion $g(R)$ ermöglicht die **Bestimmung von** α. Darüber hinaus lässt sich α bestimmen durch die Anpassung der diffusen Streudaten im Rahmen der dynamischen Streutheorie (Distorted Wave Born Approximation, DWBA), die zuerst von Sinha *et al.* beschrieben wurde [8]. Die Anpassung der diffusen Streudaten erlaubt ferner die **Bestimmung von** $1/z$. Der Skalenexponent β **ergibt sich aus** der Steigung eines linearen Fits an eine

log-log Auftragung der Rauhigkeit σ gegen die Schichtdicke D_{DIP}, wobei in dieser Arbeit σ über einen ungewöhnlich großen Bereich von Schichtdicken ermittelt wurde. Die Rauhigkeit der Proben mit $D_{DIP} \leq 1100$ Å wurde durch Auswertung der Röntgenreflektivität bestimmt, für die Probe 'o9000' mit $D_{DIP} = 9000$ Å durch Auswertung mehrerer AFM-Bilder.

Ergebnisse

- Die Skalenexponenten für DIP-Schichten, die im UHV auf SiO_2-Substraten mit einer Rate von $R = 12$ Å/min und bei einer Substrattemperatur $T_{Sub} = 145°C \pm 5°C$ hergestellt wurden, betragen $\alpha_{mean} = 0.684 \pm 0.06$, $\beta = 0.748 \pm 0.05$, $1/z = 0.92 \pm 0.20$. Die Beziehung $1/z = \beta/\alpha$ ist mit diesen unabhängig voneinander bestimmten Werten innerhalb der Fehlergrenzen erfüllt. Zur Bestimmung von β wurde ein vergleichsweise großer Bereich an Schichtdicken verwendet ($69\,\text{Å} \leq D_{DIP} \leq 9000\,\text{Å}$).

- Der Wert von $\beta = 0.748 \pm 0.05$ übersteigt das theoretische Limit für ballistische Deposition ('random deposition'), $\beta_{RD} \leq 0.5$. Das einzige Modell, das ein 'rapid roughening' mit größeren Werten für β beschreibt, beinhaltet zufällige räumliche Inhomogenitäten in der lokalen Wachstumsrate. Als Erklärung für eine laterale Inhomogenität der Wachtumsrate wird die Ausbildung sogenannter 'tilt-Domänen' (dt.: Kippwinkel-Domänen) vorgeschlagen: In Analogie zu epitaktischem Wachstum bei anorganischen Filmen erwartet man die Ausbildung zweidimensionaler Inseln in der ersten Monolage. Die hier verwendeten Moleküle zeigen jedoch eine ausgeprägte Formanisotropie und stehen annähernd senkrecht auf dem Substrat (die Abweichung von der Senkrechten wird durch einen Kippvektor mit Kippwinkel ϕ beschrieben). Man kann erwarten, dass die in der Ebene liegende Kom-

ponente des Kippvektors in jeder Insel konstant ist, sich aber von Insel zu Insel unterscheidet. Wenn sich die beim Zusammentreffen zweier Inseln entstehenden zweidimensionalen Korngrenzen in die nachfolgenden Moleküllagen fortsetzen, könnte das zu den geforderten lateralen Inhomogenitäten in der lokalen Wachstumsrate führen.

1.3 Das Metall-Organische Heterosystem Au/DIP

Neben einer hohen Ladungsträgerbeweglichkeit in der organischen Schicht ist die zuverlässige Funktion des Kontakts zwischen Metall und organischer Schicht von großer Bedeutung für die Leistungsfähigkeit 'organischer' Halbleiterbauteile. Daher ist das Verständnis sowohl der Morphologie an der metall-organischen Grenzschicht als auch ihrer thermischen Stabilität sehr wichtig. Allerdings gibt es bisher nur wenige Untersuchungen an metall-organischen Grenzflächen. Die meisten wurden an ungeordneten Polymeren durchgeführt, die als Material mit geringer Dielektrizitätskonstante eine große Bedeutung im Herstellungsprozess herkömmlicher Mikroelektronik gewonnen haben [9–11]. Außerdem gibt es einige Untersuchungen an Langmuir-Blodgett-Filmen [12] und an dünnen Filmen von 'kleinen' organischen Molekülen, die mittels OMBE im UHV aufgewachsen wurden [13].

Im Rahmen dieser Arbeit wird die Grenzfläche zwischen Gold und dünnen DIP-Schichten als Modell-System für Metallkontakte auf organischen Halbleiterbauteilen untersucht. Dies erfolgte sowohl unmittelbar nach Deposition des Gold-Films ('as grown'), als auch während und nach einer Temperprozedur.

Hierbei wurde DIP als organisches Material verwendet, weil die Oberfläche der DIP-Schichten große (bis zu mehreren 100 nm Länge) flache

Terrassen mit monomolekularen Stufen aufweist. Diese Morphologie ist ideal geeignet, um die Grenzflächenstruktur von Metallkontakten auf organischen dünnen Schichten zu untersuchen. Darüber hinaus weisen die DIP Schichten eine sehr hohe strukturelle Ordnung und, damit verbunden, vergleichsweise hohe Ladungsträgerbeweglichkeiten von bis zu $\mu = 0.1$ cm^2/Vs auf. Damit sind DIP-Schichten auch sehr gut für den Einsatz in organischen Halbleiterbauteilen geeignet.

Gold wird häufig verwendet, um organische Halbleiterelemente zu kontaktieren. Zudem ist Gold hochgradig inert, wodurch chemische Verbindungen an der Gold-DIP Grenzfläche nur eine kleine Rolle spielen dürften. Zur Untersuchung der 'as grown'-Grenzflächenmorphologie kann daher das Augenmerk auf den Einfluss der Parameter Substrattemperatur und Wachstumsrate des Goldes gerichtet werden. Die Temperstudien sind insbesondere wichtig, um die Frage nach der thermischen Stabilität organischer Halbleiterelemente gegenüber erhöhten Betriebstemperaturen zu untersuchen.

Probenherstellung

Für die Untersuchung der oben genannten Fragestellungen wurden Goldfilme ($D_{Au} \approx 120$ Å) bei unterschiedlichen Wachstumsparametern im UHV auf wohldefinierte DIP-Schichten aufgebracht (Schichtdicke $D_{DIP} \approx 380$ Å, Substrattemperatur $T_{Sub,DIP} \approx 145$°C, Rate $R_{DIP} \approx 12$ Å/min):

1. $T_{Sub,Au} = -120$°C, $R_{Au} \approx 23$ Å/min
2. $T_{Sub,Au} = -120$°C, $R_{Au} \approx 0.35$ Å/min
3. $T_{Sub,Au} = +70$°C, $R_{Au} \approx 23$ Å/min
4. $T_{Sub,Au} = +70$°C, $R_{Au} \approx 0.35$ Å/min

Methoden

Die Proben wurden anschließend mit unterschiedlichen experimentellen Methoden untersucht:

- Zunächst wurde die Qualität der Grenzfläche 'as-grown' mit Querschnitts-Transmissions-Elektronenmikroskopie bestimmt.

- Die thermische Stabilität und der Desorptionsmechanismus der organischen Schicht in diesem Heterosystem wurde anschließend in Röntgenexperimenten am HASYLAB in Hamburg ermittelt. Dazu wurden die Proben in einer kleinen Vakuumkammer bei einer bestimmten Temperatur jeweils für eine Stunde getempert und in der Folge wurde die spekuläre Reflektivität und der erste spekuläre Bragg-Reflex der DIP-Schicht gemessen.

- Zusätzlich wurde die kristallographische Struktur und die Ordnung der Goldschicht nach jedem Temperschritt durch spekuläre Bragg-Streuung und durch Rockingscans untersucht.

- Mit hochauflösender Rutherford Rückstreuung (RBS) wurde schließlich der Frage nachgegangen, bis zu welcher Temperatur die Au/DIP-Grenzfläche gegenüber Interdiffusion von Gold in DIP stabil ist. Dazu wurde auf eine wohldefinierte DIP-Schicht ($D_{DIP} \approx 380$ Å, $T_{Sub,DIP} \approx 145$°C, $R_{DIP} \approx 12$ Å/min) *in situ* ein Goldfilm mit $D_{Au} \approx 70$ Å bei Raumtemperatur und einer Rate von $R_{Au} \approx 1$ Å/min präpariert. Anschließend wurde die Probe für jeweils eine Stunde bei schrittweise höheren Temperaturen getempert. Der RBS-Gold-Peak wurde 'as grown' und nach jedem Temperschritt gemessen, um aus seiner Form auf mögliche Diffusionsprozesse schließen zu können.

Ergebnisse

- Es konnte gezeigt werden, dass die Morphologie der Au/DIP-Grenzschicht entscheidend von den Wachstumsbedingungen der Goldschicht abhängt. Aufdampfen von Gold bei tiefen Substrattemperaturen (-120°C) führt dabei zu gut definierten Grenzschichten, die lediglich einen geringen Grad an Interdiffusion von Gold in die DIP-Schicht aufweisen. Die Wachstumsrate beeinflusste in dem hier untersuchten Bereich ($0.35\,\text{Å/min} \leq R \leq 23\,\text{Å/min}$) die Grenzflächenmorphologie nur, wenn gleichzeitig eine hohe Substrattemperatur (+70°C) angewendet wurde.

- Die thermische Stabilität der DIP-Schicht bleibt im Vergleich zu reinen DIP-Filmen nahezu unverändert bis $T \approx 155$°C gegeben. Allerdings verläuft der bei höheren Temperaturen einsetzende Desorptionsvorgang lateral inhomogen. Diese Beobachtung unterscheidet sich von der eines lateral homogenen Desorptionsprozesses bei reinen DIP-Filmen und könnte dem Goldfilm zugeschrieben werden.

- Die Goldschicht zeigt unmittelbar nach der Präparation eine hohe Mosaizität. Goldfilme, die bei niedriger Substrattemperatur hergestellt wurden (−120°C) zeigen bei ansteigenden Temperaturen (ab $T \gtrsim 120$°C) den Beginn eines Umordnungsprozesses. Dieser führt zu Gold-Körnern, die entlang der Oberflächennormalen überwiegend eine (111)-Orientierung aufweisen. Die Ursache für den Umordnungsprozess könnte in der für $T > 100$°C erleichterten Diffusion der Goldatome im DIP-Film gesehen werden. Goldfilme, die bei hohen Substrattemperaturen (+70°C) hergestellt wurden, weisen nur einen geringen Umordnungsprozess auf, der überdies erst für $T \geq 150$°C beobachtet wird.

- Weiterhin konnte in den RBS-Experimenten gezeigt werden, dass die

Grenzfläche bis zu einer Temperatur von etwa 100°C stabil gegen weitere Diffusionsvorgänge ist.

Chapter 2

Introduction

Due to their potential for use in electronic and optoelectronic applications, semiconducting organic materials are in the focus of a rapidly increasing research activity. Organic field effect transistors, organic light emitting diodes, or organic solar cells are only few examples of tailored organic device structures [14–17].

There is a large number of organic molecules that could potentially be used for the fabrication of organic electronic devices and for the study of fundamental questions concerning growth, structure, and physical properties. However, *planar molecules* (for example some phthalocyanines, pentacene-derivates, and perylene-derivates) are of particular interest for the investigation of these issues. Their comparatively low molecular weight in combination with their stability against polymerization and thermal decomposition up to several hundred degrees C permit the sublimation of the molecules under UHV-conditions. Thus, it is possible to fabricate thin (crystalline) films of these molecules with a maximum control of the deposition parameters by organic molecular beam epitaxy (OMBE).

DIP thin films

Recently, Münch investigated the charge-carrier mobility in thin films of a certain planar molecule, the perylene-derivate diindenoperylene (DIP), deposited on SiO_2 at $T \approx 140°C$. Employing laboratory x-ray sources to characterize the samples it turned out that the so prepared DIP thin films exhibit high structural order normal to the substrate surface with small rocking widths [1]. In spite of the ease of preparation and the interesting electrical properties and structural aspects in DIP thin films, to date only little is known about their physical and structural properties.

One aim of this thesis was to systematically investigate details of the growth and of the structure of DIP thin films employing *high-resolution* x-ray scattering at synchrotron sources. Due to the high quality of both structural order and x-ray data a quantitative analysis of the data provides insight into the underlying growth mechanism as well as into the out-of plane structure as a function of film-thickness.

The first part of this thesis is organized as follows. Chapter 3 briefly reviews the properties of the molecule DIP, the known data about its bulk and about its thin-film structure on various substrates. In Chapters 4-6 the experimental methods employed in this thesis are presented. The DIP thin film structure at room temperature and upon elevated temperatures are addressed in Chapter 7. First results on DIP thin films deposited on SiO_2 which were obtained by cross-sectional TEM, AFM, high-resolution x-ray scattering and spectroscopic ellipsometry measurements are shown in Sec. 7.1. Specular x-ray scattering was used to determine the electron density of DIP-films along the surface-normal, $\rho_{el}(z)$, with high precision. This is achieved by fitting the specular rod up to the 9th DIP-Bragg-reflection using a semi-kinematical formalism (Sec. 7.2). Furthermore, the thermal stability of DIP-films as well as the thermal expansion coefficient along the z-axis and the desorption mechanism is investigated (Sec. 7.3). At the end of Chapter

7.2, the in-plane structure of DIP-films deposited on thermally oxidized silicon and on A-plane sapphire is examined by means of grazing incidence x-ray diffraction (GIXD) experiments.

The formation of thin film structures as well as the topography of sample surfaces cannot be understood without knowledge of the underlying growth processes. Besides atomistic growth-models using Monte-Carlo simulations to understand the formation of thin-film morphologies, a theoretical framework has been established over the past two decades which relates the mechanism involved in the growth of a thin film to a set of scaling exponents (roughness exponent α, growth exponent β, and inverse dynamical exponent $1/z$) describing the dependence of the surface roughness on film thickness and lateral length scale [2, 3, 18, 19]. Despite their potential in technological applications and great efforts to characterize their crystalline structure, to date there are only very few studies concerning the scaling exponents of organic thin films and in particular of small molecules deposited under UHV-conditions [4–7].

Therefore, the growth-process described by scaling exponents will be addressed in this thesis in addition to the structural investigations of DIP thin films. For this purpose, DIP-films with a film thickness between ≈ 70 Å and ≈ 9000 Å were examined by non-contact AFM, by x-ray-reflectivity, and by x-ray-diffuse scattering. In Chapter 8 these experiments and the obtained scaling exponents α, β, and $1/z$ as well as a discussion of the associated growth process are presented.

The metal-organic heterosystem Au/DIP

Besides high charge-carrier mobilities inside the organic layer, the proper function of the contact between the metal and the organic layer is of great importance for device performance. Thus, knowledge of the associated morphology of the metal-organic interface as well as its thermal stability is essential. To date, only few studies have been published on metal-organic interfaces,

mainly on disordered polymers used as low dielectric constant material in conventional microelectronic fabrication processes [9–11]. Some studies have also been published on Langmuir Blodgett films [12] and on UHV-deposited organic thin films [13].

In this thesis, the interface between gold and DIP thin films as a model system for metal-contacts on organic electronic devices is investigated immediately after deposition and during annealing. DIP is particularly suitable for this study, since the surface of the DIP films is very well-defined and exhibits large terraces (up to several 100 nm) with monomolecular steps of 16.5 Å. Moreover, DIP exhibits excellent crystalline order (see, e.g., Chapter 3) associated with high charge carrier mobilities of up to $\mu = 0.1$ cm^2/Vs [1]. Gold is widely used for contacting organic electronic devices and is rather inert, hence specific chemical interactions are expected to play only a minor role. This facilitates the study of the role of substrate temperature and deposition rate on the morphology of the metal-organic interface. Annealing studies are particularly important to address the issue of thermal stability of devices operating at elevated temperatures.

At the beginning of Chapter 9, the preparation conditions which lead to a well-defined Au/DIP interface immediately after deposition are examined by cross-sectional TEM and x-ray-reflectivity measurements (Sec. 9.3). Following this step, the thermal stability of the DIP thin film in this heterosystem at elevated temperatures and its desorption mechanism are investigated by *in situ* x-ray-scattering (Sec. 9.4). To illuminate the structural changes in the 'contact' at these elevated temperatures, the gold film is also investigated by *in situ* x-ray scattering (Sec. 9.5). Finally, the thermal stability of the metal-organic interface is studied employing *in situ* high-resolution Rutherford backscattering spectrometry (RBS) as a function of temperature (Sec. 9.6).

Chapter 3

Diindenoperylene – DIP

3.1 The Molecule and its Properties

DIP (Fig. 3.1) is a planar perylene-derivate with two indeno-groups located at opposite sides of the perylene-core thus giving the chemical formula $C_{32}H_{16}$, with a molecular weigth of 400.48 g/mol and the specific name Diindeno-[1,2,3-cd:1',2',3'-Im]perylene (sometimes referred to as 'Periflanthene'). The extensions of the molecule, ≈ 18.4 Å $\times$ 7 Å, were calculated on the basis of the 'Cambridge Crystallographic Database' by a combination of the data of fluoranthen ($C_{16}H_{10}$) and perylene ($C_{20}H_{10}$); the H-atoms and their van-der-Waals radii were also taken into account [1]. DIP is thermally stable against polymerization and decomposition. It starts to sublime at $T > 330$°C.

DIP is only slightly soluble and separates as red, copper-like shimmering crystals from solution in trichlorobenzene. The synthesis was first described by von Braun in 1934 [20] and later on by Clar [21, 22].

As a polyaromatic-hydrocarbon (PAH), DIP has been found also as a pyrolisis-product [23] of polyaromatic hydrocarbons and even in interstellar space [24].

Studies on the carcinogeneity of PAH molecules suggest that DIP is not

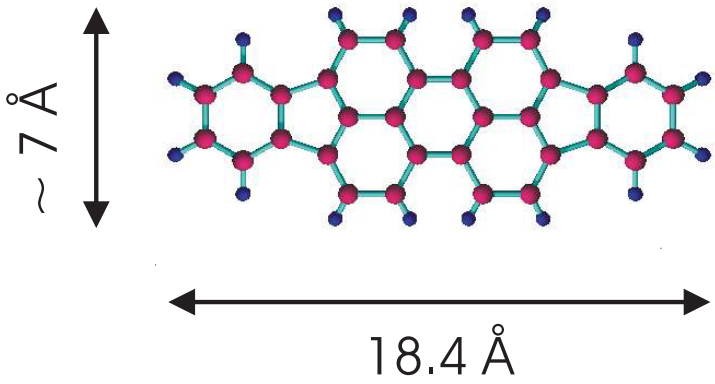

Figure 3.1: The structure of a DIP-molecule, $C_{32}H_{16}$: red circles denote carbon atoms, blue circles hydrogen atoms. The extensions were calculated by Münch [1].

a carcinogen [25–28]. Rather, it is thought to have the potential to be used as an anti-virus medicine [29].

The molecules used in our experiments were purchased from Aldrich and from the 'Institut für PAH-Forschung', Greifenberg, Germany. Before they were used for the preparation of thin-film samples they were purified by gradient-sublimation in the 'Kristallabor der Universität Stuttgart'.

3.2 Structure of DIP Single-Crystals

The structure of bulk-DIP was not known until recently. In the 1950s and 1960s Hofer published powder-diffraction data on the structure of DIP [30–32]. However, only the most prominent lines were reported. In 2001 Frey and Karl [33] determined the structure of DIP in single crystals. They obtained a triclinic structure with

- space-group $P\overline{1}$; $Z = 4$;

- $a = 1.15941(14)$ nm; $b = 1.2968(2)$ nm; $c = 1.4879(2)$ nm;
- $\alpha = 98.108(9)^\circ$, $\beta = 98.101(10)^\circ$; $\gamma = 114.527(9)^\circ$;
- $V = 1.9649(4)$ nm^3; $\rho = 1.354$ g/cm^3.

3.3 Thin Films of DIP

Until now, there have been only few studies completed on the structure of DIP thin-films. Strohmaier *et al.* investigated (sub)monolayers of DIP on graphite [34] by scanning tunneling microscopy (STM). In this study the DIP-moelcules were lying flat on the substrate surface.

Hoshino *et al.* studied the crystallography of DIP thin films on perylene and NaCl-substrates, respectively [35] by TEM. It was found in this study that the molecules exhibit a herringbone structure and the following lattice parameters were revealed

- DIP/NaCl: $a = 8.67$ Å, $b = 6.96$ Å,$c = 18.55$ Å, and $\beta = 93.5^\circ$. $c' = 18.52$ Å
- DIP(150 Å)/perylene: $a = 11.0$ Å, $b = 10.6$ Å, $c = 17.5$ Å, and $\beta = 106.0^\circ$. $c' = 16.82$ Å

in which the lattice spacing along the z-axis, c', is given by the relation $c' = c \cdot \sin\beta$.

Recently, Münch investigated the charge carrier mobility in DIP-films (D_{DIP} in the order of 500 Å) deposited on thermally oxidized silicon-wafers [1]. In this study it was found that DIP films deposited onto silicon-dioxide show a high degree of crystalline order and that the charge carrier mobility (up to 0.1 Vs/cm^2) (anti)correlates with the mosaicity of the out-of-plane DIP-lattice planes.

The presence of high structural order in thin films of the organic semiconductor DIP on SiO_2 was the motivation for a systematic study of the growth behavior and of the structural aspects of DIP thin films of various thickness employing in particular *high-resolution* (synchrotron) x-ray measurements and subsequently analyze the data *quantitatively*.

Chapter 4

X-ray Scattering From Thin Films

The scattering of x-rays was used in this thesis to investigate structural aspects of organic thin films and of metal-organic heterostructures. In this chapter, the theory of x-ray scattering in various experimental geometries is described. For details of the derivations see Refs. [36–38].

4.1 Optical Effects in X-Ray Scattering: Refraction and Absorption

Scattering of electromagnetic waves can be described by introducing an index of refraction, n, and solving Maxwell's equations. In the following sections, plane waves of x-rays are considered with the electric field vector denoted as

$$E(\mathbf{r}) = A_0 e^{i\mathbf{k_i}\cdot\mathbf{r}} \quad . \tag{4.1}$$

4.1.1 The index of refraction, n, and Snell's law of refraction

The complex index of refraction, n, is used in x-ray as well as in light scattering to describe the effects of reflection and of refraction. For homogeneous media it reads

$$n = 1 - \delta + i\beta, \tag{4.2}$$

with δ and β being the dispersion and absorption, respectively. For x-ray energies far from absorption edges, they are written as

$$\delta = \frac{\lambda^2}{2\pi} r_e \rho_{el} \tag{4.3}$$

and

$$\beta(r) = \frac{\lambda}{4\pi}\mu \quad . \tag{4.4}$$

In the above, λ is the wavelength of the impinging x-ray wave, $r_e = 2.8 \cdot 10^{-15}$ m is the classical electron radius, ρ_{el} is the electron density of the medium, and μ is the linear absorption coefficient of the medium. For x-rays, δ is always positive, i.e., $n < 1$ inside the medium (neglecting[1] β).

For a single vacuum / medium interface, Snell's law of refraction relates the incident angle α_i of the impinging wave to the angle of the transmitted wave in the medium, α_t (see also Fig. 4.1), via

$$n = \frac{\cos\alpha_i}{\cos\alpha_t} \quad . \tag{4.5}$$

Because $n < 1$, there will be an incident angle at which α_t becomes 0. This angle is designated the *critical angle* of total external reflection, α_c, and can be written as (Taylor expansion of $\cos\alpha_i$):

[1]For $\beta \neq 0$ the index of refraction, n, becomes a complex number and '$n < 1$' only applies for the real part of n.

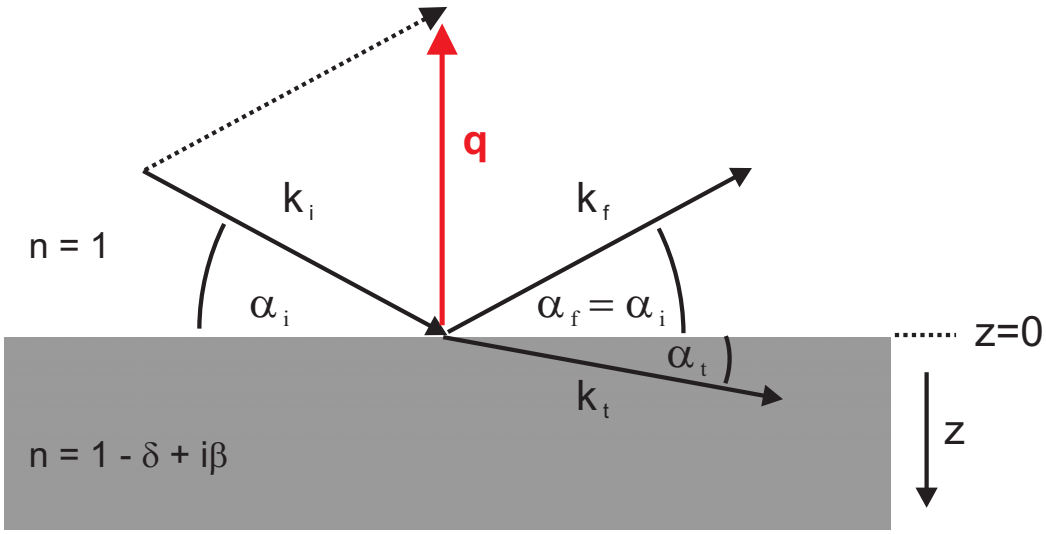

Figure 4.1: Schematic for reflection and refraction at an interface. $\mathbf{k_i}$, $\mathbf{k_f}$, and $\mathbf{k_t}$ are the wavevectors of the incident, reflected and transmitted wave, respectively. For $\alpha_i = \alpha_f$ the momentum transfer $\mathbf{q} = \mathbf{k_i} - \mathbf{k_f}$ reads $\mathbf{q} = (0, 0, q_z)$.

$$\alpha_c \approx \sqrt{2\delta} = \lambda\sqrt{r_e \rho_{el}/\pi} \tag{4.6}$$

Typical values of δ for x-ray energies $\approx$ 10 keV are in the order of $10^{-6} \ldots 10^{-5}$. This implies critical angles in the range of $\alpha_c = 0.2° \ldots 0.5°$. The absorption coefficient β is usually a factor of $10 \ldots 100$ smaller than δ. For low-Z materials like organics, β is in the order of 5×10^{-9}. Thus, for the derivation of the intensity of specularly reflected x-rays β will be neglected.

4.1.2 The Fresnel coefficients

Calculating the transmitted and the reflected field-amplitudes for a plane wave impinging on the surface, the well-known Fresnel coefficients R_F and T_F (Eq. 4.9 and 4.10) are obtained for the reflected and transmitted waves, respectively [39]. To calculate the transmitted and reflected field amplitudes, the continuity of the tangential components of the electric and of the magnetic field at the interface ($z = 0$) is used. The $z-$components of the incoming ($k_{i,z}$) and the transmitted ($k_{t,z}$) wave read

$$k_{i,z} = k \sin \alpha_i \tag{4.7}$$

and

$$k_{t,z} = k\sqrt{n^2 - \cos^2 \alpha_i} \approx k\sqrt{\alpha_i^2 - \alpha_c^2} \tag{4.8}$$

(using Snell's law, Eq. 4.5). For x-rays with the refractive index n being almost unity, the distinction between $s-$ and $p-$ polarization of the impinging wave can be omitted[2]. Then, R_F and T_F are calculated as:

$$R_F = \frac{k_{i,z} - k_{t,z}}{k_{i,z} + k_{t,z}} \overset{\alpha_i \ll 1}{=} \frac{\alpha_i - \alpha_i'}{\alpha_i + \alpha_i'} \tag{4.9}$$

$$T_F = \frac{2k_{i,z}}{k_{i,z} + k_{t,z}} \overset{\alpha_i \ll 1}{=} \frac{2\alpha_i}{\alpha_i + \alpha_i'} \tag{4.10}$$

with the refracted beam angle α_i' as

$$\alpha_i' = \sqrt{\alpha_i^2 - \alpha_c^2} = \alpha_i\sqrt{1 - \alpha_c^2/\alpha_i^2} \tag{4.11}$$

[2]Moreover, for the experiments presented in this thesis, synchrotron light was employed with the scattering plane perpendicular to the plane of the storage ring. This implies that only s-polarized waves were used.

For $\alpha_i \gg \alpha_c$ it is possible to approximate α_i' by the first term of a Taylor expansion: $\alpha_i' \approx \alpha_i(1+(\alpha_c/2\alpha_i)^2)$. Employing a second approximation, $4\alpha_i^2 + \alpha_c^2 \approx 4\alpha_i$, Eq. 4.9 reduces to

$$R_F \simeq \left(\frac{\alpha_c}{2\alpha_i}\right)^4 \quad . \tag{4.12}$$

The deviation of this approximation from the 'true' R_F is smaller than 3% for $\alpha_i \gtrsim 3\alpha_c$.

Eq. 4.12 describes the characteristic steep decay of the intensity with increasing incident angle α_i close to the critical angle α_c in x-ray reflectivity measurements.

The case $\alpha_i < \alpha_c$

If the incident angle is smaller than the critical angle, $\alpha_i < \alpha_c$, then $k_{t,z}$ in Eq. 4.8 becomes imaginary and reads $k_{t,z} = ik\sqrt{\alpha_i^2 - \alpha_c^2}$. Inserting $k_{t,z}$ into the expression for the electrical field in the medium, E reads:

$$E \sim e^{ik_{t,z}z} \sim e^{-zk\sqrt{\alpha_i^2-\alpha_c^2}} = e^{-z/\Lambda} \tag{4.13}$$

This implies a wave traveling parallel to the surface. The amplitude which penetrates the sample perpendicularly decreases exponentially with increasing depth (*evanescent wave*). The depth at which the *amplitude of the wave* has decreased to $1/e$ is designated as the penetration depth Λ. To calculate Λ, we consider β, as otherwise $\Lambda \to \infty$ for $\alpha_i = \alpha_c$. Then, Λ reads

$$\begin{aligned} \Lambda^{-1} &= \frac{k}{\sqrt{2}}\left(\sqrt{(\alpha_i^2 - \alpha_c^2)^2 + 4\beta^2} + \alpha_c^2 - \alpha_i^2\right)^{1/2} \\ &\overset{\beta\to 0}{=} k\sqrt{\alpha_c^2 - \alpha_i^2} \end{aligned} \tag{4.14}$$

using only the (negative) solution $(\alpha_c^2 - \alpha_i^2)$ of the expression $\sqrt{(\alpha_i^2 - \alpha_c^2)^2}$ in the last step.

For $\alpha_i \to 0$, the penetration depth becomes independent of the wavelength and is only dependent on the electron density of the medium: $\Lambda = \lambda/(2\pi\alpha_c) = 1/\sqrt{4\pi r_e \rho_{el}}$.

The effect of evanescent waves is used in particular for the determination of lateral structures in thin films by grazing incidence diffraction (GID). This method is addressed in more detail in Sec. 4.4.

4.2 Reflectivity - Specular and Diffuse Scattering

4.2.1 Multiple interfaces - Parratt-formalism

The condition for specular x-ray reflectivity is $q_x = q_y = 0$, implying $\alpha_i = \alpha_f$. Since the momentum transfer $\mathbf{q}$ has only a component along the z-direction the laterally averaged electron-density profile along the z-axis, $\rho_{el}(z)$, is measured.

Parratt-formalism for sharp interfaces

With the Parratt-formalism [38, 40], the specular x-ray reflectivity intensity from a sample consisting of N layers on top of a substrate, i.e., $N+1$ interfaces, is calculated by a recursive algorithm. The sample is represented by a 'box-model' where each box j corresponds to layer j with constant thickness, D_j, and refraction index n_j, i.e., electron density $\rho_{el,j}$ (see Fig. 4.2). In this model, layer 1 is the medium above the sample (usually vacuum) and the substrate is layer $N+1$.

The ratio between reflected and transmitted wave-amplitudes in the j-th layer, X_j, is then calculated as:

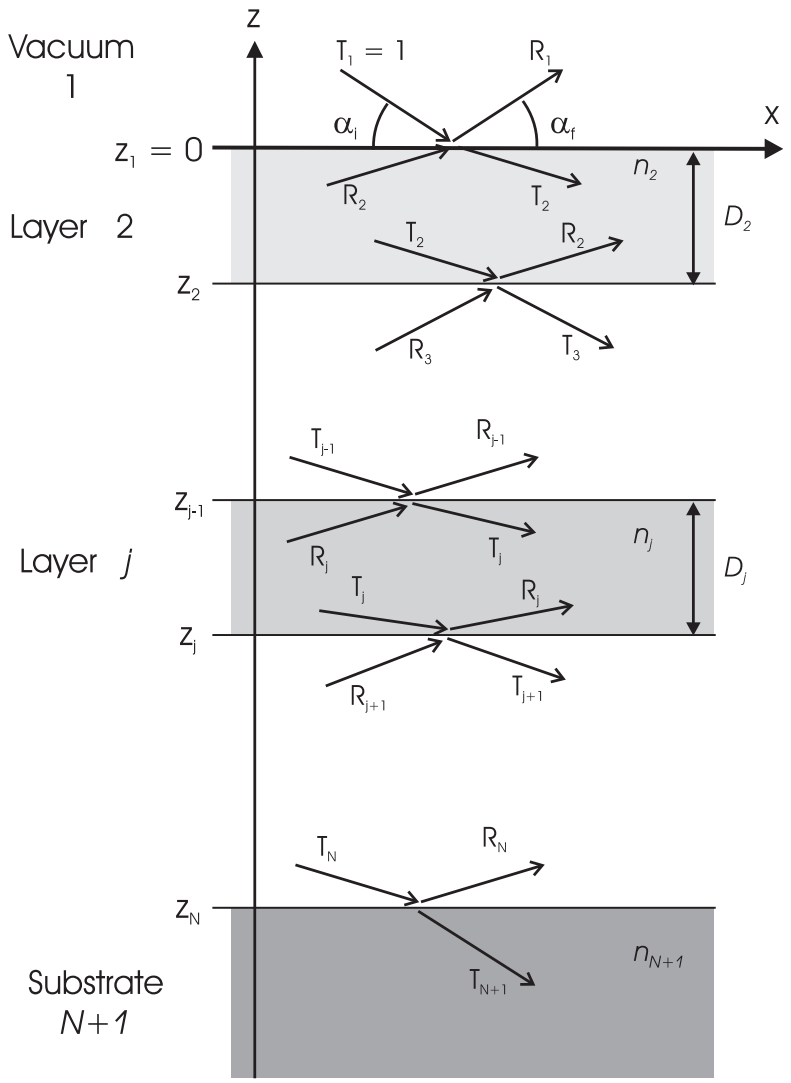

Figure 4.2: Schematic for the parameterization of a sample in the Parratt-formalism

$$X_j = \frac{R_j}{T_j} = e^{-2i\,k_{z,j}z_j}\frac{R_{j,j+1} + X_{j+1}e^{2ik_{z,j+1}z_j}}{1 + R_{j,j+1}X_{j+1}e^{2ik_{z,j+1}z_j}} \tag{4.15}$$

with

$$R_{j,j+1} = \frac{k_{z,j} - k_{z,j+1}}{k_{z,j} + k_{z,j+1}} \tag{4.16}$$

as the Fresnel coefficient of interface j and where $k_{z,j} = k\sqrt{n_j^2 - \cos^2 \alpha_i}$ denotes the z component of the wavevector in layer j (see also Eq. 4.8). The measured intensity is given after N iterations as

$$R = |X_1|^2 = |R_1|^2 \tag{4.17}$$

using the transmission-coefficient in layer 1 ($\equiv$ vacuum) $T_1 = 1$. To solve the recursive algorithm, it is assumed that there is no reflection from the substrate, i.e., $R_{N+1} = X_{N+1} = 0$.

The most prominent features of x-ray reflectivity measurements are the rapidly decaying intensity for incident angles α_i larger than the critical angle α_c ($I \propto \alpha_i^{-4}$, Eq. 4.12) and the so-called Kiessig fringes that are superimposed on the Fresnel-reflectivity. These oscillations are due to the interference between the wave amplitudes reflected from the individual layers. Each periodicity in the oscillations $\Delta q_{z,j}$ is related to the thickness of one layer by the relation $D_j = 2\pi/\Delta q_{z,j}$.

Interfacial roughness

Real samples do not exhibit sharp interfaces, but show some interfacial roughness. Let $h_j(x, y)$ be the height function that relates each point (x, y) of interface j to a specific height, then σ_j, which is defined as the square root of the mean squared height fluctuations, reads

$$\sigma_j = < (\tilde{z}_j(x, y))^2 >^{1/2}, \tag{4.18}$$

where the height fluctuation $\tilde{z}_j(x, y)$ at point (x, y) around the mean height of the interface, $h_{j,0} = < h_j(x, y) >$ is given by

$$\tilde{z}_j(x,y) = h_j(x,y) - h_{j,0}. \tag{4.19}$$

Assume that the fluctuations around $h_{j,0}$ could be described by a Gaussian probability distribution with 95% of all fluctuations lying in the interval $h_{j,0} \pm \sigma_j$ (which is often the case in real samples). Then the index of refraction, $n(z)$, between layer j and $j+1$ follows a continuous, error-function-like transition from n_j to n_{j+1}. In this case, interfacial roughness can be implemented in the Parratt-formalism by simply multiplying $R_{j,j+1}$ (Eq. 4.16) by an exponential damping factor $\exp(-2\mathrm{k_{z,j}k_{z,j+1}}\sigma_\mathrm{j}^2)$ (referred to as 'Névot & Croche' factor [41] in the literature). The modified Fresnel coefficient for the reflection from the interface between layer j and $j+1$ then reads:

$$\tilde{R}_{j,j+1} = \frac{k_{z,j} - k_{z,j+1}}{k_{z,j} + k_{z,j+1}} \, e^{-2k_{z,j}k_{z,j+1}\sigma_j^2} \tag{4.20}$$

Note, however, that this holds true only if σ_j is much smaller than the thickness of layer j and $j+1$, $\sigma_j \ll D_j$ and $\sigma_j \ll D_{j+1}$.

Roughness results in damping of the specularly reflected intensity and gives rise to diffuse scattering in non-specular directions ($q_{x,y} \neq 0$), which therefore contains information about the in-plane structure of the sample. The analysis of the diffuse intensity will be discussed in Sec. 4.2.3.

4.2.2 Kinematic scattering theory - Master formula

In the preceding sections, the Fresnel reflectivity for single interfaces and the recursive Parratt-formalism were considered to describe the specularly scattered x-ray intensity of layered systems. This description has the advantage that it takes into account all scattering contributions and is therefore correct even for incident angles α_i close to the critical angle.

However, the box-model, which is used to parameterize the sample can become a drawback for certain practical applications. In particular, the attempt

to fit the complete specular rod is critical, if the sample either exhibits a periodic structure that gives rise to distinct Bragg-reflections (see section 4.3), or if an (organic) thin-film system shows pronounced intralayer electron-density oscillations. Here, a fit assuming a simple electron density profile consisting of only a single box with a constant electron density ρ_{film} and thickness D_{film} will fail already at small angles. On the other hand, the endeavor to model the smooth and oscillatory 'real' electron density $\rho_{el}(z)$ profile by slicing the film into a large number of boxes results in large computing times for the recursive algorithm. In addition, a huge number of free fitting parameters are needed, which makes the resulting electron density profile fairly ambiguous.

Besides the (exact) Parratt-formalism, there are other approaches to calculate the specular scattering intensity based on semi-kinematic theory (i.e., only single scattering events are considered). One of the most prominent and simplest expressions in this framework is the so-called 'Master formula' (Eq. 4.21). It is well suited to describe the specular rod intensity for layered samples where the absorption of x-rays in the layers above the substrate plays only a minor role. This condition is fulfilled for x-ray scattering on organic thin films with x-ray energies of $\approx$ 10 keV that were used in our experiments. The advantage of semi-kinematic theory is the opportunity to tailor the required (smooth and oscillatory) electron-density by (only few) analytical functions. This tremendously reduces the number of free fitting parameters.

The Master formula

The Master formula is given by the following expression:

$$R(q_z) = I_0 G(q_z) R_F(q_z) \left| \frac{1}{\rho_{el,\infty}} \int \frac{d\rho_{el}(z)}{dz} \, e^{iq_z z} dz \right|^2 = I_0 G(q_z) R_F(q_z) \left| F(q_z) \right|^2 \tag{4.21}$$

where I_0 is a constant factor accounting for the scattering geometry and the flux of photons, $\rho_{el,\infty}$ is the electron density of the substrate, and $G(q_z)$ is a factor that takes into account illumination corrections for small incident angles[3] α_i.

For a semi-kinematic treatment of the scattering, it is possible to take into account refraction corrections at incident angles close to α_c. For this correction, q_z in the structure factor $F(q_z)$ of Eq. 4.21 is replaced by

$$q_z' = 2k \ \sin\left(\sqrt{\alpha_i^2 - \alpha_c^2}\right) = 2k \ \sin(\alpha_i') \tag{4.22}$$

The validity of the (semi-)kinematic approach was extensively investigated by Hamley and Pederson [42,43]. It turned out that the Master-formula intensity, $I_{MF}(q_z)$, does not significantly deviate from that calculated by the Parratt-algorithm, $I_{Parratt}(q_z)$, for roughly $\alpha_i \gtrsim 3\alpha_c$ (with some dependence on the sample parameters). For smaller α_i, dynamical scattering effects have a significant influence on the scattered intensity. Here, only the envelope of $I_{MF}(q_z)$ matches $I_{Parratt}(q_z)$, see also Fig. 4.3.

Measuring and analyzing specular x-ray reflectivity

In an experiment the measured specular intensity I_{tot} is a superposition of the true specular intensity, I_S, and the diffusely scattered intensity, I_D (see also Sec. 4.2.3): $I_{tot} = I_S + I_D$. Thus, I_S has to be extracted by carefully subtracting the diffusely scattered intensity from the measured intensity before analyzing the data. To subtract I_D, usually an 'offset-scan' is carried out where $\alpha_i = 2\Theta/2 \pm \alpha_{off}$. α_{off} is chosen such that the data are recorded

[3]This illumination correction applies for $\alpha_i < \arcsin(b/L)$, where b is the width of the beam, and L is the length of the sample parallel to the beam-direction. For $\alpha_i < \arcsin(b/L)$, the illuminated area at the sample position ('footprint') is larger than the sample and therefore the scattered intensity is reduced by the ratio between the totally illuminated area and the illuminated area of the sample.

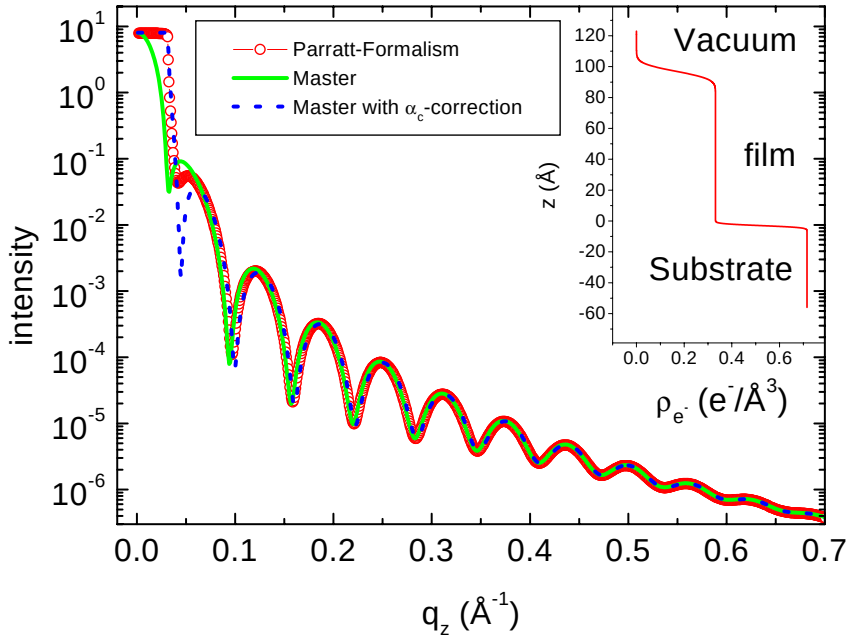

Figure 4.3: Comparison of Master formula and Parratt-formalism. The calculated intensities for an organic film with $D = 100$ Å on a silicon substrate at a wavelength of $\lambda = 1.54$ Å are shown. The inset displays the electron density profile $\rho_{el}(z)$ that was used to calculate both spectra.

slightly beside the specular rod, where only diffusely scattered intensity is expected. The data of the offset-scan are subtracted from I_{tot} before fitting I_S by either the Parratt-algorithm or by the Master formula.

4.2.3 Diffuse scattering

Interfacial roughness, σ, gives rise to scattering in non-specular directions ($q_{\|} \neq 0$), i.e., *diffuse scattering* [8, 44–47]. Therefore, it contains information about lateral correlations of the sample due to the non-zero momentum

transfer parallel to the surface.

To analyze the diffusely scattered intensity of rough surfaces, it is useful to describe the surface by a statistical approach. The height fluctuation, $\tilde{z}(x,y)$ (Eq. 4.19), of point (x,y) around the mean height of an interface, $h_{j,0}$, is used in the definition of the height-difference correlation function[4] (HDCF)

$$g(R) =< [\tilde{z}(x,y) - \tilde{z}(x',y')]^2 >, \tag{4.23}$$

where

$$R = [(x-x')^2 + (y-y')^2]^{1/2}, \tag{4.24}$$

and the average is taken over all pairs of points on the surface, which are separated horizontally by the length R. The function $g(R)$ is related to the height-height correlation function $C(R) =< \tilde{z}(R)\tilde{z}(0) >$ by

$$\begin{aligned} g(R) &= 2 < (\tilde{z}(x,y))^2 > \; - 2 < \tilde{z}(x,y)\tilde{z}(x',y') > \\ &= 2\sigma^2 \; - \; 2 < \tilde{z}(R)\tilde{z}(0) > \\ &= 2\sigma^2 \; - \; 2\,C(R) \end{aligned} \tag{4.25}$$

For the second step the definition of roughness, Eq. 4.18, is used.

The diffusely scattered intensity can be calculated according to Sinha *et al.* [8]. They derived the cross-section for the diffuse scattering using perturbation theory (DWBA). Under such theory, the deviations from a smooth surface located at the spatial height average h_0 are considered as small perturbations. The scattering matrix is then solved using the eigenstates of the smooth surface. Their expression for the diffuse scattering, integrated with respect to one direction perpendicular to the scattering plane is given as

[4]For the height-difference correlation function of the sample surface, $g(R)$ reduces to $g(R) =< [h(x,y) - h(x',y')]^2 >$

$$I(q_\parallel, q_z) = I_0 \frac{\Delta\Omega}{A}(L_x L_y)\frac{|k_0^2(1-n^2)|^2}{16\pi^2} \times |T(\mathbf{k_i})|^2 |T(\mathbf{k_f})|^2 S(q_\parallel) \quad (4.26)$$

with

$$S(q_\parallel, q_z) = \frac{\exp(-[(q_{t,z})^2 + (q_{t,z}^*)^2]\sigma^2/2)}{|q_{t,z}|^2} \times \int_0^\infty (e^{|q_{t,z}|^2 C(R)} - 1) e^{(iq_\parallel R)} dR. \quad (4.27)$$

The x-ray data are assumed to be recorded with relaxed slit settings in the direction perpendicular to the scattering plane.

Here, k_0 is the wavevector magnitude, $L_x L_y$ denotes the area illuminated by the beam, and $\Delta\Omega$ is the solid angle seen by the detector at the sample.

In general, the integral of Eq. 4.27 is difficult to calculate. However, for $q_{t,z}^2 C(R) \ll 1$ the exponential of the integrand can be expanded. Then, the scattering function for the diffuse intensity, $S(q_\parallel, q_z)$, is simply the Fourier transformation of the height-height correlation function $C(R)$.

4.3 Bragg Scattering - Kinematic Theory

To derive the expressions for Bragg scattering, a monochromatic, plane x-ray wave is considered, as given by Eq. 4.1 and at this point, polarization is disregarded. The notations follow the notation of standard x-ray diffraction textbooks (e.g., Ref. [36]).

If the plane wave impinges on the sample, it interacts with the electrons of the atoms. To derive an expression for the scattered intensity, the scattering contributions of all electrons of the illuminated sample have to be added.

4.3.1 Lattice sum and scattering intensity of a small 3D crystal

Scattering from one atom

Scattering from the electrons of one atom is given by the (complex) atomic scattering factor $f(\mathbf{q})$, which is the Fourier transform of the electron density, $f_0(\mathbf{q})$, and by energy dependent terms that account for resonance effects close to absorption edges, $f'(\mathbf{q}, E)$ and $f''(\mathbf{q}, E)$:

$$f(\mathbf{q}) = f_0(\mathbf{q}) + f'(\mathbf{q}, E) + if''(\mathbf{q}, E) \tag{4.28}$$

with E as the energy of the incident x-ray wave. The terms $f_0(\mathbf{q})$, f' and f'' are listed in Refs. [48–50] for the individual elements.

Scattering amplitude from a crystalline lattice

Next, consider a three-dimensional crystal with the lattice vectors $\mathbf{a_x}, \mathbf{a_y}, \mathbf{a_z}$ being parallel to the $x-$, $y-$, and $z-$axis, respectively. The position of each atom then reads

$$\mathbf{R}_{n,n_1,n_2,n_3} = n_1\mathbf{a_x} + n_2\mathbf{a_y} + n_3\mathbf{a_z} + \mathbf{r_n} \quad . \tag{4.29}$$

Here, $\mathbf{r_n}$ describes the atomic arrangement within the unit cell. For a crystal lattice with an extension of N_1, N_2, and N_3 unit cells in the directions $\mathbf{a_x}, \mathbf{a_y}, \mathbf{a_z}$, the scattering amplitude is given by

$$A(\mathbf{q}) = \frac{r_e}{R_0} \cdot A_0 \cdot F(\mathbf{q}) \cdot \sum_{n_1=0}^{N_1-1} \cdot \sum_{n_2=0}^{N_2-1} \cdot \sum_{n_3=0}^{N_3-1} e^{i\cdot(q_x n_1 a_x + q_y n_2 a_y + q_z n_3 a_z)} \quad , \tag{4.30}$$

where R_0 is the distance between scattering center and detector and $F(\mathbf{q})$ is the structure factor:

$$F(\mathbf{q}) = \sum_{\text{unit cell}} f_n(q) e^{i\mathbf{q}\cdot\mathbf{r_n}} \quad . \tag{4.31}$$

The scattered intensity

Analyzing Eq. 4.30 in terms of a geometrical series and subsequent squaring gives the intensity

$$\begin{aligned} I(\mathbf{q}) &= \left(\frac{r_e}{R_0} \cdot A_0 \cdot F(\mathbf{q})\right)^2 \times \\ &\quad \frac{\sin^2(\frac{1}{2}\, N_1\, q_x a_x)}{\sin^2(\frac{1}{2}\, q_x a_x)} \cdot \frac{\sin^2(\frac{1}{2}\, N_2\, q_y a_y)}{\sin^2(\frac{1}{2}\, q_y a_y)} \cdot \frac{\sin^2(\frac{1}{2}\, N_3\, q_z a_z)}{\sin^2(\frac{1}{2}\, q_z a_z)}. \end{aligned} \tag{4.32}$$

If the so-called Laue-conditions

$$q_x \cdot a_x = h \cdot 2\pi, \;\; q_y \cdot a_y = k \cdot 2\pi, \;\; q_z \cdot a_z = l \cdot 2\pi \tag{4.33}$$

are all fulfilled ($h, k, l \in \mathbb{Z}$), and $F(\mathbf{q}) \neq 0$, then $I(\mathbf{q})$ exhibits a maximum with

$$I_{max}(\mathbf{q}) \propto N_1^2 N_2^2 N_3^2 \quad . \tag{4.34}$$

4.3.2 Amplitude for specular Bragg scattering in a free-standing thin film

Specular scattering is characterized by the condition $\alpha_i = \alpha_f$ and $q_x = q_y = 0$. Thus, Eq. 4.30 reduces to

$$\begin{aligned} A_{film}(q_z) &= \frac{A_0 r_e}{R_0} \cdot N_1 N_2 \cdot F(q_z) \cdot \sum_{n_3=0}^{N_3-1} e^{iq_z n_3 a_z} \\ &= \frac{A_0 r_e}{R_0} \cdot N_1 N_2 \cdot F(q_z) \cdot \frac{1 - e^{iq_z N_3 a_z}}{1 - e^{iq_z a_z}} \quad . \end{aligned} \tag{4.35}$$

where the factor $(N_1 N_2)$ represents the typical size of a single crystalline domain parallel to the surface.

Eq. 4.35 equals the expression for the scattering of light at an $N-$slit grid. For a free standing film of uniform thickness, the measured intensity is given by Eq. 4.32 (see also Fig. 4.4). The maxima are located at the positions $q_z = 2\pi l/a_z$ with $I_{max} \propto N_3^2$.

From the position of the principal maxima, the lattice spacing a_z perpendicular to the surface can be determined.

Aside the maxima side-peaks are visible. From the distance of the minima, Δq_z, of these so-called Laue-oscillations the number of ordered, i.e., coherently scattering, lattice planes, N_3, and the coherent thickness of the film, D_{coh}, can be calculated using the relation

$$D_{coh} = N_3 \cdot a_z = 2\pi/\Delta q_z \quad . \tag{4.36}$$

The intensity of a film which exhibits domains with different numbers of lattice planes is the incoherent superposition of the intensities of the individual domains. This superposition results in a damping or even extinction of the Laue-oscillations.

Intensity for thin films on top of a substrate

In experiments, the intensity of the *entire sample* is recorded, i.e., of a thin film on top of a substrate. To calculate the scattered intensity, first the *scattering amplitudes* of the film and of the substrate have to be summed up. The square of this sum then yields the intensity

$$\begin{aligned} I(q_z) &= |A_{film} + A_{Substrate}|^2 \\ &= |A_{film}|^2 + |A_{Substrate}|^2 + 2\,\mathrm{Re}(A^*_{film} A_{Substrate}) \quad . \end{aligned} \tag{4.37}$$

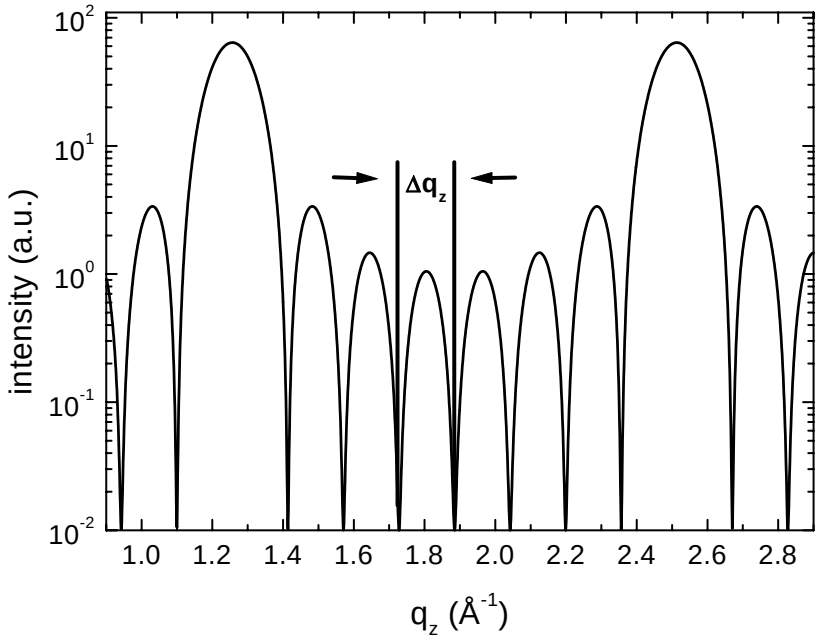

Figure 4.4: Calculation of the square of Eq. 4.35 simulating the intensity of a free standing film with 8 monolayers ($N_3 = 8$) and $a_3 = 5\,\text{Å}$. All other factors were set to 1. Note the logarithmic scale for the intensity.

The coherent superposition of the scattering amplitudes may cause significant asymmetries in the Laue-oscillations aside the Bragg-reflections of the thin film. This phenomenon could be observed particularly in the vicinity of the substrate Bragg-reflections where $A_{Substrate}$ is quite high and the interference term $2\,\mathrm{Re}(A^*_{film}A_{Substrate})$ becomes significant. The interference of the substrate- and film-amplitudes allows in principle for the determination of the relative scattering phase, e.g., Refs. [51, 52].

4.4 Grazing Incidence Diffraction (GID) from thin films

In the previous section it has been shown how structural information about a_z can be obtained by analyzing specular Bragg-reflections. However, to gain a comprehensive understanding about a thin film structure, lateral structure information is as well needed in form of Bragg-reflections. This information can be revealed by 'Grazing Incidence Diffraction', see Fig. 4.5.

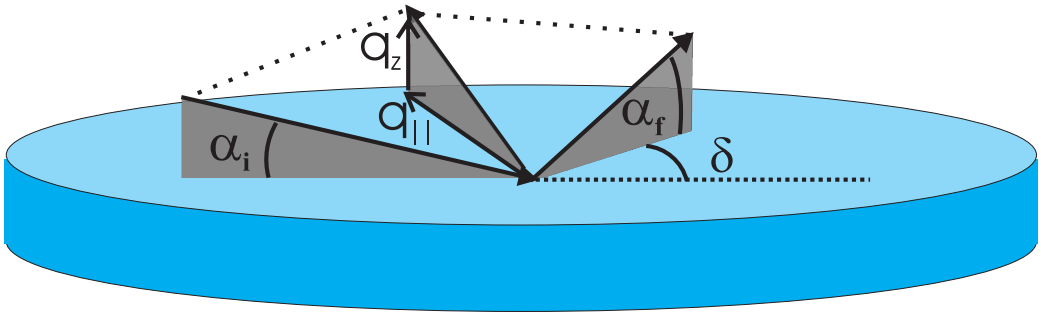

Figure 4.5: Schematic of an GID setup. The small incident and exit angles, α_i and α_f, respectively, (primarily) determine the momentum transfer q_z. The in-plane angle δ determines the momentum transfer $q_{\|}$.

In GID-experiments, small incident and exit angles, $\alpha_{i,f}$, close to the critical angle, α_c, are employed. This results in

1. a momentum transfer inside the sample, $\mathbf{q}'$, which has (almost) no specular component, i.e., $q'_z \simeq 0$ ($q'_z = 0$ holds only for $\alpha_{i,f} \leq \alpha_c$). Then, the Bragg-reflections are related to an in-plane lattice parameter, $\mathbf{a_x}$, $\mathbf{a_y}$ or a linear combination of $\mathbf{a_x}$ and $\mathbf{a_y}$. At least two independent Bragg-reflections in the plane in addition to the specular Bragg-reflections are needed to derive a 3D description of the structure inside the thin-film

which may significantly differ from that of the bulk phase of the film material.

2. x-ray waves, exponentially damped inside the sample for angles $\alpha_{i,f} \leq \alpha_c$ (see also Eq. 4.13) with a penetration depth of $\Lambda(\alpha_{i,f})$ (Eq. 4.14). This allows for a very precise control of the depth from which the structural information is obtained, and therefore permits a depth resolved structural analysis.

Detailed information about this technique and its applications are given, e.g., in Refs. [37, 53, 54].

Chapter 5

Rutherford Backscattering Spectrometry - RBS

Scattering of low-Z ions with an energy in the MeV range by atoms inside the sample is employed in Rutherford backscattering spectrometry (RBS). This allows for the determination of concentration profiles in thin film samples. Recording an RBS-spectrum is done by detecting the number of (back)scattered ions (under an angle θ, see Fig. 5.1) as a function of energy. This usually requires an energy dispersive detector and a multi-channel analyzer which distributes each recorded ion to the channel that covers the appropriate energy interval.

To describe the main characteristics of RBS measurements, three basic physical processes have to be considered. In the following three sections, these processes will be described briefly to give a comprehensive overview about this technique. For details the reader is referred to the books by Chu, Mayer, and Nicolet [55], Feldman and Mayer [56] and Tesmer [57].

5.1 The Kinematic Factor K

If a projectile with mass M_P and kinetic energy E_0 hits a target-atom with mass M_T, there will be an energy transfer from the projectile to the target-atom (see Fig. 5.1).

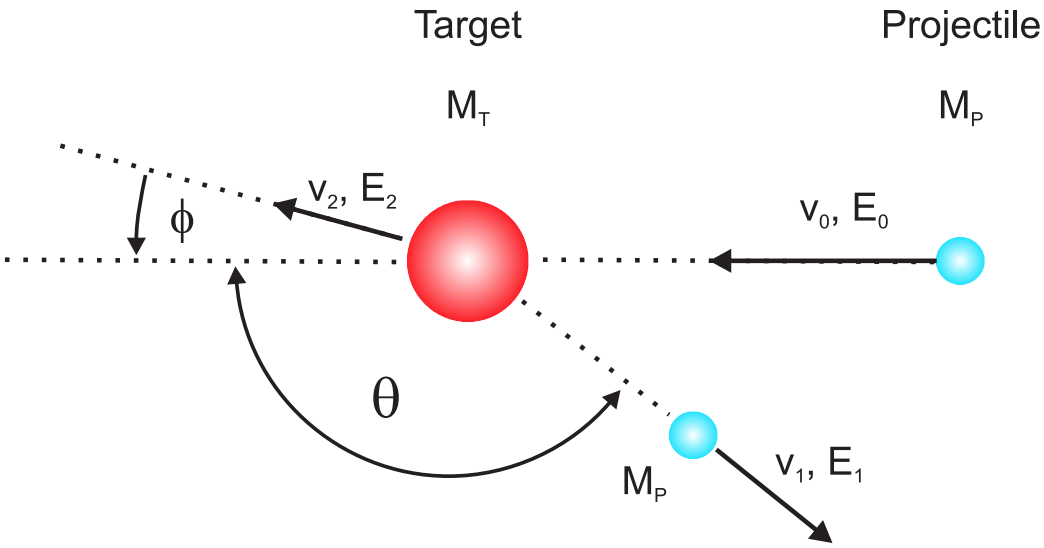

Figure 5.1: Schematic of the scattering between a projectile-atom with velocity $\mathbf{v_0}$, energy E_0, and mass M_P and a target-atom with mass M_T. After the collision, the projectile, scattered under the angle θ, has the velocity $\mathbf{v_1}$ and the energy $E_1 = K_{M_T} E_0$. The target-atom has the velocity $\mathbf{v_2}$ and the energy E_2.

Using conservation of energy and momentum, the energy, E_1, of the projectile after the collision can be calculated. For $M_P \leq M_T$ the kinematic factor, which is defined as the ratio between E_1 and E_0, is given by

$$K_{M_T} \equiv \frac{E_1}{E_0} = K_{M_T}(\Theta, M_P/M_T)$$
$$= \left[\frac{\sqrt{1-[(M_P/M_T)\sin\Theta]^2} + (M_P/M_T)\cos\Theta}{1+(M_P/M_T)}\right]^2 \quad . \qquad (5.1)$$

K_{M_T} decreases with decreasing ratio M_P/M_T and with increasing scattering angle Θ. The variation of K_{M_T} with M_T determines the mass-resolution of the method; the larger dK_{M_T}/dM_T, the better is the mass-resolution.

Scattering of the projectile-ion by target-atoms located at the surface results in the detected energy $E_{det} = E_1 = K_{M_T}E_0$.

5.2 The (Differential) Cross Section

So far, only the energy loss of the projectile as a result of a scattering event has been considered. However, this does not provide information about the *scattering-probability* for the event. The latter is given by the *differential scattering cross section*, $d\sigma/d\Omega$. Considering only scattering due to Coulomb interaction between the two masses and assuming $M_P \ll M_T$, $d\sigma/d\Omega$ reads

$$\left(\frac{d\sigma}{d\Omega}\right) = \left(\frac{Z_P Z_T e^2}{16\pi\epsilon_0 E}\right)^2 \frac{4}{\sin^4\Theta} \times \frac{\left[\sqrt{1-[(M_P/M_T)\sin\Theta]^2} + \cos\Theta\right]^2}{\sqrt{1-[(M_P/M_T)\sin\Theta]^2}} \qquad (5.2)$$

Here, Z_P and Z_T are the atomic numbers of the projectile- and of the target-atoms, respectively, e is the elementary charge, and ϵ_0 is the dielectric constant. Eq. 5.2 contains the $1/\sin^4\Theta$-dependence, typical for Rutherford-scattering and was derived as early as 1911 by Rutherford [58].

The main characteristics of Eq. 5.2 are

1. $d\sigma/d\Omega \propto Z_P^2$. This implies that the count rate increases strongly using ions with higher atomic number as projectiles.

2. $d\sigma/d\Omega \propto Z_T^2$. This implies that the count rate of high-Z elements is much higher than that for low-Z elements.

3. $d\sigma/d\Omega \propto E^{-2}$. The higher the projectile energy the lower is the count rate.

4. $d\sigma/d\Omega$ is essentially proportional[1] to $1/\sin^4\Theta$. This implies that for smaller scattering angles the count rate increases dramatically.

As an example, the probability for the backscattering of a single $\alpha-$particle impinging on a silicon surface with an energy of 2 MeV under a scattering angle of $\theta = 172°$ is $p = 3.3 \times 10^{-13}$.

5.3 Energy Loss in Matter

Since the probability for (back)scattering by the target-atoms is small, the projectile will penetrate the surface of the sample. Inside the sample, the ion loses energy mostly due to *electronic* interaction with the electrons of the target atoms. The electronic stopping power (i.e., energy loss dE per length dx) was calculated in the 1930s by Bethe and Bloch and reads

$$\begin{aligned} -\frac{dE}{dx}(E) &= N\frac{Z_P^2 Z_T e^4}{4\pi\epsilon_0^2 v^2 m_e} \\ &\times \left[\ln\frac{2m_e v^2}{\overline{I}} - \ln\left(1-\frac{v^2}{c^2}\right) - \frac{v^2}{c^2}\right]. \end{aligned} \tag{5.3}$$

[1]The differential cross-section is not infinite for $\Theta \to 0$ as suggested by Eq. 5.2. A careful calculation of the cross-section has to take into account the electrical 'shielding' of the atomic nucleus by the electron-cloud. Projectile-atoms, which do not hit the target-nucleus in its center, 'feel' a Coulomb-charge smaller than Z. This results in a deviation of the true differential cross-section from Eq. 5.2 for small Θ.

Here, Z_P and Z_T are the atomic numbers of the projectile ion and of the target atom, respectively, N denotes the atomic density of the target atoms, m_e is the mass of an electron, v and c are the velocity of the projectile ion and the speed of light, respectively. $\overline{I}$ finally is the mean ionization potential for electrons which can be estimated as $\overline{I} = 11.5 \cdot Z_T$ (eV) [55].

5.3.1 The energy distribution in RBS spectra

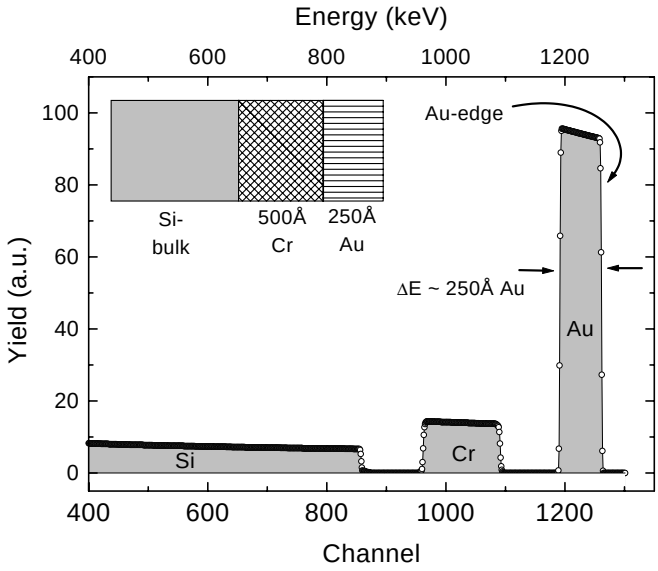

Figure 5.2: Simulation of an ideal RBS-spectrum for a sample Au(250 Å) / Cr(500 Å) / Si(bulk) probed by He^+-ions with an energy of $E_0 = 1.3$ MeV, $\theta_1 = \theta_2 = 37.5°$, i.e., $\Theta = 75°$ and an energy-resolution of $\Delta E = 2.4$ keV. The Au-edge is indicated and corresponds to $E_{Au,edge} = K_{M_{Au}} E_0$. The width of the peaks corresponds to the thickness of the respective layer (indicated for the Au-peak). The Cr-edge and the Si-edge are shifted to energies *smaller* than $K_{M_{Cr}} E_0$ and $K_{M_{Si}} E_0$ due to energy loss of the ions in the layers above.

Combining the above three processes, the resulting RBS-spectrum can be explained. Details about how a simulation of an RBS-spectrum is obtained can be found in [59, 60]. As an example, Fig. 5.2 displays an ideal RBS-spectrum for a sample Au(250 Å) / Cr(500 Å) / Si(bulk) probed by He^+-ions with an energy of $E_0 = 1.3$ MeV, $\theta_1 = \theta_2 = 37.5°$, i.e., $\Theta = 75°$ and an energy-resolution of $\Delta E = 2.4$ keV which has been simulated using the standard RBS-analysis-software 'RUMP'[2].

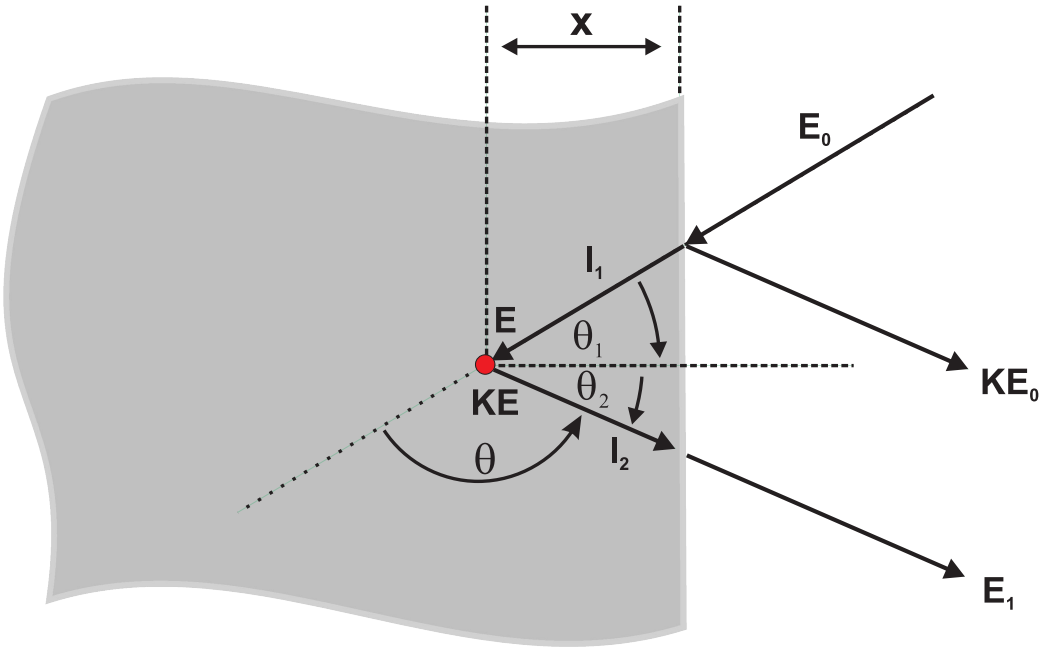

Figure 5.3: Schematic for the detected energy for an ion scattered at the surface and an ion scattered in depth x. For explanations see text.

Consider a sample with only one sort of atoms with atomic number Z_T and mass M_T and projectile ions with atomic number Z_P, mass $M_P \ll M_T$

[2]Usual RBS-analysis-programs such as 'RUMP' assume single scattering of the projectile only. If multiple scattering effects are to be included, time-consuming Monte-Carlo simulations had to be applied.

and incident energy E_0. Furthermore, let the incident angle be θ_1 and the exit angle be θ_2, both with respect to the surface normal. The scattering angle θ is then given as $\theta = 180° - (\theta_1 + \theta_2)$ (see Fig. 5.3).

In the RBS spectrum the number of scattering events with a specific energy is recorded. The different energies can be related to a distinct depth by the following considerations:

1. The highest recorded energy corresponds to scattering from the surface. It will be $E_{edge} = K_{M_T} \cdot E_0$. At E_{edge}, an edge appears in the spectrum. Its position is characteristic for the specific target element.

2. An ion that penetrates the sample loses energy on its way into the sample with length $l_1 = x/\cos\theta_1$. At a depth of x, the ion hits a target-atom and is scattered. Under the assumption of a constant stopping power dE/dx along its way into the sample, the ion has an energy just before the scattering of

$$E = E_0 - l_1 \left.\frac{dE}{dx}\right|_{in} . \tag{5.4}$$

   Then the ion is scattered and the energy just after the scattering reads $K_{M_T}E$.

3. Now the ion has to travel back through the sample to the surface. Again it loses energy along its way of length $l_2 = x/\cos\theta_2$. Under the assumption of a constant stopping power dE/dx along l_2 the energy at which the ion is detected after it finally has left the sample can be calculated:

$$\begin{aligned} E_1 &= K_{M_T}E - l_2 \left.\frac{dE}{dx}\right|_{out} \\ &= K_{M_T}E_0 - \left(\frac{K_{M_T}}{\cos\theta_1} \left.\frac{dE}{dx}\right|_{in} + \frac{1}{\cos\theta_2} \left.\frac{dE}{dx}\right|_{out} \right) \cdot x \end{aligned} \tag{5.5}$$

Therefore, ions recorded with energies smaller than the 'edge-energy' $K_{M_T}E_0$ are associated with scattering events inside the sample. It is possible to relate the energy-scale to a depth-scale. In combination with the knowledge of the (energy dependent) scattering cross section, concentration profiles of specific elements can be determined to study, e.g., diffusion-processes. Furthermore, shifts of the element-specific edge-energy to lower energies are a clear sign for a cover-layer above the inspected element.

Chapter 6

Experimental Details

6.1 Sample Preparation

In the experiments, diindenoperylene (DIP) from Aldrich was used, purified via gradient sublimation in the 'Kristallabor' of N. Karl at Stuttgart University. The purified material was evaporated at about 330°C with custom-made Knudsen-cells in an OMICRON-MBE-system (Fig. 6.1) onto the substrates under normal incidence.

6.1.1 The MBE system

For sample preparation and *in situ* surface analysis an OMICRON-MBE and -analysis system was used (see Fig. 6.1). The system has three individually pumped UHV-chambers connected to each other to allow for sample transfer without breaking the vacuum.

A small load-lock chamber is used for sample transfer between the laboratory and the OMBE-system without breaking the vacuum of the MBE- and analysis-part of the system.

Up to four Knudsen-cells (see Sec. 6.1.2) can be mounted to the MBE-

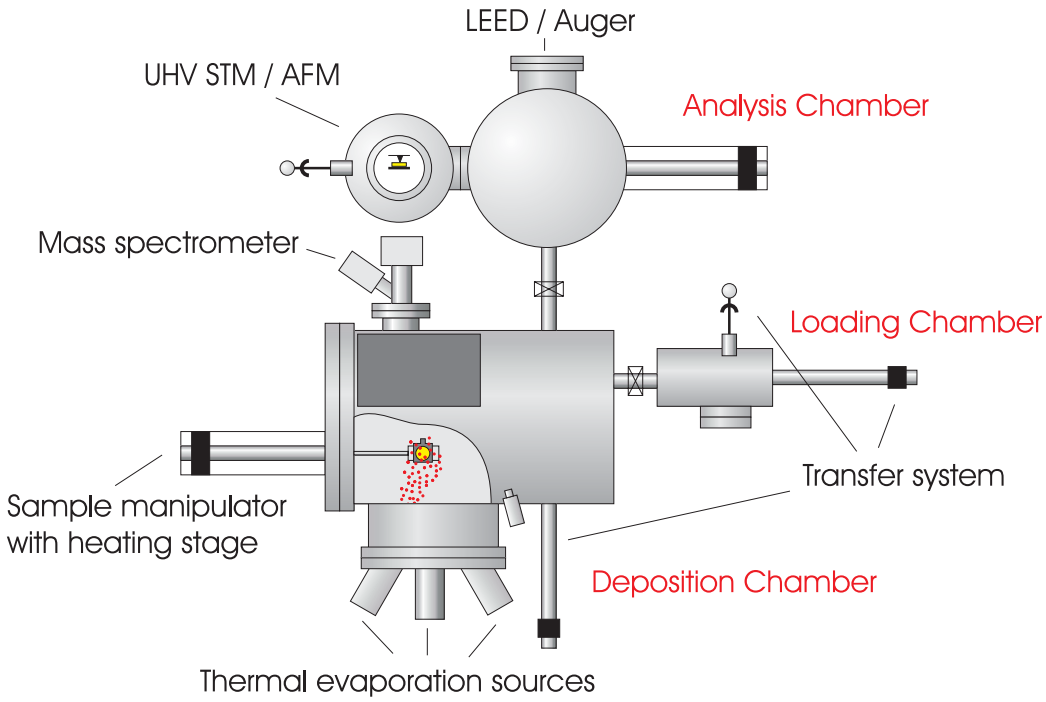

Figure 6.1: OMICRON MBE-system. Three separated UHV-chambers allow for the growth of samples, analysis of the samples and for transfer of samples from/to the laboratory via the load-lock chamber without breaking the vacuum of the system. The growth and analysis chambers are operated at a base pressure of $\approx 2 \times 10^{-10}$ mbar and $\approx 2 \times 10^{-11}$ mbar, respectively.

chamber operated at a base pressure of $\approx 2 \times 10^{-10}$ mbar. The samples are attached to a manipulator allowing for translation and rotation of the sample as well as for heating (up to 850°C) and cooling (down to −150°C). The substrate on the manipulator is at a distance of about 40 cm from the evaporation-cell aperture. During deposition at a vacuum of better than 2×10^{-9} mbar the film-thickness and the deposition rate are monitored by a quartz-microbalance (*MDC*).

After deposition the samples could be transferred to the analysis cham-

ber ($p \approx 2 \cdot 10^{-11}$ mbar). A non-contact atomic force microscope (NC-AFM) is employed to characterize the surface morphology immediately after deposition (see Figs. 6.2 and 6.3 for a schematic of the NC-AFM measurement and for a photograph of the OMICRON instrument). Note, however, that for DIP-films the surface morphology does not change after exposure to air (even after several months), as checked for several samples.

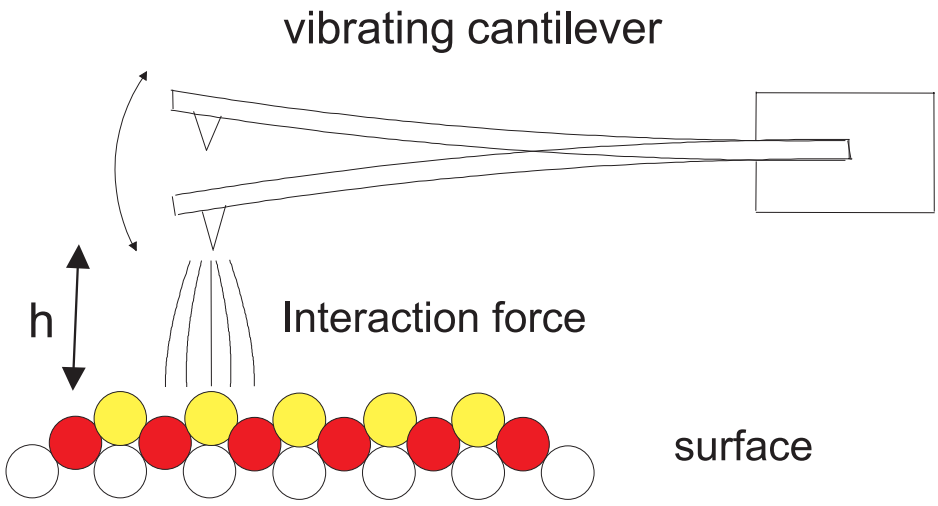

Figure 6.2: Schematic of NC-AFM measurements.The cantilever's resonance frequency is a function of the interaction forces between sample-surface and cantilever. These interaction forces are proportional to the distance between cantilever and surface, h. Thus, the surface topography can be determined by measuring small changes in the resonance frequency of the cantilever.

6.1.2 The evaporation cells

The materials used for the preparation of the thin films (i.e., DIP and gold) were thermally evaporated by Knudsen-cells. Fig. 6.4 shows the simple design of such a cell.

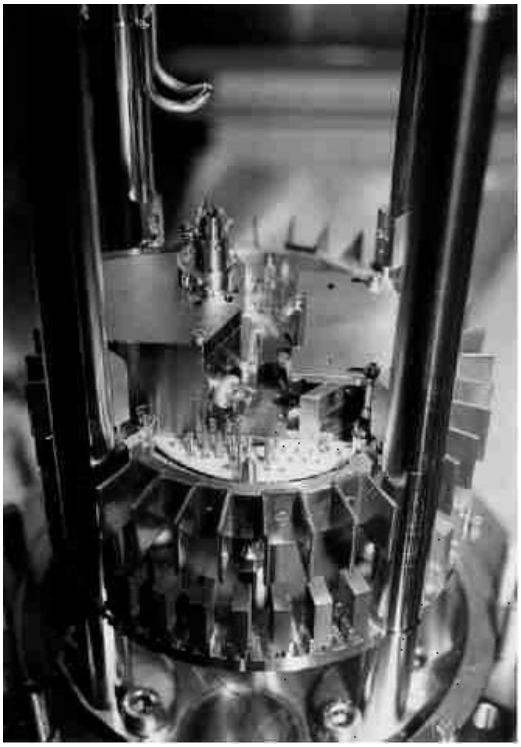

Figure 6.3: Side view of the OMICRON AFM

To evaporate the organic material DIP a custom-made Knudsen-cell was used, designed by K. A. Ritley. The evaporation temperature is monitored by a K-type thermocouple. Gold was evaporated from a water-cooled commercial Knudsen-cell (*CreaTec HTC-40-5-168-SH*). The temperature is monitored by a C-type thermocouple.

The cell-temperature was controlled by a Eurotherm (*Eurotherm 2408*) temperature controller with a relative precision of $\Delta T \lesssim 1°\mathrm{C}$.

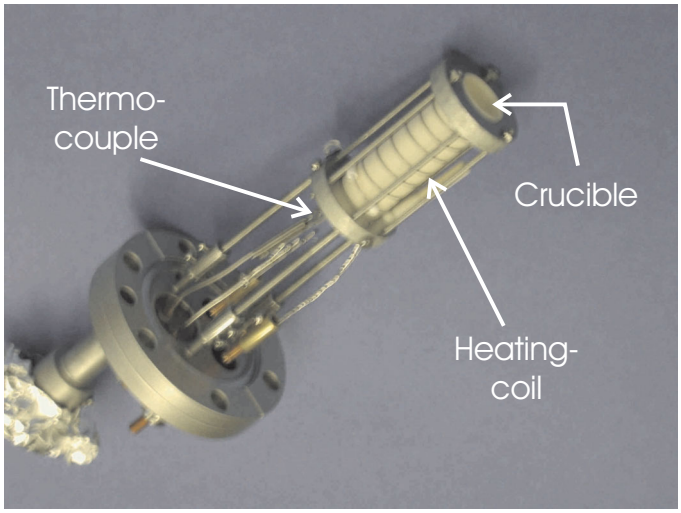

Figure 6.4: Photo of a custom-made evaporation cell used for the evaporation of DIP. For operation in the OMBE the cell is equipped with two tantalum heat-shields and a shutter.

6.1.3 Substrates

The samples were prepared on two different types of substrates with dimensions of $\approx 10 \times 10$ mm^2:

1. Thermally grown silicon-oxide on Si(100). The silicon wafers had (100)-orientation with a miscut of 0.5° and were covered with a thermally grown SiO_2-layer of 4000 Å in thickness. The substrates were cleaned in acetone and dried in a stream of nitrogen. Prior to deposition of the organic material the substrates were heated in UHV above 750°C for a minimum of 12 hours.

2. Sapphire (A-plane). To investigate whether an epitaxial relationship of the DIP-molecules with a substrate can be found, some samples were prepared on A-plane sapphire ($(11\bar{2}0)$-orientation). The substrates were

cleaned in acetone, dried in a stream of nitrogen and heated under UHV-conditions to over 750°C for a minimum of 12 hours prior to film deposition.

Details of the film-deposition parameters (DIP and gold deposition) are given in Tables C.1 and 9.1, respectively.

6.2 X-Rays

Most of the x-ray measurements have been carried out at the European Synchrotron Radiation Facility (ESRF) in Grenoble, France, and at the Hamburg Synchrotron Laboratory (HASYLAB) in Hamburg, Germany.

The ESRF is a state-of-the-art 3rd generation synchrotron with the electron storage ring being operated at 6 GeV. After injection the typical electron current is 200 mA with a lifetime of about 55 h. The experiments have been performed at the high-brilliance multi-purpose Troïka beamline (undulator).

The Synchrotron HASYLAB is a 2nd generation 4.4 GeV electron storage ring which operates at a typical electron current of 100 mA. The experiments at HASYLAB have been carried out at the wiggler beamline W1.

Table 6.1 summarizes the main parameters of the employed synchrotron beamlines. The longitudinal coherence length is calculated using the relation $\xi_{long} = \frac{\lambda}{2} \cdot \Delta E/E$. The transverse coherence length given in Table 6.1, ξ_{trans}, is a lower limit. It was calculated using the FWHM, $\Delta\Theta$, of the rocking-curve of the (111)-reflection of a silicon-wafer at sample position (i.e., behind the complete beamline optics). This procedure provides an upper limit for the beam divergence of the respective beamline at sample position[1]. ξ_{trans} is then

[1]This assumption holds true due to the very high monochromaticity of the radiation. Then, the upper limit for the divergence of the beam is given by the width of the rocking curve on a Bragg-reflection of a (nearly) perfect crystal like a silicon-wafer. If the rocking width was limited by the perfection of the crystal, i.e., by its Lorentz-width, then the

parameter	Troïka II	W1
λ (Å)	1.563(2)	1.390(2)
$\Delta E/E$	6×10^{-5}	2.2×10^{-4}
slit settings (detector)		
vertical '=' (mm)	0.2	0.4
horizontal '‖' (mm)	4	4
rocking width of Si(111)-reflection		
$\Delta\Theta$ (deg)	0.003	0.007
coherence length of the beam:		
ξ_{long} (Å)	≈ 13000	≈ 3200
ξ_{trans} (Å)	≥ 14900	≥ 5700

Table 6.1: Beamline-characteristics for Troïka II (ESRF) and W1 (HASYLAB). The values λ, $\Delta 2\Theta$, and $\Delta\Theta$ were measured during the alignment at the Si(111)-reflection. Values $\Delta E/E$ are from beamline-information homepages. ξ_{trans} and ξ_{long} are given for the beam impinging perpendicular onto the sample. ξ_{trans} may be much larger at small incident angles due to projection effects (see also text).

calculated by the relation $\xi_{trans} \approx \lambda/2\Delta\Theta$ [46]. Note that the transverse coherence length in a specific experimental situation is the projection of ξ_{trans} to the sample. For specular rod measurements it is given by $\tilde{\xi}_{trans} = \xi_{trans}/\sin\alpha_i$ and can exceed 50 μm for small angles.

Some additional experiments have been carried out at in-house sources (GID-measurements, sample pre-characterization).

The main features of the x-ray sources are described below. Extensive information about the Synchrotron sources ESRF and HASYLAB as well as

divergence would be even smaller.

the beamlines can be found on the respective webpages[2].

6.2.1 In-house sources

Several in-house x-ray sources were used to characterize the samples. Reflectivity and in-plane measurements were carried out with the sources listed below

1. Mo-K_α radiation (monochromatized by a HOPG-monochromator, $\lambda = 0.71$ Å) at a HUBER 6-circle diffractometer. The x-rays were produced by a Rigaku 18 kW rotating anode x-ray generator.

2. Co-K_α radiation (monochromatized by a HOPG-monochromator, $\lambda = 1.7921$ Å) at a small HUBER 4-circle diffractometer with an Eulerian cradle. The x-rays were produced by a sealed tube anode.

6.2.2 Synchrotron sources

Troïka II beamline (ID10B) at ESRF in Grenoble

The beamline ID10B at the ESRF in Grenoble is a high-brilliance multipurpose beamline. The diffractometer is optimized for scattering from surfaces and interfaces using grazing-incidence diffraction and reflectivity in both horizontal and vertical scattering geometry. The experiments were carried out at a wavelength $\lambda = 1.5632$ Å in vertical scattering geometry (i.e., with the sample mounted horizontally) so that the polarization factor could be neglected in the evaluation of the data. The specular rod and diffuse scattering on DIP-films of various thickness have been measured at this beamline.

Fig. 6.5 shows a schematic of the Troïka II beamline setup. The white beam is monochromatized by a double-crystal monochromator (diamond(111)) which gives an intrinsic energy resolution of $\Delta E/E = 6 \times 10^{-5}$.

[2]http://www.esrf.fr and http://www-hasylab.desy.de

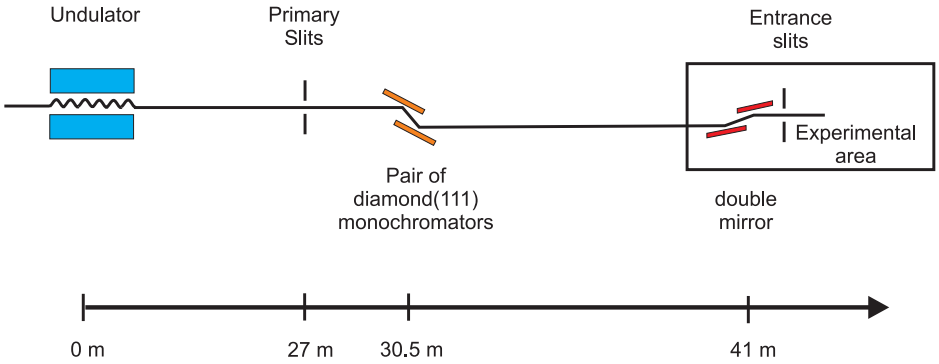

Figure 6.5: Schematic of the Troïka II beamline setup at the ESRF

A pair of mirrors can be used to suppress higher harmonics. The beam size at sample position exhibits a cross-section of $< 1 \times 0.5$ mm^2 (H×V). The photon flux at the sample is 10^{11} photons/s at 100 mA and a beam energy of 8 keV.

A small cell with 360° Kapton-window and a constant stream of helium served as sample environment to suppress air-scattering during the measurements. Without sample, the measured background (i.e. 'air-scattering') in this setup was negligible.

W1 beamline at HASYLAB in Hamburg

The beamline W1 at HASYLAB is a multi-purpose beamline. The diffractometer is optimized for scattering from surfaces and interfaces using grazing-incidence diffraction and reflectivity in both horizontal and vertical scattering geometry. The experiments were carried out at a wavelength $\lambda = 1.3920$ Å in vertical scattering geometry (i.e., with the sample mounted horizontally) so that the polarization factor could be neglected in the evaluation of the data. At this beamline, temperature dependent reflectivity and Bragg scattering experiments on the heterostructure samples (gold on DIP) were carried

out in several runs. In addition, the thermal expansion coefficient of DIP in uncapped DIP-films was determined at beamline W1.

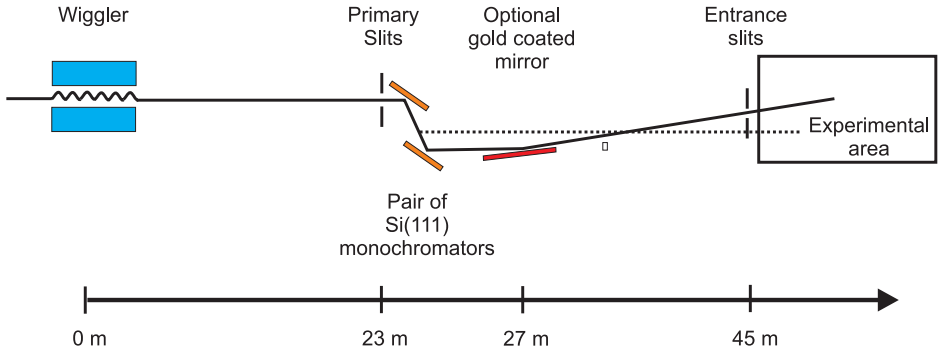

Figure 6.6: Schematic of the W1 beamline setup at HASYLAB

Fig. 6.6 shows a schematic of the W1 beamline setup. The white beam is monochromatized by a double-crystal monochromator (Si(111)) which gives an intrinsic energy resolution of $\Delta E/E = 2.2 \times 10^{-4}$. The monochromatic beam may enter the experimental hutch directly (dotted line in Fig. 6.6) or can be reflected upwards to be focused by a gold coated toroidal mirror (straight line in Fig. 6.6). Higher harmonics are suppressed by this mirror and/or by proper adjustment of the energy window of an energy discriminator after the NaJ-scintillation detector. The beam size was set to a cross-section of 40×1 mm^2 (H×V) in front of the mirror by the primary slits and to 4×0.2 mm^2 (H×V) at sample position by the entrance slits. The flux at the sample is approximately 10^9 photons s^{-1} mm^{-2}.

For the temperature dependent measurements the samples were mounted horizontally in a small vacuum chamber ($p \approx 1 \times 10^{-6}$ mbar) with a Kapton-window. The sample station (Ta-plate, 0.5 mm thick) could be heated up to $T = 300$°C with the temperature being measured by a C-type thermocouple mounted close to the sample. The precision of the absolute temperature-measurement was approximately 3 K, the precision of relative temperature

measurements was better than 0.3 K.

6.3 Cross-Sectional Transmission Electron Microscopy (TEM)

In order to investigate the interfacial morphology of gold-DIP heterostructures, cross-sectional TEM measurements were employed. Electron microscopy is based on the wave-character of electrons with wavelength in the Å-range. Thus it is possible to obtain high-resolution images of solid samples. The electrons are accelerated by a high voltage to a given energy (i.e., a given wavelength). The latter determines the resolution. A comprehensive introduction to this field can be found in Refs. [61–63].

Sample preparation is crucial for good TEM-images since the probed spot in transmission geometry must not exceed a thickness of ≈ 100 nm. Otherwise the electron beam is completely absorbed by the sample. In particular, preparation of samples with organic thin films is difficult. Careful attention and experience are needed to prepare suitable TEM-samples. High temperatures ($< 100°C$) must be avoided and the use of organic solvents as well as the amount of mechanical treatment (e.g., by sawing, by grinding, etc.) of the sample have to be minimized.

The main steps of sample preparation as well as the microscopes used to investigate the samples are described below.

6.3.1 Sample preparation

All samples investigated by cross-sectional TEM were prepared in the following way:

1. A small slice of the sample is cleaved into two pieces.

2. The two pieces are glued together and the glue (*Gatan G1*) is stabilized in an oven at T = 70°C for 2 hours resulting in a sandwich consisting of the layers Si/SiO_2/DIP/Au/glue/Au/DIP/SiO_2/Si.

3. The sandwich is fixed in a copper tube with 3 mm diameter (see Fig. 6.7)

4. The copper tube is sliced with a diamond wire saw into thin slices of about 500 μm thickness.

5. The thin slices are grinded and polished on both sides to a final thickness of ≈ 80 μm

6. The sample is dimple-grinded to a thickness of ≈ 20 μm (see Fig. 6.7 for an example)

7. In an ion-mill the sample is thinned until the thickness of the Au/DIP-layer is in the range of 10 . . . 100 nm and then is transparent for electrons

While the above preparation route is essentially standard for inorganic systems, its application to organic systems requires special care.

In step 2, it is particularly important to use an epoxy-glue which stabilizes at comparatively low temperatures ($T \ll 100$°C) in a short time in order to minimize the time the organic film is exposed to elevated temperatures.

Grinding and polishing the thin slice in step 5 implies fixing the sample onto a sample holder with a thin layer of wax (for each side once). After the polishing procedure, the wax has to be removed with acetone. In this step one has to take care that (a) the sample is fixed quickly onto the sample holder which is kept at $T \approx 130$°C in order to melt the wax and (b) the amount of acetone used to remove the wax is minimized since acetone may dissolve the organic film.

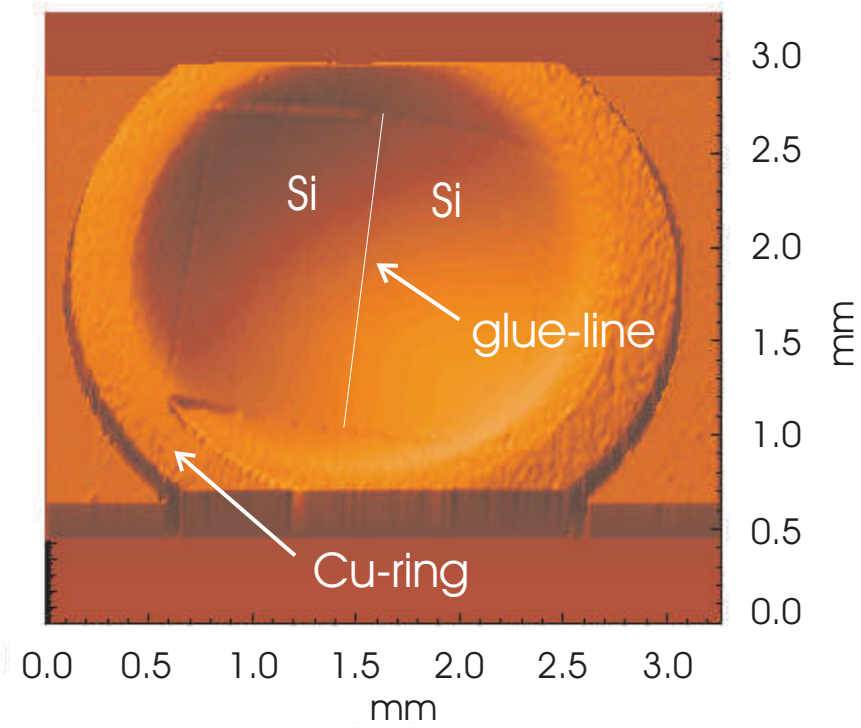

Figure 6.7: 3D-profile of a prepared TEM-sample just before insertion into the ion-mill. The glue-line (indicated as white line) is the center of the sandwich-structure and contains the parts SiO_2/DIP/Au/glue/Au/DIP/SiO_2.

Finally it is preferable to cool the sample during the ion-milling process (step 7), again, to minimize thermal exposure of the organic film. For our samples, the samples were cooled by liquid nitrogen.

Note, that also the choice of the substrate has to be considered carefully. Extremely hard substrates (e.g., sapphire) require a long grinding-process until their thickness is reduced sufficiently. Since the duration of the mechanical treatment also should be kept to a minimum, less hard substrates such as silicon are preferable.

With the above described procedure, cross-sectional TEM samples of several different Au/DIP-structures have been successfully been prepared. Usually, several TEM-samples are prepared of a single Au/DIP-sample since only 30-50% of them give reasonable images.

6.3.2 Instruments

The samples were measured with a CM200 microscope (Philips) operated at 200 keV and with a JEM 4000 FX microscope (JEOL) operated at 400 keV, respectively. Both instruments were equipped with a LaB_6-cathode which produced the electrons. The point-resolution was 2.7 Å (CM200) and 2.0 Å (JEM 4000 FX), respectively. The samples exhibited a stability against the electron beam of $1 \ldots 2$ minutes, sufficient for taking representative photographs of the interface (the exposure time for photographs was $1 \ldots 3$ seconds). Note, that the stability of the samples was larger by a factor of ≈ 2.5 in the JEM 4000 FX microscope compared to the CM200. The stability may be increased in further experiments by cooling the sample to LN_2-temperature during the measurements.

6.4 RBS

6.4.1 The Stuttgart Pelletron

The RBS measurements were performed at the Stuttgart Pelletron, which is described elsewhere in detail [64,65]. In brief, He^+-ions of 1.3 MeV were used and the scattering angles were $\theta_1 = \theta_2 = 37.5°$, therefore the scattering angle θ was $\theta = 75°$ (see Fig. 5.3 for the definition of the angles). To provide a good depth resolution the high-resolution spectrometer was used as detector [66]. An energy resolution of 2.4 keV was obtained corresponding to a depth resolution of ≈ 10 Å in the gold layer.

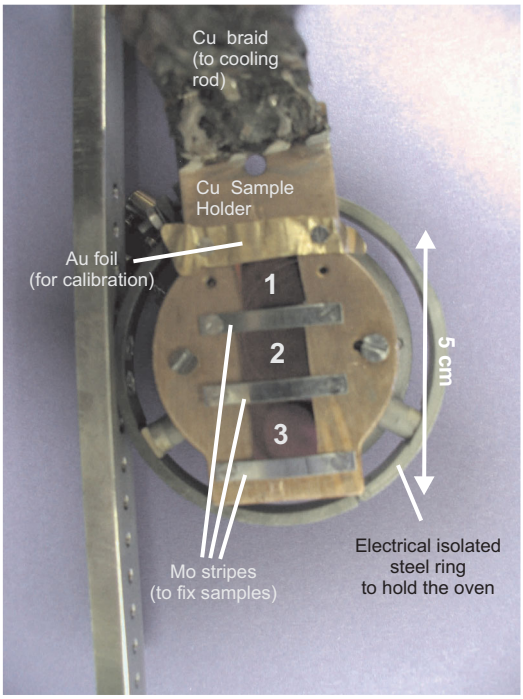

Figure 6.8: Photograph of the RBS sample-holder

A special sample holder was constructed for the RBS measurements (see Fig. 6.8). Up to 4 samples can be accommodated in a vertical arrangement on a Cu-plate (1 mm thick), which guarantees good thermal conductivity. This arrangement gives access to the different samples moving them only in $z-$direction. The individual samples could exhibit a maximum size of 10×10 mm^2 and are mounted on the copper plate by molybdenum-stripes ($\approx 14 \times 2$ mm^2) or by a thin foil of gold (for calibration purposes). To facilitate a fast cooling of the sample holder after annealing, the Cu-plate was connected to a cooling-finger ($-20°$C) via a broad Cu-braid.

6.4.2 *In situ* sample preparation

Prior to the RBS-experiment the gold layer was deposited on top of the DIP-film *in situ*. The base pressure of the system was better than 2×10^{-8} mbar. Gold was evaporated from a tiny droplet of gold situated in a tungsten filament at room temperature with a rate of 1 Å/min. Measurements were performed immediately after preparation and after annealing. After each temperature treatment (1 hour at a given temperature) the sample was cooled down to room temperature and measured again. To exclude the influence of ion-induced damages, the data were compared to measurements at previously unprobed spots from time to time.

Chapter 7

Structure of DIP-Thin-Films

7.1 First AFM-, Cross-Sectional TEM-, High-Resolution X-Ray, and Spectroscopic Ellipsometry Investigations

Deposited under suitable conditions ($T_{Sub} \approx 150$°C, $R \approx 12$ Å/min) on thermally oxidized (4000 Å) silicon wafers with (100)-orientation or on A-plane sapphire ($Al_2O_3(11\bar{2}0)$)[1], DIP thin films show excellent crystalline order in the direction perpendicular to the substrate surface as demonstrated by cross-sectional TEM (Fig. 7.1) and by specular x-ray scattering (Fig. 7.2) [67].

The latter show DIP Bragg-reflections up to the 7th...9th order, giving a lattice constant for the DIP-monolayers of $d_{DIP} \approx 16.5$ Å, which suggests essentially upright standing molecules. Furthermore, comparing the Kiessig-fringes with the Laue-oscillations around the DIP(001) Bragg-reflection (inset of Fig. 7.2), the same periodicity is obtained for both oscillations, i.e., the investigated DIP-films are coherently ordered across their entire thickness.

[1]Details on the sample denotation and on the thickness of individual DIP-films can be found in Table C.1.

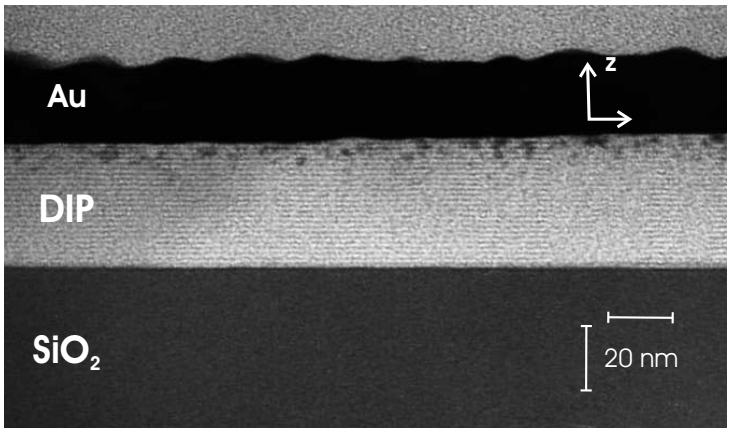

Figure 7.1: Cross- sectional TEM-image of a DIP thin film ($D_{DIP} = 390$ Å) deposited on a thermally oxidized (4000 Å) Si(100) substrate. Each pair of black and white stripes is related to one monolayer of the essentially upright-standing DIP-molecules with $d_{DIP} = 16.5$ Å. The image was taken using a JEOL FX 4000 electron-microscope at 400 keV. Notice that in this sample (sample A1, Table 9.1) the DIP-film has been overgrown with a Au cap (as a potential electrical contact, see also Chapter 9). The dark features in the DIP-layer at this interface are due to interdiffused gold-clusters in the DIP-layer.

In addition, the almost undamped Laue-oscillations around the DIP(001) Bragg-reflection (Fig. 7.3) demonstrate that the thickness of the DIP-grains in the film is very homogeneous.

Remarkably, individual DIP-monolayers are visible in the TEM-image as pairs of black and white stripes (Fig. 7.1) with the reported lattice constant. This is a consequence of the high structural order with mosaicities as small as $0.0087° \pm 0.0003°$ (inset of Fig. 7.3), which is an extraordinarily small value

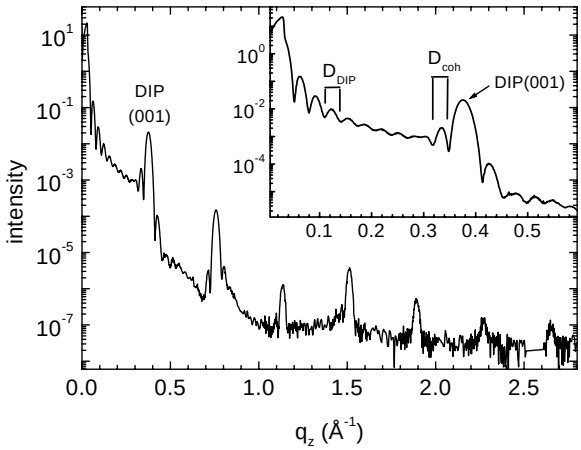

Figure 7.2: Specular x-ray intensity of a typical DIP thin film. Out-of plane Bragg-reflections up to the 7th order are seen. The inset shows a magnification from total external reflection up to the first DIP Bragg-reflection, which shows $D_{DIP} = D_{coh}$ (sample 'o206').

for organic thin films.

In Fig. 7.4 the surface topology of a DIP-film is displayed as probed by NC-AFM. The image shows a closed DIP-film with large planar terraces extended to several 100 nm which are separated from each other by monomolecular steps of $\approx$ 16.5 Å. These steps are particularly well seen at the left-hand side of the profile-line, which follows the black solid line in Fig. 7.4. The surface roughness of this film is $\sigma = 28 \pm 3$ Å which corresponds to less than two MLs of DIP.

Spectroscopic ellipsometry measurements were carried out on DIP thin-films to determine the optical band-gap of this organic semiconductor (Fig. 7.5)[2]. Since a detailed analysis of the ellipsometric spetra is beyond the scope

[2]In cooperation with M. I. Alonso and M. Garriga, Institut de Ciencia de Materials de

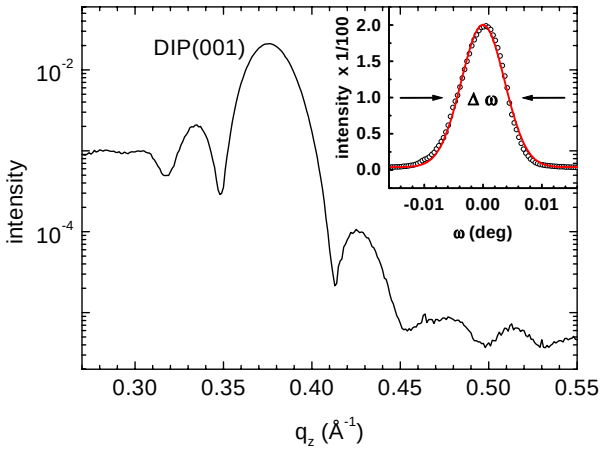

Figure 7.3: Radial scan over the DIP(001) reflection which show pronounced Laue-oscillations. The inset is a rocking scan over the DIP(001) reflection with a FWHM of only $0.0087° \pm 0.0003°$ (sample 'o206').

of this thesis, only the most relevant parameters of the respective measurements are outlined briefly (for details see Refs. [68, 69]).

In a rotating polarizer (or analyzer) ellipsometer, the relevant measured quantities are $\tan\Psi$ and $\cos\Delta$, where the ellipsometric magnitudes Ψ and Δ describe the ratio between the reflected χ_r , and incident χ_i, light polarization states

$$\frac{\chi_i}{\chi_r} = \tan\Psi e^{i\Delta} \tag{7.1}$$

This ratio is determined as a function of energy at a fixed incident and exit angle ϕ with respect to the surface normal (for the measurements presented in this thesis, $\phi = 60°$).

It is now possible to determine, inter alia

Barcelona, CSIC, 08193 Bellaterra, Spain.

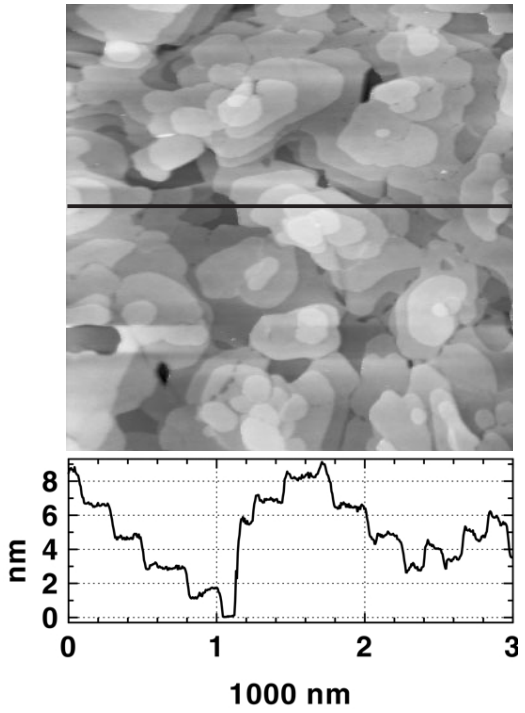

Figure 7.4: AFM-image of a thin DIP-film (D_{DIP} = 396 Å, sample 'o396'). Large terraces extended to several 100 nm are seen with monomolecular steps of ≈ 16.5 Å.

1. the optical band-gap $E_{g,opt.}$ using the parameter $\tan\Psi$: the first increase of $\tan\Psi$ (indicated by the arrow in Fig. 7.5) indicates the necessary absorption energy, which corresponds to the optical gap.

2. optical anisotropies which are related to structural anisotropies: significant differences in the spectra taken from the sample in a certain azimuthal orientation ('0°') and the spectra from the sample rotated by 90° around its surface normal ('90°') are evidence for a structural anisotropy in the film parallel to the surface (e.g., a preferential orien-

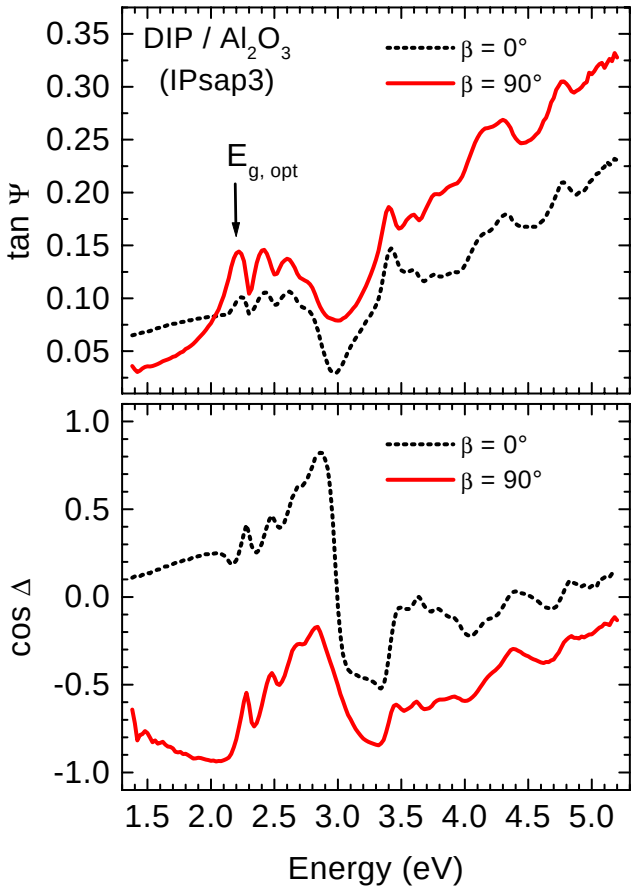

Figure 7.5: Spectroscopic ellipsometry on a DIP-film grown on A-plane sapphire (sample 'IPsap3'). The optical bandgap of $E_{g,opt.} = (2.2 \pm 0.1)$ eV is seen as well as the optical anisotropy under an azimuthal rotation of the sample of 90°. The incidence angle was $\phi = 60°$ and β is given with respect to the (in-plane) sapphire c-axis (measurements carried out by I. Alonso).

tation).

3. geometric information about the sample (e.g., film thickness)

The ellipsometric measurements give an optical band-gap[3] for DIP thin films of 2.2 ± 0.1 eV.

Furthermore, Fig. 7.5 shows a pronounced anisotropy in the ellipsometric parameters for the DIP-film deposited on A-plane sapphire (sample 'IPsap3'). This suggests a preferential orientation of the DIP-molecules in the film parallel to the surface, which is presumably induced by the crystalline orientation of the sapphire-substrate and which rules out polycrystalline order in the film.

7.2 Quantitative Analysis of Specular X-Ray Measurements

In this section the out-of-plane structure of the highly crystalline DIP films is investigated in detail as a function of thickness by quantitatively analyzing high resolution x-ray data. The preparation conditions of the investigated samples with a range of thickness of $69\,\text{Å} \leq D \leq 1100\,\text{Å}$ (denoted '069'...'o1100') are found in Table C.1.

After preparation, the samples were characterized in detail by NC-AFM measurements as well as by specular and diffuse x-ray measurements at beamline ID10B (Troïka II) at the ESRF in Grenoble in France. Analysis of the x-ray reflectivity employing the Parratt-algorithm provides the mean electron density ρ^0_{DIP} of the films as well as their thickness and their rms-roughness. A detailed analysis of the intramolecular electron density distribution along

[3]Note, that the *optical* band-gap, $E_{g,opt.}$, may differ from the *electronic* band-gap, $E_{g,el.}$ by up to 0.5 eV due to the contribution of the exciton-binding energy, which cannot be neglected in organic semiconductors [70].

the z-axis of the DIP molecules in the films is carried out using the Master formula to fit the complete specular rod data of the various films.

7.2.1 X-ray reflectivity

First, the (small angle) x-ray reflectivity of the individual samples was measured in a specular scan ($q_x = q_y = 0$); the diffuse intensity was obtained employing a so-called 'offset scan'. For the latter, at a given value of $2\Theta = \alpha_i + \alpha_f$ the incident angle α_i was slightly offset with respect to the specular condition as $\alpha_i = 2\Theta/2 \pm \Delta\omega_{off}$ with $\Delta\omega_{off} = 0.03°$.

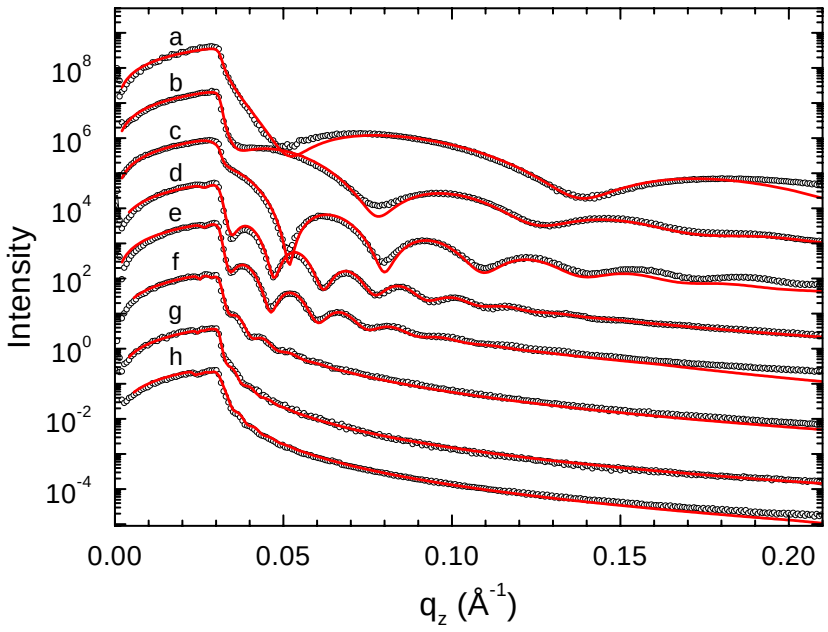

Figure 7.6: Reflectivity data and fits according to the Parratt-algorithm, (a) o69, (b) o126, (c) o206, (d) o385, (e) o396, (f) o670, (g) o970, (h) o1100

The offset data were subtracted from the specular scan data to yield the

'true' specular intensity. Fig. 7.6 displays the data and fits to the data as obtained by the Parratt-algorithm; the fitting parameters are listed in Table 7.1. Due to the oscillating electron density in the DIP film the simple box-model which assumes a constant electron density ρ^0_{DIP} along the complete DIP-film failed to fit the data already at comparatively small momentum transfers $q_z \approx 0.20$ Å^{-1}. This is seen in particular at the right hand side of the curves (a), (c), (e), and (h) in Fig. 7.6. Here, the intensity of the first out-of-plane DIP Bragg reflection (located at $q_z \approx 0.38$ Å^{-1}) which is not taken into account by the simple box-model already cannot be neglected. Nevertheless, the fitting parameters D_{DIP}, σ_{DIP}, ρ^0_{DIP}, and β_{DIP} are significant. Whereas D_{DIP} and σ_{DIP} are determined with high accuracy by the distance between individual Kiessig fringes and their damping, the values of ρ^0_{DIP} and β_{DIP} can be determined by careful fitting of the total-reflectivity edge. Slight deviations between fit and data close to the edge of total reflection (as visible in the curves (a) and (b) of Fig. 7.6) are additional evidence that the coarse box-model is insufficient at this level and that a certain gradient in the electron-density most likely is apparent.

7.2.2 Complete specular rod

The high quality of the x-ray data of the DIP films is a consequence of their high structural order. The data contain much more information about the electron density normal to the surface than simply the thickness, the rms-roughness and the mean electron density if also the part $q_z > 0.20$ Å^{-1} is considered. In principle, the DIP-Bragg reflections, their Laue-oscillations and the interference between substrate and film (leading to asymmetries in the Laue-oscillations) for the samples under inspection provide detailed information about the electron-density profile along the surface normal up to a vertical resolution given by $2\pi/q_{z,max}$. To overcome the restrictions of a

sample	D_{DIP} (Å)	σ_{DIP} (Å)	ρ^0_{DIP} (el/Å^3)
'o69'	69.0 ± 1	7.6 ± 0.5	0.327 ± 0.02
'o126'	126.2 ± 1	13.0 ± 1	0.344 ± 0.015
'o206'	206.3 ± 2	15.0 ± 1.5	0.367 ± 0.015
'o385'	384.7 ± 2	23.0 ± 3	0.384 ± 0.01
'o396'	396.5 ± 2	28.0 ± 3	0.39 ± 0.01
'o670'	670 ± 4	53 ± 5	0.402 ± 0.01
'o970'	970 ± 8	65 ± 5	0.39 ± 0.01
'o1100'	1100 ± 10	62 ± 5	0.39 ± 0.01

Table 7.1: Parameters D_{DIP}, σ_{DIP}, and ρ^0_{DIP} as obtained by the Parratt-algorithm. For the remaining parameters the following values were obtained: $\beta_{DIP} = 1.0 \times 10^{-8}$ el/Å^3, $\sigma_{Si} = 1.7 \pm 0.3$ Å, $\rho_{Si} = 0.689$ el/Å^3, and $\beta_{Si} = 2 \times 10^{-7}$ el/Å^3.

coarse box-model as discussed above, the semi-kinematic formalism (Master formula) is used in what follows to make use of the information provided by the complete specular rod. Starting from Eq. 7.5 the formalism to analyze the data was developed in the present thesis.

Linearity of $F(q_z)$ in the Master formula

Due to the linearity of the integral in Eq. 4.21 it is possible to separate the individual contributions of the complete electron profile as follows (see Fig. 7.7):

$$F(q_z) = r_A(q_z) + r_B(q_z)e^{iq_z d_0} + r_C(q_z)e^{iq_z d_0}, \tag{7.2}$$

in which

1. $r_A(q_z)$ is determined by the electron-density contrast between the silicon substrate and the DIP film,

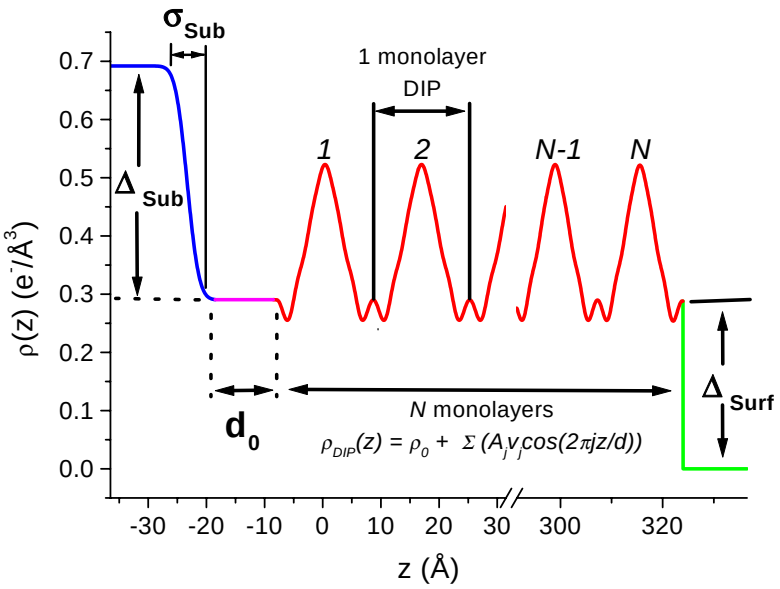

Figure 7.7: Splitting of $F(q_z)$ into $r_A(q_z)$, $r_B(q_z)$, and $r_C(q_z)$

$$r_A(q_z) = \Delta_{Sub} e^{-\frac{1}{2}\sigma_{Sub}^2 q_z^2} \tag{7.3}$$

with Δ_{Sub} being the electron-density contrast between silicon and the electron density of the DIP film at the interface. The roughness of the substrate σ_{Sub} enters $r_A(q_z)$ via the exponential expression in Eq. 7.3

2. $r_B(q_z)$ is the contribution of the oscillatory electron density of the DIP film.

3. $r_C(q_z)$ is associated with the electron density contrast between the surface of the last DIP layer and medium 1 (ρ_1) above the DIP-film (here: vacuum).

The phase factor $e^{iq_z d_0}$ accounts for the distance between substrate surface and the first DIP-monolayer, d_0, which in general is not the same as d_{DIP} (see Fig. 7.8).

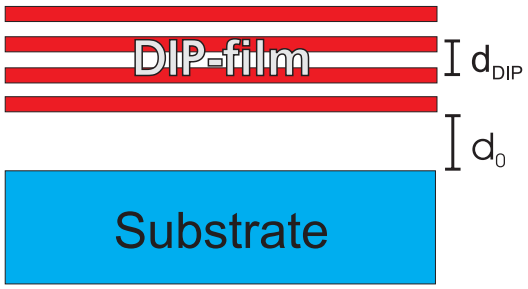

Figure 7.8: Schematic for d_0

The parameterization of the DIP layer and therefore the expressions for $r_B(q_z)$ and $r_C(q_z)$ are discussed in the following.

Parameterization of the electron density of the DIP-film along the z-axis

The parameterization of the DIP electron density, $\rho_{el,\,DIP}(z)$, is facilitated by the fact that each Bragg reflection corresponds to one Fourier-component in the electron density profile of the film. Therefore, $\rho_{el,\,DIP}(z)$ can be written as a series of cosine-terms with amplitudes A_j that represent the intensities of the Bragg reflections and phases ϕ_j (see Eq. 7.4):

$$\rho_{DIP}(z) = \rho_0 + \sum_{j=1}^{M} A_j \cos(j\frac{2\pi}{d_{DIP}}z + \phi_j) \tag{7.4}$$

with M as the number of Bragg peaks, d_{DIP} as the lattice constant of the DIP-film along the z-axis, f_j as the Fourier-amplitude of the j-th Fourier-component and ϕ_j as the phase of the j-th Fourier-component.

In this form (general case) the determination of the phases ϕ_j poses some difficulties. However, DIP is a molecule which shows mirror-plane symmetry and as a consequence, the projection of its electron-density to the z-axis also displays mirror-plane symmetry with respect to $z = d_{DIP}/2$. This has two important implications:

1. the Fourier-phases ϕ_j reduce to $n\pi$ (only then the sum of all cosine-terms is symmetric in the general case!);

2. the electron density is actually described by the cosine-terms of Eq. 7.4 using the Fourier-series composition (the cosine is symmetric in contrast to sine!)

The first constraint reduces the 'phase problem' of Eq. 7.4 to a much easier 'sign problem':

$$\rho_{DIP}(z) = \rho_0 + \sum_{j=0}^{M} v_j A_j \cos(j\frac{2\pi}{d_{DIP}}z) \tag{7.5}$$

with v_j either '+' (equivalent to a phase ϕ_j of $n \cdot 2\pi$) or '-' (equivalent to a phase ϕ_j of $(2n-1) \cdot \pi$).

Now the terms Δ_{Sub} of r_A (Eq. 7.3), $r_B(q_z)$ and $r_C(q_z)$ can be specified:

1. Δ_{Sub}:

$$\Delta_{Sub} = \rho_{Substrate} - \left(\rho_{0,DIP} + \sum_{j=1}^{M} v_j A_j\right) \tag{7.6}$$

   (given that at the interface the individual cosine-terms are either +1 or -1).

2. r_B:

$$r_B(q_z) = f(q_z)\, s(q_z) \tag{7.7}$$

with $f(q_z)$ as the 'reflectivity form factor' of a DIP monolayer, containing the oscillatory electron density, defined in Eq. 7.5:

$$f(q_z) = \int_{-d_{DIP}/2}^{d_{DIP}/2} \frac{\partial \rho(z)}{\partial z}\, e^{iq_z z} dz, \tag{7.8}$$

and $s(q_z)$ as the structure factor of the DIP-molecule stack consisting of N DIP-monolayers:

$$s(q_z) = \sum_{l=0}^{N-1} e^{i(lq_z d_{DIP})} \tag{7.9}$$

where d_{DIP} is the lattice constant of one DIP-monolayer derived from the positions of the Bragg-refections.

Inserting $\rho_{DIP}(z)$ (Eq. 7.5) into the expression for $f(q_z)$ (Eq. 7.8) and evaluating the integral leads to the analytical expression:

$$f(q_z) = \sum_{j=1}^{M} v_j A_j \cdot \frac{i8\pi^2 j^2 \sin\left(q_z \frac{d_{DIP}}{2}\right)}{4\pi^2 j^2 - q_z^2 d_{DIP}^2} \cdot \cos(\pi j) \tag{7.10}$$

3. r_C:

$$r_C(q_z) = \Delta_{surf} e^{iq_z N d_{DIP}} \tag{7.11}$$

with

$$\Delta_{surf} = \left(\rho_{0,DIP} + \sum_{j=1}^{M} v_j A_j\right) - \rho_1 \tag{7.12}$$

At this point the individual contributions $r_A(q_z)$, $r_B(q_z)$ and $r_C(q_z)$ (Eq. 7.3, 7.7, 7.11) are added so that the term $F(q_z)$ of Eq. 4.21 is now written as:

$$\begin{aligned} F(q_z) &= \Delta_{Sub} \cdot e^{-\frac{1}{2}\sigma_{Sub}^2 q_z^2} \\ &+ f(q_z)\, s(q_z) \cdot e^{iq_z d_0} \\ &+ \Delta_{surf} \cdot e^{iq_z(Nd_{DIP}+d_0)} \end{aligned} \tag{7.13}$$

Roughness at the top of the DIP-film

Until now, a flat DIP-film of N DIP-monolayers has been considered that does not show any roughness. To account for the roughness of the DIP-film in the model, a continuous decay of the DIP-coverage ($0 \leq \Theta_i \leq 1$ for the i-th monolayer) along the z-axis is assumed. This decay follows an error-function for $i > N$ with N denoting the number of monolayers with coverage $\Theta = 1$. The error-function is defined as:

$$\mathrm{erf(z)} = \frac{1}{\sqrt{\pi}} \int_0^{\mathrm{z}} \exp(-\mathrm{t}^2)\mathrm{dt} \tag{7.14}$$

For the transition between two 'box-like' media with constant electron densities ρ_1 and ρ_2 and an error function like interfacial density, the derivative $d\rho/dz$ in $F(q_z)$ transforms the error function to a Gaussian, yielding $F(q_z) = \Delta_{1,2} \cdot e^{-\frac{1}{2}\sigma^2 q_z^2}$. In the system under consideration this is true for the term r_A, associated with the transition from the silicon substrate to the DIP-film.

However, for the DIP-film (and presumably for most films of well-ordered, upright standing organic molecules) this ansatz is too simple. The roughness of a DIP layer of some hundred Ångstroms is in the order of $2 \ldots 5$ monolayers of DIP. Due to the (pronounced) oscillatory electron density along one monolayer it is necessary to convolute the error-function profile for the

DIP-coverage with the *oscillatory form factor* $f(q_z)$ of the DIP to obtain the *correct electron density profile* for the transition between the DIP-film and the medium above it (for illustration, see the *oscillatory* decay of the DIP electron density towards vacuum at the right hand side of Fig. 7.10).

To account for this convolution in the model, the contribution r_C (Eq. 7.11) is replaced by

$$r'_C = \left(\int_0^{5\cdot\sigma_{DIP}} \frac{\partial \rho_C(z)}{\partial z} \, e^{iq_z z} dz \right) e^{iq_z N d_{DIP}} \tag{7.15}$$

with

$$\rho_C(z) = \mathrm{erf}\left(\frac{\mathrm{z} - \mathrm{z}_\mu}{\sqrt{2}\sigma^2_{\mathrm{DIP}}} \right) \rho_{\mathrm{DIP}}(\mathrm{z}), \tag{7.16}$$

where $z_\mu = 2.5 \times \sigma_{DIP}$ and the integral in Eq. (7.15) runs from 0 to $5 \times \sigma_{DIP}$. These integrating boundary-conditions have been chosen such that 98% of the area of the probability density, represented by a Gaussian associated with the error-function, lies in the above mentioned range ($z_\mu \pm 2.5 \cdot \sigma$).

At this point, the film thickness D_{DIP} of the DIP-film is given in this model simply by

$$D_{DIP} = N d_{DIP} + 2.5 \cdot \sigma_{DIP} \tag{7.17}$$

and the effective (mean) number of DIP-layers of the DIP-film, $\overline{N}$, associated with D_{DIP} is calculated as

$$\overline{N} = N + \frac{2.5 \cdot \sigma_{DIP}}{d_{DIP}} \tag{7.18}$$

Dissipative part of the index of refraction, β

β has two implications for the intensity, (a) it leads to absorption and (b) it contributes to the index of refraction.

In the model presented here, absorption of x-rays in the organic film has not been taken into account. Even for small incident angles it does not play a significant (noticeable) role in the present case due to the small value of $\beta_{DIP} \approx 1 \times 10^{-8}$ and to the small film-thickness of (100 Å $\lesssim D_{DIP} \lesssim$ 1100 Å) which is examined in this study. Absorption in the substrate does not contribute to the scattering intensity.

On the other hand, the contribution of β to the index of refraction is taken into account (n and $k_{t,z}$ are complex numbers) for the calculation of the Fresnel-reflectivity, R_F, of the substrate which is multiplied to $|F(q_z)|^2$ in Eq. 4.21. For the organic film, the ratio between β and δ is factor 10 smaller than for silicon, therefore β_{DIP} is not considered in the model.

The integrand $F(q_z)$

Summing up the results of the previous subsection we arrive at the final form of the integrand of Eq. 4.21:

$$\begin{aligned} F(q_z) &= r_A + r_B + r'_C \\ &= \Delta_{Sub} \cdot e^{-\frac{1}{2}\sigma^2_{Sub}\, q_z^2} \\ &+ f(q_z)\, s(q_z) \cdot e^{iq_z d_0} \\ &+ \left(\int_0^{5\cdot\sigma_{DIP}} \frac{\partial \rho_C(z)}{\partial z}\, e^{iq_z z} dz \right) \cdot e^{iq_z(Nd_{DIP}+d_0)} \end{aligned} \tag{7.19}$$

7.2.3 Results of the model

The specular rod data of five samples with different thicknesses were fitted by the proposed model. For each data-set four or more DIP Bragg reflections were measured. To fit the data we fixed the parameters ρ^0_{DIP} to the individual value we found by the Parratt-algorithm and ρ_{Si}. The values σ_{DIP} and σ_{Si} of

the Parratt-algorithm were used as starting parameters in the Master formula fit. To obtain a starting value for the number of monolayers, N, the thickness of the DIP-film, D_{DIP}, was employed (which has previously been obtained by the Parratt-algorithm).

parameter	'o126'	'o206'	'o396'	'o670'	'o1100'
N	5	10	20	32	56
d_{DIP} (Å)	16.65 ± 0.05	16.62 ± 0.03	16.587 ± 0.03	16.559 ± 0.02	16.563 ± 0.02
σ_{Si} (Å) (±0.2 Å)	2.1	1.9	1.6	1.7	1.8
σ_{DIP} (Å)	13 ± 1	13 ± 1	24 ± 2	53 ± 3	62 ± 3
d_0 (Å)	0.8 ± 0.2	0.4 ± 0.2	0.7 ± 0.2	0.4 ± 0.2	0.2 ± 0.2
$\overline{A_1}$ (±0.005)	+0.21	+0.285	+0.305	+0.298	+0.31
$\overline{A_2}$ (±0.002)	+0.032	+0.045	+0.069	+0.061	+0.0395
$\overline{A_3}$ (±0.0002)	+0.0045	+0.0063	-0.0109	-0.009	-0.0021
$\overline{A_4}$ (±0.0002)	+0.009	+0.0155	+0.0305	+0.0212	+0.0051
$\overline{A_5}$ (±0.0002)	–	(+)0.0071	(-)0.0146	(-)0.0104	–
$\overline{A_6}$ (±0.0002)	–	(+)0.0043	(+)0.0063	(+)0.0063	–
$\overline{A_7}$ (±0.0001)	–	(+)0.0041	(+)0.0055	(+)0.0056	–
$\overline{A_8}$ (±0.0001)	–	–	–	(+)0.0016	–
$\overline{A_9}$ (±0.0001)	–	–	–	(+)0.0017	–
$\overline{N}$	6.95 ± 0.15	11.95 ± 0.15	23.62 ± 0.3	40.00 ± 45	65.36 ± 0.45
D_{DIP} (Å)	115.8 ± 2.5	198.7 ± 2.5	391.7 ± 5	662.4 ± 7.5	1082.5 ± 7.5
ρ^0_{DIP} (el/Å^3)	0.344	0.367	0.390	0.402	0.390
ρ^{max}_{DIP} (el/Å^3)	0.431	0.502	0.542	0.553	0.527
ρ^{min}_{DIP} (el/Å^3)	0.284	0.280	0.283	0.300	0.287
$\rho^{max}_{DIP}/\rho^{min}_{DIP}$	1.52	1.79	1.91	1.85	1.84

Table 7.2: Parameters used in the fits with the Master formula. The parameters $\overline{A_j}$ are 'effective parameters' and defined as $\overline{A_j} = v_j A_j / \rho^0_{DIP}$.

The position of the Bragg reflections fixed the value of d_{DIP} with high accuracy and the intensity of these reflections yielded the values A_j. The decay of the intensity is determined primarily by the roughness of the substrate σ_{Si}. The parameter pair D_{DIP} (related to N via Eq. 7.17) and σ_{DIP} determines the oscillation period (D_{DIP}) of the Kiessig-fringes and Laue-oscillations as well as the damping (σ_{DIP}) of these oscillations.

Therefore, the only 'free' fitting parameters were the distance d_0, and the

signs v_j which could be determined up to the 4th or 5th Bragg reflection due to the interference effect with the wave reflected from the substrate. For higher order Bragg reflections (with a very small contribution to the oscillation amplitude of the electron density) v_j was set to '+' ($v_{j>5} = +$).

The results of the fits for the five samples are listed in Table 7.2. The parameters $\overline{A_j}$ are 'effective parameters' and they are defined as $\overline{A_j} = v_j A_j / \rho^0_{DIP}$. Fig. 7.9 and Fig. 7.10 show the specular-rod data together with the fit for sample 'o396' and the electron-density profile, $\rho_{el}(z)$ which was used for the fit, respectively. In Fig. 7.11 the data and fits for the other 4 samples are displayed.

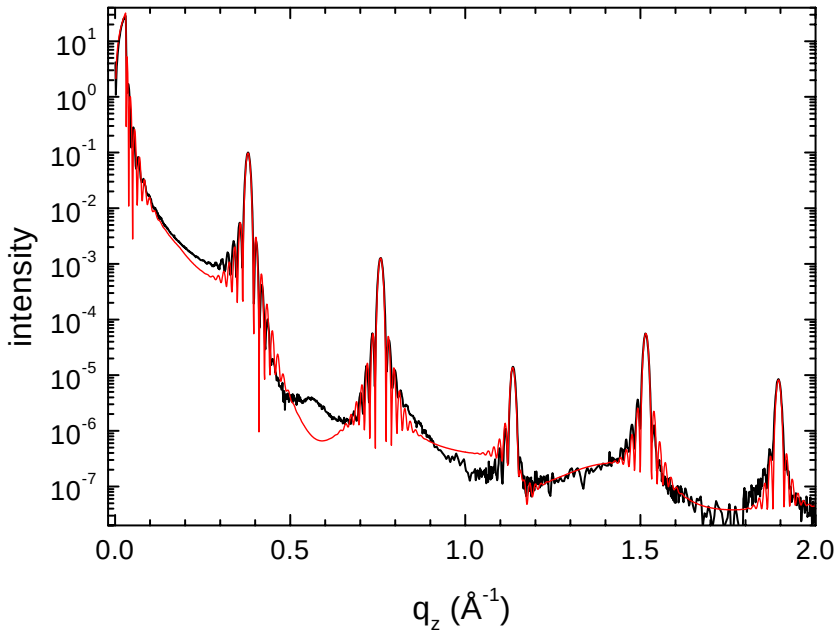

Figure 7.9: Fit (red) to the specular rod of 'o396' (black) using the Master formula (the first 5 Bragg reflections are seen).

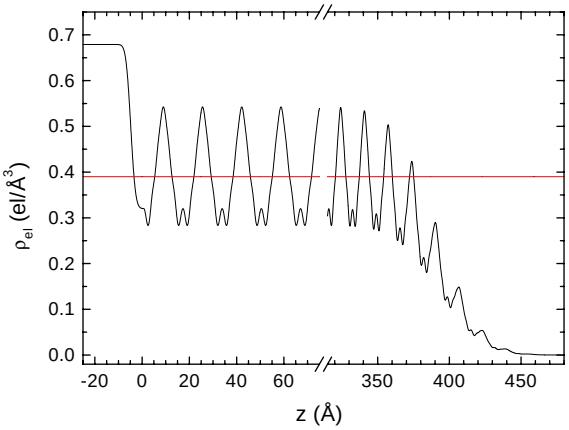

Figure 7.10: Electron density, $\rho_{el}(z)$ used for the fit in Fig. 7.9.

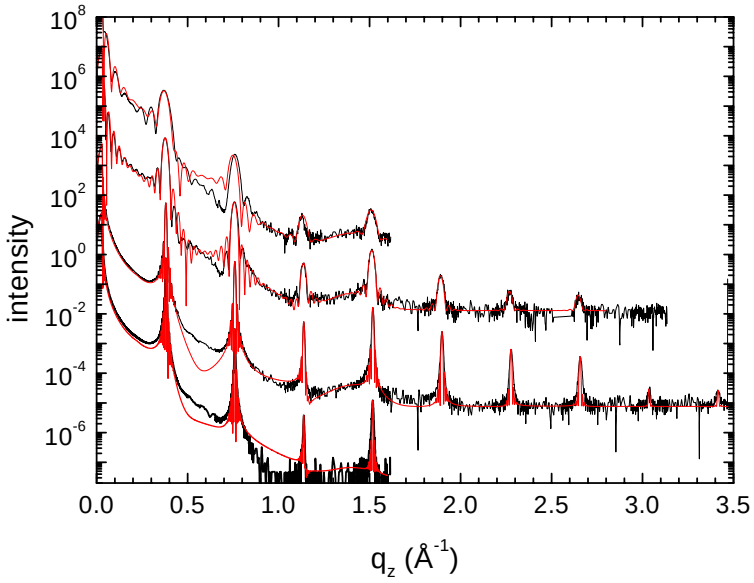

Figure 7.11: Fit (red) to the data (black) of 'o126', 'o206'; 'o670', and 'o1100' using the Master formula (from top to bottom).

7.2.4 Discussion

The analysis of the data for samples with a film thickness between ≈70 Å and ≈1100 Å allowed for the determination of several parameters as a function of thickness. The behavior of the parameters d_{DIP}, $\rho_{DIP}(z)$, and d_0 will be discussed below. The behavior of σ_{DIP} as a function of film thickness provides information on the growth process. This will be discussed in Chapter 8.

Lattice constant for DIP, d_{DIP}, as function of film thickness, D_{DIP}

As was pointed out previously, the large number of out-of plane Bragg reflections observed in x-ray measurements on the specular rod allows for the determination of the DIP lattice constant with a high degree of accuracy. The values of d_{DIP} are listed in Table 7.2 and are displayed in Fig. 7.12. One observes a significant decrease of d_{DIP} with increasing film thickness up to $D_{DIP} \approx 670$ Å. Here, the value of d_{DIP} remains constant at 16.56 ± 0.02 Å. Over the observed range of film thickness the lattice constant changed by $\Delta d_{DIP} = 0.09$ Å; this corresponds to a decrease of d_{DIP} of 0.54% in the thickest films compared to the thinnest film.

Electron density, $\rho_{DIP}(z)$, as a function of film thickness, D_{DIP}

In the model under consideration, the electron density of DIP is split into two parts. First, the (constant) 'mean' electron density ρ^0_{DIP} (determined by the analysis of the x-ray reflectivity with the Parratt formalism, see Table 7.1). Second, the oscillations around ρ^0_{DIP} associated with the Fourier decomposition of the oscillatory electron density (Eq. 7.5). The oscillatory part is defined by the parameters v_j and A_j listed in Table 7.2 for five samples. Fig. 7.13 displays ρ^0_{DIP} (all samples, ■) and the extreme values in the oscillatory electron density, ρ^{max}_{DIP} (▲) and ρ^{min}_{DIP} (▼) (for five samples), as a function of film thickness.

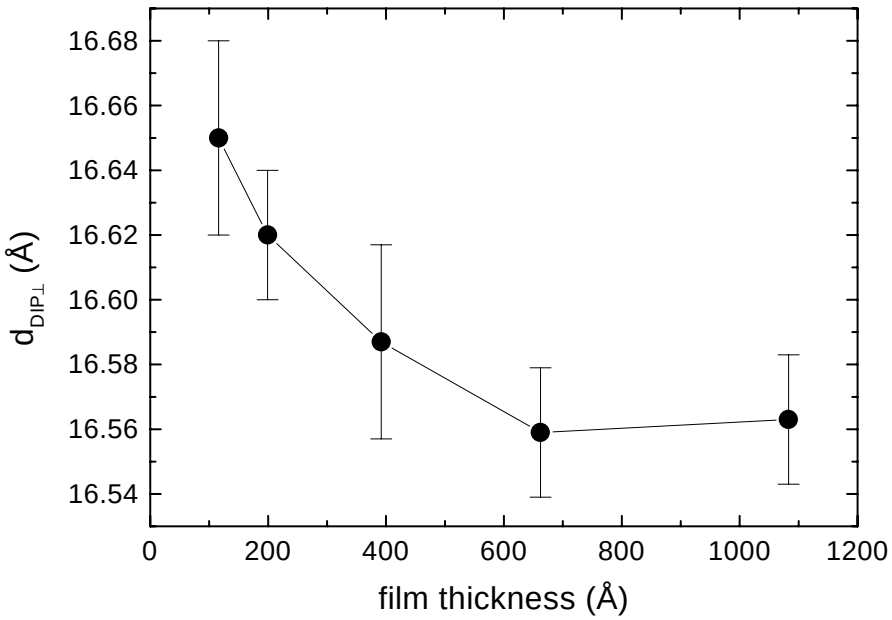

Figure 7.12: Lattice constant of the DIP film perpendicular to the substrate versus film thickness.

It can be clearly seen that ρ^0_{DIP} increases with increasing film thickness up to $\approx$ 400 Å where the value saturates at $\rho^0_{DIP} = 0.39$ el/Å^3. The same behavior is observed for ρ^{max}_{DIP}, which saturates at $\rho^{max}_{DIP} = 0.53 \pm 0.015$ el/Å^3. On the other hand, the minimum in the electron density remains essentially constant for all films, $\rho^{min}_{DIP} = 0.285 \pm 0.015$ el/Å. Note, that the values of ρ^{max}_{DIP} and ρ^{min}_{DIP} are representative also for 'o126' and 'o1100' although only four Bragg reflections were measured. The error can be estimated by comparison with the components $A_{5\ldots9}$ of the other samples as $\rho^0_{DIP} \cdot \sum_{j=5}^{9} \overline{A_j}$ and it is at maximum 0.015 el/Å^3.

The increase of both ρ^0_{DIP} and ρ^{max}_{DIP} points to a change in the structural

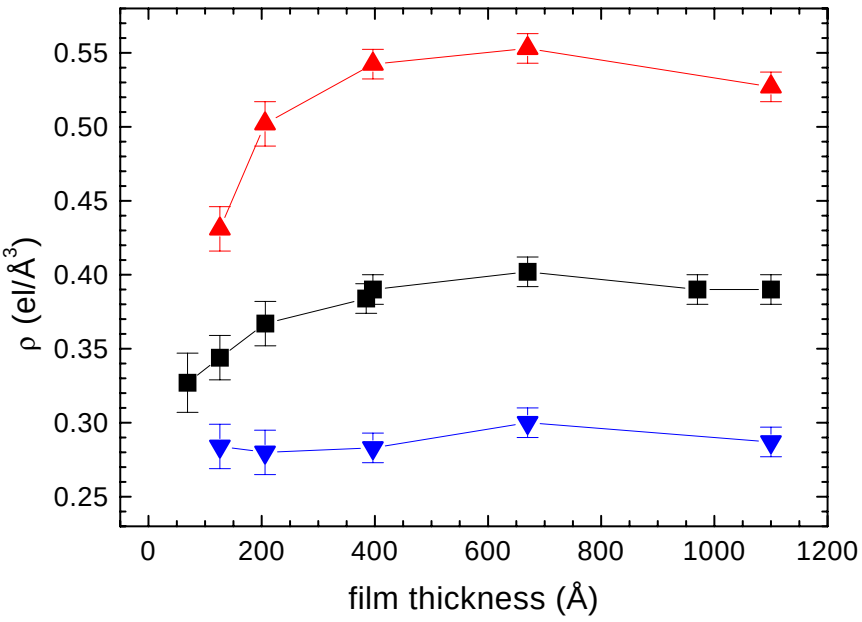

Figure 7.13: ρ^0_{DIP} (■, determined by fitting the reflectivity with the Parratt-formalism, see Table 7.1 and Fig. 7.6), ρ^{max}_{DIP} (▲), and ρ^{min}_{DIP} (▼) versus the film thickness.

order of the films at larger thickness ($\approx$ 400 Å). This change cannot be explained simply by the smaller lattice constant d_{DIP} because the change in ρ^0_{DIP} from the sample 'o126' to the thickest sample 'o1100' is $16.9 \pm 5.9\%$. It exceeds the relative change in the lattice constant for the respective samples ($\Delta d_{DIP} = -0.54\%$) by more than one order of magnitude. The increase in ρ^0_{DIP} is even $22.9 \pm 8.1\%$ if one compares 'o69' with 'o1100'.

Thus, $\rho^0_{DIP} \times d_{DIP}$ is not constant over the inspected range of thickness, implying an increase in the mean area electron-density (up to $D_{DIP} = 400$ Å) within the layers.

This may be explained by a change in the in-plane structure of the films associated with a closer packing, i.e., a change in the unit-cell of the film. Note also the strong increase in ρ_{DIP}^{max} ($25.6 \pm 9.9\%$) (comparing 'o396', 'o670', and 'o1100' with 'o126'). Moreover, the Fourier sign for the 3rd Bragg reflection, v_3 changes from '+' to '-' for films with a thickness[4] $D_{DIP} \geq 396$ Å. Fig. 7.14 shows the electron density of approximately two monolayers in the DIP film for the various samples. The 'small' peak in the minimum area of 'o396' and 'o670' is attributed to the sign change of v_3 and v_5. It is clearly evident that an increase of film thickness results in an increase of the oscillation amplitude. Note, however, that only the density-maximum, ρ_{DIP}^{max}, is increasing whereas the minimum, ρ_{DIP}^{min}, remains essentially constant.

To investigate the nature of a structural change as suggested above, information about changes in the in-plane structure as a function of film thickness are necessary. Information about the in-plane structure of DIP thin films will be presented in Sec. 7.4. However, these data were not recorded as a function of film thickness. Thus, while the occurrence of a structural change is clear from the data, its exact nature is not known. Nevertheless, the change appear to be continuous over some range of thickness, as opposed to an abrupt transition.

[4]A sign change in v_5 from '+' to '-' for films with a thickness $D_{DIP} \geq 396$ Å resulted in slightly better fits but this is not significant due to a lack of interference patterns at the 5th Bragg reflection.

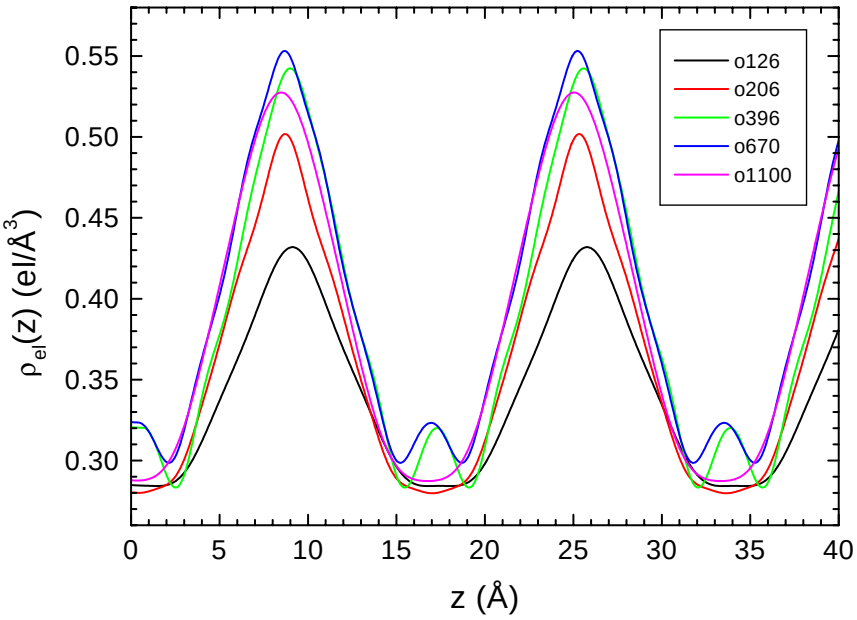

Figure 7.14: close up to the electron density $\rho_{el}(z)$ of approximately 2 monolayers of DIP for the 5 different samples.

7.3 Temperature Dependent Measurements

The thermal stability of organic layers, their desorption mechanism as well as their thermal expansion coefficient are of great importance not only from a fundamental point of view but also for technical applications. Therefore, temperature dependent x-ray measurements have been carried out at beamline W1 at HASYLAB.

7.3.1 Sample preparation and characterization

A DIP film with $D_{DIP} = 890$ Å was prepared on a thermally oxidized (4000 Å) silicon wafer (Si(100)), employing the usual deposition conditions (rate ≈ 12 Å/min, $T_{Sub} = 145°\text{C} \pm 5°\text{C}$; see Table C.1)[5]. This sample, 'o890', was then characterized by means of x-ray reflectivity (Fig. 7.15 and Table 7.3) at room temperature and afterwards split into two pieces (size $\approx 5 \times 10$ mm^2), hereafter referred to as 'o890a' and 'o890b'. Samples 'o890a' and 'o890b' were exposed to different thermal annealing procedures. Sample 'o890a' was exposed and measured extensively up to a temperature of $T_{max,a} = 205°\text{C}$. At this temperature the desorption rate is large so that 'o890a' neither showed pronounced specular Bragg-reflections after the annealing procedure nor did it exhibit Kiessig-fringes for small values of q_z. This observation provides evidence for a thermally destructed organic film. In contrast, 'o890b' was exposed and measured only for approximately one minute at a maximum temperature of $T_{max,b} = 200°\text{C}$. After the annealing-procedure, 'o890b' still exhibited a well-defined crystallinity as probed by the specular DIP Bragg-reflections. In addition, the sample still showed well-defined Kiessig-fringes in x-ray-reflectivity measurements (see Fig. 7.15 and Table 7.3). The x-ray reflectivity data for the samples before and after the annealing procedure

[5]Note that temperature dependent measurements at three similar samples exhibited the same results within the experimental error.

were fitted according to Parratt and the fit parameters[6] are listed in Table 7.3.

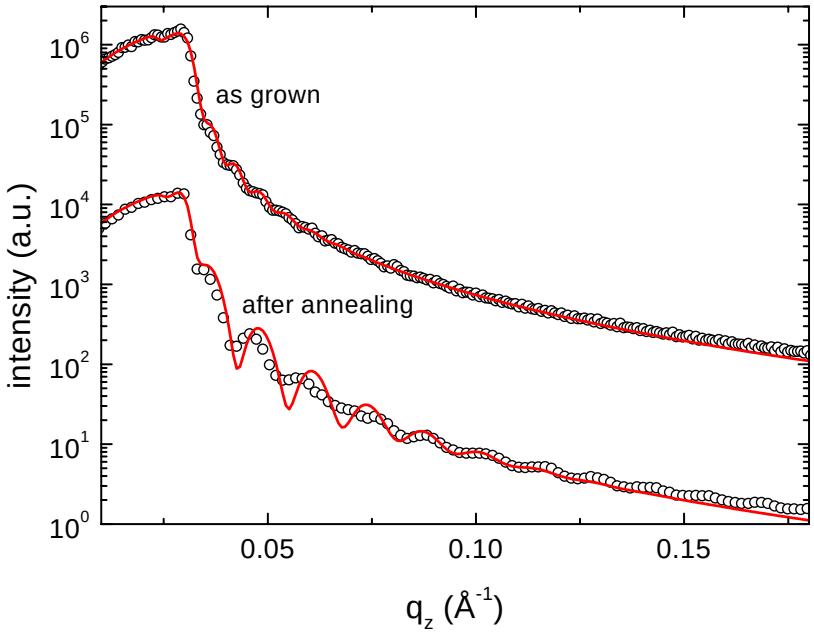

Figure 7.15: 'o890' before annealing and 'o890b' after annealing. The solid lines are fits to the data. The curves are offset with respect to each other for sake of clarity.

At each temperature step at least one specular DIP Bragg reflection was

[6]The fit for sample 'o890b' is not excellent because for $q_z \lesssim 0.07$ Å^{-1} the periodicity of the Kiessig-fringes is smaller than for larger values of q_z. Employing the Parratt-algorithm, it was tried to match the region $q_z > 0.07$ Å^{-1}; the mismatch for smaller values of q_z is accounted for by the large error-bar of ± 15 Å for D_{DIP}. The error covers also the larger film-thickness which corresponds to the periodicity in the region $q_z \lesssim 0.07$ Å^{-1}. Since the precision of D_{DIP} is sufficient for the discussion the development of a more sophisticated model has not been considered at this point.

parameter	'o890' as grown	'o890b' annealed
D_{DIP} (Å)	890 ± 5	445 ± 15
σ_{DIP} (Å)	47 ± 4	25 ± 5
ρ^0_{DIP} (el/Å^3)	0.394 ± 0.01	0.39 ± 0.01
β_{DIP} (el/Å^3)	1.0×10^{-8}	
σ_{Si} (Å)	1.2 ± 0.3	
ρ_{Si} (el/Å^3)	0.689	
β_{Si} (el/Å^3)	2×10^{-7}	

Table 7.3: X-ray reflectivity: fit parameters for sample 'o890' as grown and after annealing

recorded with its Laue oscillations before the next temperature was set. The Bragg reflections were fitted by the Laue function (square of Eq. 4.30)

$$I = y_0 + I_0 \left(\frac{\sin(\frac{N q_z d_{DIP}}{2})}{\sin(\frac{q_z d_{DIP}}{2})} \right)^2 \quad , \tag{7.20}$$

where y_0 is a constant background, I_0 is the intensity, d_{DIP} is the lattice constant in the DIP-film, and N is the number of (coherently scattering) monolayers in the film. In this formula, d_{DIP} is adjusted by fitting the position of the Bragg reflection while N is sensitive to the periodicity of the Laue-oscillations.

The thermal stability of DIP-films, the desorption mechanism and the desorption rate at a given temperature, as well as the determination of the thermal expansion coefficient for expansion perpendicular to the surface will be addressed in the following subsections.

7.3.2 Thermal stability and desorption mechanism

Fig. 7.16 displays the thermal stability of the DIP film during the annealing procedure of sample 'o890b'. In Fig. 7.16 (a) it is clearly seen that the normalized intensity (filled squares) of the DIP(001) Bragg-reflection remains (almost) constant upon annealing up to $T \approx 160$°C (dotted line)[7]. At the same time, the coherent thickness of the film, D_{coh}, does not change (Fig. 7.16 (b)).

For higher temperatures ($T \gtrsim 160$°C) the intensity of the Bragg reflection decays as does the coherent thickness. The ratio between Bragg reflection intensity and coherent thickness remains almost constant during the annealing procedure. For comparison, both parameters are displayed in Fig. 7.16 (a) simultaneously: the intensity (filled squares) decreases by 60%, the coherent thickness (gray open circles) by 50%. This observation points to a laterally homogeneous desorption process, e.g., a layer-by-layer desorption, which does not affect the crystallinity of the film during desorption. The x-ray reflectivity data at sample 'o890b' (Fig. 7.15, Table 7.3) after the annealing procedure demonstrates that the film thickness, D_{DIP}, still equals the coherent thickness, D_{coh}, as was found for all unannealed DIP-films investigated in the present study. This observation excludes a dewetting or island-formation of the film during desorption and supports the scenario of laterally homogeneous desorption.

Furthermore, the data allow for an estimate of the desorption rate at a given temperature. This is done by scanning a Bragg reflection repeatedly at the same temperature and by subsequently evaluating the number of coherently scattering monolayers N as a function of time. Given the experimental

[7]Note that the rocking width of the reflection remains constant during the annealing procedure. This rules out the possibility of a decrease in intensity due to an onset of a disordering processes. The slight increase in the intensity up to $T = 150$°C can be attributed to improvement of the order as a consequence of elevated temperature.

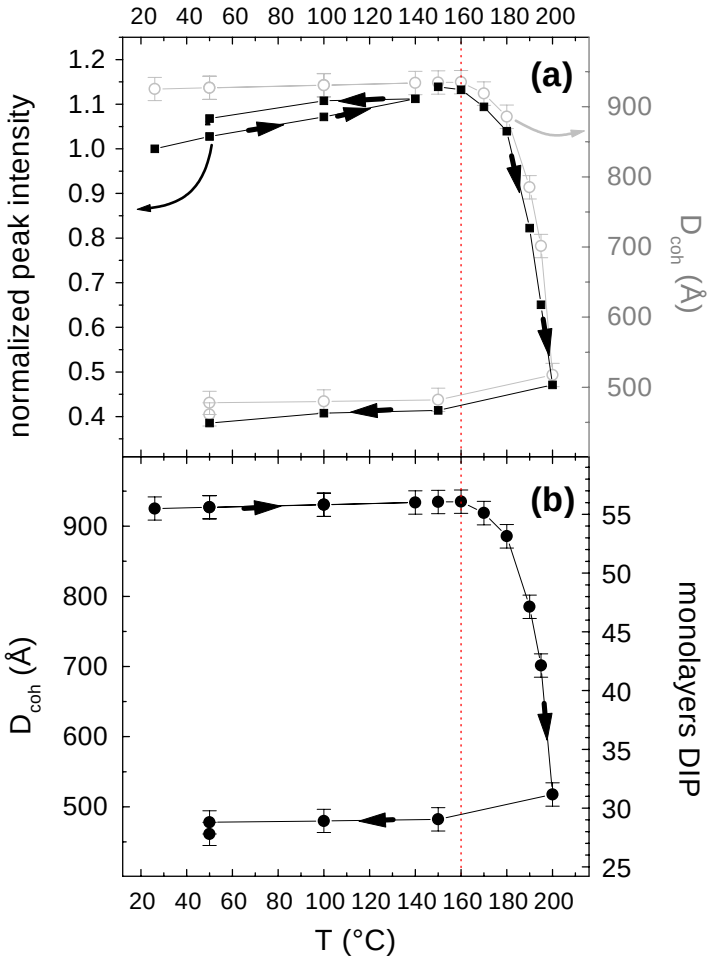

Figure 7.16: 'o890b': (a) intensity of the DIP(001)-Bragg reflection as a function of temperature (■); the coherent thickness of the DIP layer, D_{coh}, is displayed simultaneously (gray ◯, right axis) to demonstrate that it starts to decay at the same temperature as the Bragg-intensity. (b) D_{coh} in Å (•, left axis) and in monolayers (right axis) as a function of temperature.

conditions and assuming layer-by-layer desorption, a desorption rate of approximately one monolayer of DIP per minute (1 ML/min) is obtained[8] at $T = 195°\mathrm{C} \pm 10°\mathrm{C}$.

7.3.3 Thermal expansion

For the temperature-range of thermal stability, the thermal expansion coefficient for the DIP-film in the direction approximately parallel to the molecular plane (i.e., perpendicular to the substrate), $\alpha_{\parallel}$, has been determined.

For samples 'o890a' and 'o890b', Fig. 7.17 displays the relative change of $d_{DIP}(T)$ in % compared to $d_{DIP}(300\,\mathrm{K})$ in the temperature range of thermal stability of the DIP-film ($T \leq 160°\mathrm{C}$) and a linear fit to the data. The slope of the fit provides the thermal expansion coefficient $\alpha_{\parallel}$. The average of both samples gives $\alpha_{\parallel} = (75.8 \pm 4.5) \times 10^{-6}$ 1/K (Table 7.4). This is large compared to typical expansion coefficients of metals but it shows the same order of magnitude as $\alpha_{\parallel}$ in similar organic materials (see Table 7.4).

Crystals or thin films of planar organic molecules usually exhibit a large anisotropy of their thermal expansion in different crystalline directions. Londsdale states in Ref. [71]: "In cases where the molecules are plane and where (as is usually the case) one direction in the crystal (or film) is most nearly normal to the molecular plane, the thermal expansion is greatest along that direction ($\alpha_{\perp}$)". Empirically, a factor of 2 ... 4 is found between $\alpha_{\perp}$ and $\alpha_{\parallel}$ for many planar molecules with predominant intermolecular van-der-Waals bonds (but also for organic salts [72]).

Van Smaalen *et al.* [72] employed a simple model to explain these observations. In their study, they assumed stacks of planar molecules with the stacking direction normal to the molecular plane, hereafter referred to as 'z-

[8]Note, that this value has to be considered as a rough estimate with an accuracy of a factor of 2 only since the focus of the experiment was not the determination of desorption rates.

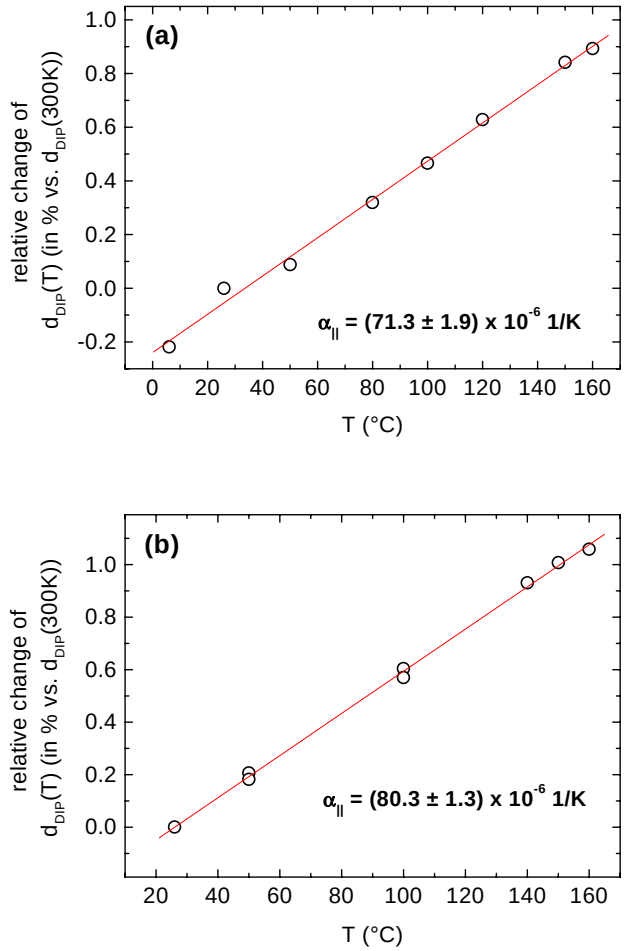

Figure 7.17: Thermal expansion of DIP for $T \leq 160°\mathrm{C}$. Relative change of $d_{DIP}(T)$ in % compared to $d_{DIP}(300\,\mathrm{K})$ as a function of temperature for (a) sample 'o890a' in the temperature interval $6°\mathrm{C} \ldots 160°\mathrm{C}$, and for (b) sample 'o890b' in the temperature interval $26°\mathrm{C} \ldots 160°\mathrm{C}$. The slope of a linear fit to the data gives the thermal expansion coefficient $\alpha_{\|}$.

axis'. The anisotropy in the thermal expansion is estimated by the following consideration. Thermal expansion normal to the molecular planes (i.e., in

stacking direction) will occur due to three processes ('degrees of freedom'):

1. thermal vibrations of the molecules along the z-axis,
2. thermally induced libration (i.e., rotational oscillations) of the whole molecule around the x-axis,
3. thermally induced libration of the whole molecule around the y-axis.

On the other hand, for thermal expansion parallel to the molecular plane, the two librational degrees of freedom do not result in markedly expansion or contraction[9]. A ratio of 3:1:1 for the thermal expansion coefficients is the consequence of this simple model. Employing a more realistic model, van Smalen *et al.* obtained $\alpha_\perp : \alpha_\parallel = 2.1 : 1$.

The thermal expansion coefficient parallel to the surface for the essentially upright standing DIP-moelcules in thin films, $\alpha_\perp$, is not yet determined. However, following the empirically and numerically obtained results presented above, it is expected, that $\alpha_\perp$ is a factor of $2 \ldots 4$ larger than $\alpha_\parallel$. This assumption is supported by the determination of the thermal expansion coefficients $\alpha_\parallel$ and $\alpha_\perp$ in thin films of PTCDA (Table 7.4), a planar perylene-derivate as DIP. The PTCDA-molecules are lying flat on the surface, i.e., with their molecular plane parallel to the surface. Their thermal expansion normal to the molecular plane, $\alpha_\perp$ is reported to be a factor of 2 larger than $\alpha_\parallel$. For comparison, the values of some additional polyaromatic organic materials are listed in Table 7.4 which provide further evidence for the assumption that $\alpha_{\perp,DIP}$ will be larger by a factor of $2 \ldots 4$ compared to $\alpha_{\parallel,DIP}$.

[9]Let the (small) angle of libration, i.e., the 'oscillation amplitude', be ϕ. Then the change in length is proportional to $\cos\phi$ for expansion normal to the molecular plane and it is proportional to $\sin\phi$ for expansion or contraction parallel to the molecular plane. For small ϕ this results in negligible expansion / contraction parallel to the molecular plane.

material	$\alpha_\perp$ (10^{-6} 1/K)	$\alpha_\parallel$ (10^{-6} 1/K)
DIP-films	—	75.8 ± 4.5
PTCDA[a] ($C_{24}H_8O_6$)	105 ± 6	≈ 50
Benzene[b] (C_6H_6)	221	106 / 119
Naphtalene[b] ($C_{10}H_8$)	225	40 / 115
Dibenzyl[c] ($C_{14}H_{14}$) $C_6H_5CH_2CH_2CH_5$	223	87 / 147
Trans-Stilbene[c] ($C_{14}H_{12}$) $C_6H_5CH = CHCH_5$	117	61 / 68
Al ($\pm 3\%$)	23.1 ... 25.8	
Au ($\pm 3\%$)	14.2 ... 15.2	
Cu ($\pm 3\%$)	16.5 ... 18.0	
Cr ($\pm 3\%$)	4.9 ... 8.3	

Table 7.4: Thermal expansion coefficients of DIP (samples 'o890a' and 'o890b'), organic materials, and some metals [73] which are often used in device fabrication. $\alpha_\perp$ and $\alpha_\parallel$ denote the thermal expansion coefficients in the stacking direction (almost) perpendicular to the molecular plane and (almost) parallel to the molecular plane, respectively. The thermal expansion in the plane of the molecules ('parallel') could depend on the main axes, i.e., two different values could be observed. The range of α for the metals corresponds to $\alpha(20°\mathrm{C})$ and $\alpha(177°\mathrm{C})$, respectively.

[a] Thin films of 3,4,9,10 perylenetetracarboxylic dianhydride (PTCDA). The planar PTCDA molecules grow with their plane parallel to the substrate surface. Data are taken from [74].

[b] Data for molecular crystals, taken from [71].

[c] Data for molecular crystals, taken from [75]. Note that the values are attributed to $\alpha_\perp$ and $\alpha_\parallel$ under the assumption that the molecules are planar and 'the thermal expansion is greatest at the direction normal to the molecular plane' ([71], see also [72])

Large differences in the thermal expansion between DIP and metals are supposed to have a negative impact on the lifetime of metal-organic hetero-systems employed in organic-electronics. In particular, frequently changing operating temperatures then will produce a high level of thermally induced stress and/or strain at the DIP-metal interface. The latter may modify the interfacial morphology resulting in unforeseen changes of the device performance.

7.3.4 Structural changes for $T > 160°\mathrm{C}$

Fig. 7.18 (a) and (b) show that the DIP-film undergoes an irreversible structural change for annealing temperatures beyond the desorption temperature ($T > 160°\mathrm{C}$). A second change in the structure occurs for $T \geq 200°\mathrm{C}$ (see Fig. 7.18 (a)). The different structural phases are denoted with different symbols and colors.

1. **Reversible Changes of Structure 1:** Open (black) circles are related to the 'as grown phase' (phase 1) which was used to determine the thermal expansion coefficient in the previous subsection. 'Structure 1' is reversible stable for annealing below $T \lesssim 150°\mathrm{C}$. This is seen in Fig. 7.18 (b). Following annealing up to $T = 140°\mathrm{C}$ the temperature is decreased. At a given temperature after completion of this annealing process, $d_{DIP}(T)$ is the same within the experimental error as it has been during the annealing process.

2. **Structure 2: Irreversible Changes:** Open (red) diamonds denote 'structure 2' which forms at temperatures $T \gtrsim 160°\mathrm{C}$ where also significant desorption sets in. In this phase of the annealing process, first, the thermal expansion of DIP is much smaller, then d_{DIP} saturates and eventually it even decreases with increasing temperature. This observation is clear evidence for a structural change in the film.

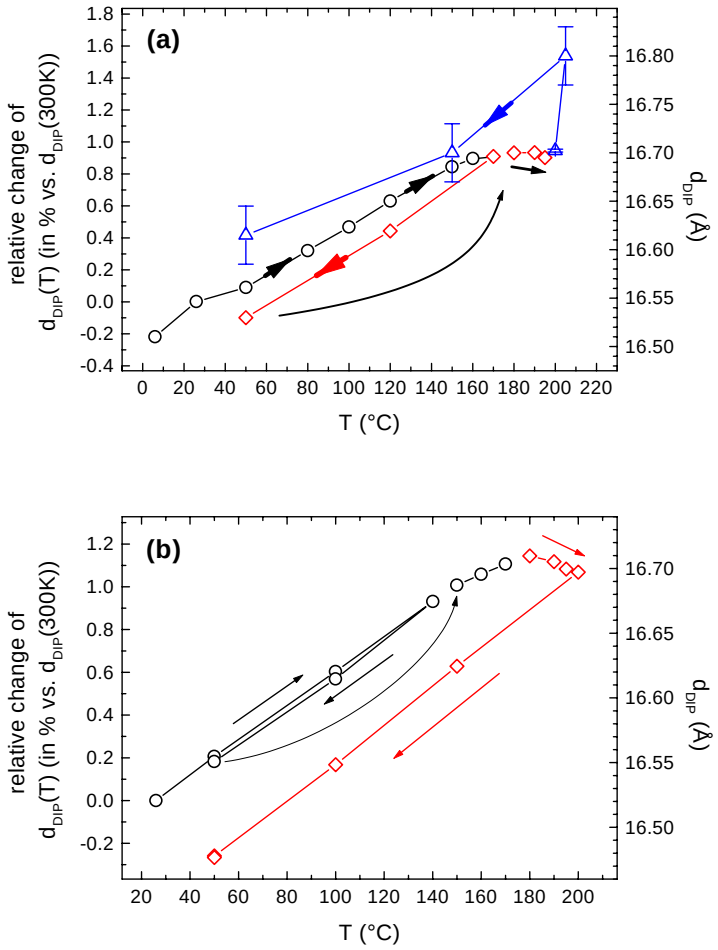

Figure 7.18: Relative change of $d_{DIP}(T)$ in ▽ compared to $d_{DIP}(300\,\mathrm{K})$ (left axis) and $d_{DIP}(T)$ (right axis) as a function of temperature for the annealing procedure of (a) sample 'o890a', and for (b) sample 'o890b'. The error is smaller than the symbol size if not explicitly displayed. Arrows indicate the route of the annealing procedure. The three structures are denoted as follows. Structure 1 = black ◯. Structure 2 = red ♢. Structure 3 (only in (a)) = blue △.

If the temperature is decreased after having reached 'structure 2', d_{DIP} decreases with almost the same expansion coefficient as in 'structure 1' (it is slightly higher: $\alpha = (80 \pm 4.5) \times 10^{-6}$ 1/K). However the contraction starts linearly from the lattice spacing, which was achieved at the highest temperature in the annealing process, $d_{DIP}(T_{max})$ resulting in the hysteresis-like form for the combination of 'structure 1' and 'structure 2' (see Fig. 7.18 (a) and (b)). It implies that 'structure 1' is metastable which is consistent with the fact that in bulk DIP the lattice parameters are different (Sec. 3.2) from the film value of $d_{DIP}(300\,K) \approx 16.55$ Å. The change in structure may therefore be attributed to a thermally activated process which forces the DIP-molecules to reorganize (more closely) to the bulk structure.

3. **Structure 3: Irreversible Changes and Enhanced Desorption:** Open (blue) triangles in Fig. 7.18 (a) for $T \geq 200$°C are related to 'structure 3'. At $T \approx 195$°C the decrease of d_{DIP} with increasing temperature reaches a final value. For still higher temperatures, d_{DIP} increases enormously in a small temperature interval which gives a thermal expansion of $\alpha_{\|} \approx 1170 \times 10^{-6}$ 1/K. This large value is evidence for a second structural change rather than to real thermal expansion. At the same time the desorption rate boosts up.

   For this structural phase, again, decreasing the temperature results in a decreasing d_{DIP} with $\alpha_{\|}$ being of the same order as observed for 'structure 1' and 'structure 2'. Thus, a second hysteresis-like effect is visible with d_{DIP} at a given temperature being larger than d_{DIP} determined during the first annealing within 'phase 1'. This observation is clear evidence for an irreversible process which has taken place. The large thermal expansion coefficient in 'phase 3' ($\alpha_{\|} \approx 1170 \times 10^{-6}$ 1/K) may be related to a breakdown of the weak intermolecular van-der-Waals

bonds which are assumed to be the key interactions that drive the high self-organized order of the DIP-films. Note that the data point at $T = 200°C$ in Fig. 7.18 (b) may already be attributed to 'structure 3'. However, in the annealing procedure of 'o890b' the exposure time of the sample at high temperatures was limited to a short time-interval so that it is not clear whether a change to 'structure 3' actually is observed.

The reported observations of three structures are in agreement with thermal desorption spectroscopy (TDS) data taken by Münch [1]. In addition, the extremely large thermal expansion coefficient of DIP in 'structure 3' may be seen similar to the observations of extremely large expansion coefficients in crystals of alkyl-chains close to their melting points [71]. Both observations are discussed below.

As in the thermal expansion data for DIP-films the TDS-spectrum displays the onset of detectable desorption at $T \approx 155°C$ with a slowly increasing desorption rate for increasing temperatures. However, at $T \approx 200°C$ there is a kink in the TDS-spectrum with a much larger slope for the desorption rate as a function of temperature. This kink in the TDS-spectrum corresponds to the transition between 'structure 2' and 'structure 3' which was observed in the thermal expansion data by a dramatic increase of $\alpha_{\|}$. Thus, the TDS data support the idea of a structural transition in the DIP-films manifested in a dramatic increase of $\alpha_{\|}$ as well as of the desorption rate. The increase in desorption rate (for $T \gtrsim 200°C$) was also observed in the x-ray measurements but it could not be quantified precisely (Sec. 7.3.2).

Studies on crystals of alkyl-chains were reviewed by Londsdale and she states "one may expect, by a consideration of melting-point in relation to packing, to gain information about the type of thermal vibration involved and hence about intermolecular forces" [71]. In addition, an "abrupt transformation to a second (...) form (...) a few degrees below their melting points"

was shown [71, 76, 77]. These transformations were accompanied by huge values of thermal expansion in the respective (small) temperature interval ($\alpha = (30000 \ldots 128000) \times 10^{-6}$ 1/K). Following these observations, the transition from 'structure 2' to 'structure 3' for the DIP-films with its large 'thermal expansion coefficient' $\alpha_{\parallel} \approx 1170 \times 10^{-6}$ 1/K appears to be a structural change close to the temperature of a phase-transition. The latter would be caused by exaggeratedly large amplitudes of librational as well as of translational oscillations of the individual molecules.

7.3.5 Conclusions

Summarizing this section (7.3), it may be concluded that

1. DIP films exhibit a thermal stability up to $T \simeq 160$°C followed by a laterally homogeneous desorption process (e.g., layer-by-layer) at higher temperatures with desorption rates of ≈ 1 monolayer DIP per minute at a temperature of $T = 195$°C $\pm$ 10°C.

2. DIP films display reversible thermal expansion with a thermal expansion coefficient nearly parallel to the molecular planes (i.e., out-of-plane for the films under inspection) of $\alpha_{\parallel} = (75.8 \pm 4.5) \times 10^{-6}$ 1/K for temperatures $T \lesssim 160$°C. This thermal expansion (in the reversible stable as-grown 'structure 1') is of the same order as that of other planar molecules.

3. DIP films undergo a first irreversible structural transition ('structure 1' to 'structure 2) for 160°C $\lesssim T \lesssim$ 200°C indicated by almost vanishing thermal expansion at increasing temperatures or even negative values of $\alpha_{\parallel}$. This structural change is correlated with the onset of the laterally homogeneous desorption process. Decreasing the temperature after having reached 'structure 2' leads to a similar $\alpha_{\parallel}$ as observed for

'structure 1'. This results in a hysteresis-like curve when plotting d_{DIP} vs. T in an annealing-cycle.

4. DIP films undergo a second irreversible structural transition ('structure 2' to 'structure 3') for $T \gtrsim 200$°C. This is manifested by a dramatic increase of the lattice parameter d_{DIP} in a small temperature interval ('thermal expansion coefficient' $\alpha_{\|} \approx 1170^{-6}$ 1/K) as well as by a dramatic increase of the desorption rate evidenced in TDS spectra [1]. Decreasing the temperature after having reached 'structure 3' leads to a similar $\alpha_{\|}$ as observed for 'structure 1'. This again results in a hysteresis-like curve when plotting d_{DIP} vs. T in an annealing-cycle.

7.4 In-Plane Structure (GID-Measurements)

In order to determine the in-plane struture of the thin films of DIP grazing incidence diffraction (GID) measurements were carried out on various samples. A 6-circle diffractometer was used to allow for constant incident (α_i) and exit angles (α_f) while scanning the sample azimuthally or scanning the momentum transfer $q_\parallel$. α_i and α_f were set close to the critical angle of the substrates which is $\alpha_{c,\mathrm{Si}} = 0.10°$ and $\alpha_{c,\mathrm{Al_2O_3}} = 0.13°$. A rotating anode x-ray generator provided the x-rays and a HOPG monochromator then selected the characteristic Mo Kα radiation ($\lambda = 0.71$ Å). The slit-settings were chosen in such a way that the obtained in-plane peak widths were not limited by the angular resolution of the measurement (except for one scan which is indicated in the respective data table). The slits perpendicular to this plane (i.e., approximately along q_z) was opened to 5 ... 10 mm to integrate the weak in-plane signals along q_z.

7.4.1 Experimental

Samples

Several samples on two different substrates have been used in the in-plane measurements. In this thesis, the discussion of the typical in-plane (IP) Bragg reflections is restricted to one film prepared on thermally oxidized (4300 Å) Si(111), 'IPsi', and two other films prepared on A-plane sapphire, 'IPsap1' and 'IPsap2'. The preparation conditions are summarized in Table C.1. GID-measurements carried out on still other samples exhibited the same results.

Data refinement and analysis of the radial scans

The Bragg reflections corresponding to the in-plane spacing of the DIP are located at comparatively small values of $q_\parallel$ where a considerable contribution

of air-scattering is still found (for $\lambda = 0.71$ Å the peaks were found at $2\Theta \approx 9.6°$ and $2\Theta \approx 11.2°$, respectively). Thus, they are superimposed on a high background-level which decreases with increasing angles. To separate the signal more clearly from the background, the latter was subtracted from the data using a straight line with the slope of the air-scattering in the respective angular range. Following this procedure the peaks in the refined signal were fitted using a Gaussian to derive their position and width, $\Delta q_{\|}$ (FWHM). The size of the DIP-grains parallel to the surface can be estimated to be at least $2\pi/\Delta q_{\|}$.

Data refinement and analysis of the azimuthal scans of sample 'IPsap2'

Since the signals were rather weak and a noisy background was superimposed on them, they were smoothened by carefully utilizing a low-pass filter. A cut-of frequency of $0.15 \ldots 0.2$ Hz was selected. That is, all signals with a periodicity smaller than $6.66° \ldots 5°$ in ϕ (azimuthal angle) are cut. With these settings peaks are only cut if they exhibit a width of $\Delta\phi < 2.5° \ldots 3.33°$ and therefore the peaks of the DIP are not affected. The data smoothened according to this procedure were fitted using Gaussians to derive positions and widths (FWHM) of the individual peaks. The positions were then related to the position of the substrate in-plane axis ($Al_2O_3(300)$).

7.4.2 Results of the polycrystalline samples

The DIP-film of samples 'IPsi' and 'IPsap1' turned out to be polycrystalline parallel to the surface. Figs. 7.19 and 7.20 show scans along $q_{\|}$ with fixed azimuthal position for 'IPsi' and 'IPsap1', respectively. The Bragg-reflections could unambiguously be attributed to the DIP-film. In Table 7.5 the positions of the Bragg-reflections and the corresponding lattice parameters are

summarized.

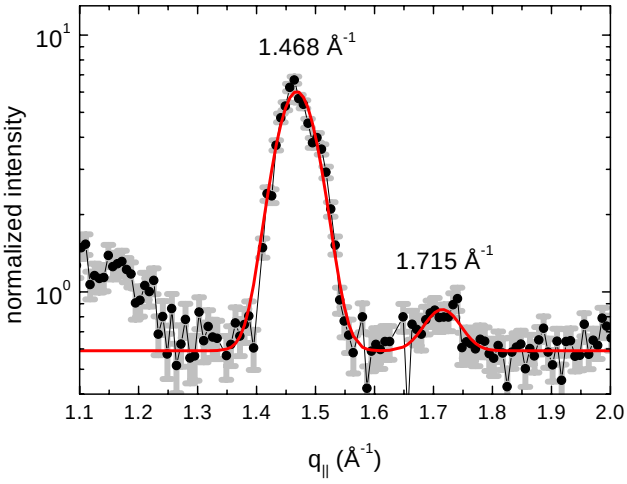

Figure 7.19: Scan along $q_{\|}$ at fixed azimuthal position on a polycrystalline DIP-film grown on thermally oxidized silicon (sample 'IPsi'). The shaded area displays the statistical error of the data (filled circles). The solid line is a fit to the data using 2 Gaussians. Note the log-scale for the intensity.

Repeating the scans along $q_{\|}$ at arbitrary azimuthal positions did not show significant differences. Azimuthal scans at fixed $q_{\|}$ showed a constant intensity. These observations provide evidence for the polycrystalline (in-plane) structure of the DIP-film and this was expected for sample 'IPsi' (grown on silicon oxide). The polycrystallinity of the DIP-film on the sapphire substrate may be explained by the preparation conditions of the film and/or by the substrate surface prior to deposition.

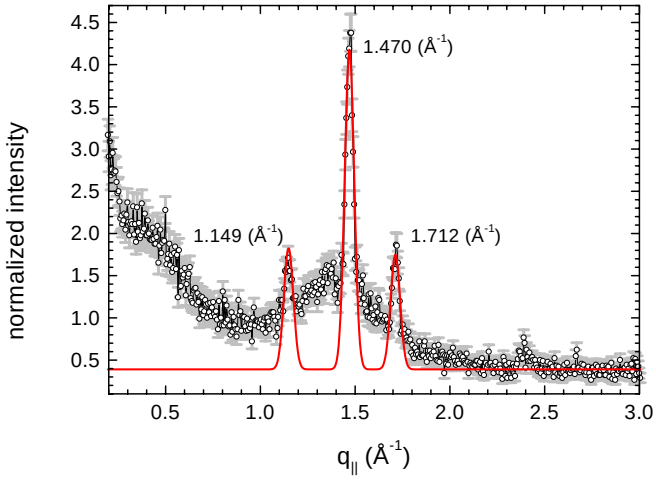

Figure 7.20: Scan along $q_{\|}$ at fixed azimuthal position on a polycrystalline DIP-film grown on A-plane sapphire (sample 'IPsap1'). The shaded area displays the statistical error of the data (open circles). The solid line is a fit to the data using 3 Gaussians.

7.4.3 Oriented DIP-film on A-plane sapphire, 'IPsap2'

Azimuthal and radial scans

At the radial peak positions given in Table 7.5 for 'IPsi' and 'IPsap1', azimuthal scans were carried out on sample 'IPsap2'. The results of the scan showed that this sample exhibited an anisotropic, i.e., ordered structure parallel to the substrate surface. However, 'IPsap2' showed peaks in the intensity only on two of the three positions of $q_{\|}$ depicted in Fig. 7.20, namely at $q_{\|} \approx 1.48$ Å^{-1} and at $q_{\|} \approx 1.72$ Å^{-1}. For an overview, Fig. 7.21 displays the relative orientation of the reflections with respect to the substrate c-axis. This peak-map is explained in detail below.

The azimuthal scans at the positions of $q_{\|}$ from Table 7.5 are shown in

sample	peak position (Å^{-1})	$d_{\parallel}$ (Å)	$\Delta q_{\parallel}$ (FWHM) (Å^{-1})	$2\pi/\Delta q_{\parallel}$ (Å)
IPsi	1.468 ± 0.01	4.28 ± 0.03	0.078 ± 0.005	≈ 80
	1.715 ± 0.02	3.66 ± 0.045	0.07 ± 0.01	≈ 90
IPsap1	1.149 ± 0.007	5.468 ± 0.03	0.06 ± 0.01	≈ 100
	1.470 ± 0.007	4.274 ± 0.03	0.06 ± 0.01	≈ 100
	1.712 ± 0.008	3.670 ± 0.03	0.06 ± 0.01	≈ 100
IPsap2	1.477 ± 0.01	4.254 ± 0.03	0.06 ± 0.005	≈ 100
	1.719 ± 0.015	3.654 ± 0.03	$0.075^{\dagger} \pm 0.01$	$\approx 85^{\dagger}$

Table 7.5: Radial in-plane peak positions and peak width for the DIP-film of samples 'IPsi', 'IPsap1', and 'IPsap2'. (see also Figs. 7.19, 7.20, 7.24, and 7.25). $2\pi/\Delta q_{\parallel}$ gives a lower limit for the in-plane domain size.
†The width of this peak is close to the radial resolution used in the scan ($\delta q_{\parallel} \approx 0.065$ Å^{-1}).

Fig. 7.22 for $q_{\parallel} \approx 1.48$ Å^{-1} and in Fig. 7.23 for $q_{\parallel} \approx 1.72$ Å^{-1}. Due to the twofold symmetry of the sapphire substrate an azimuthal scan over a range of 180° provides all information about the peak positions. This is confirmed by the 360°-scan at $q_{\parallel} = 1.48$ Å^{-1} (Fig. 7.22), where the peaks are symmetric with respect to the substrate c-axis ($Al_2O_3(300)$). The azimuthal positions of the peaks as derived by the fits are summarized in Table 7.6. The angular spread of the crystallites (i.e., the perfection of the crystal-lattice) is given by the width $\Delta\phi$ of the peaks. $\Delta\phi$ is in the range of $5° \ldots 9°$ for all observed peaks.

To assure that the peaks in azimuthal scans are not artifacts, radial scans were carried out over two azimuthal peaks for each $q_{\parallel}$ (see Fig. 7.24 for $q_{\parallel} = 1.47$ Å^{-1} and Fig. 7.25 for $q_{\parallel} = 1.72$ Å^{-1}). The peak positions obtained from these scans are listed in Table 7.5. The inverse width of the radial scans

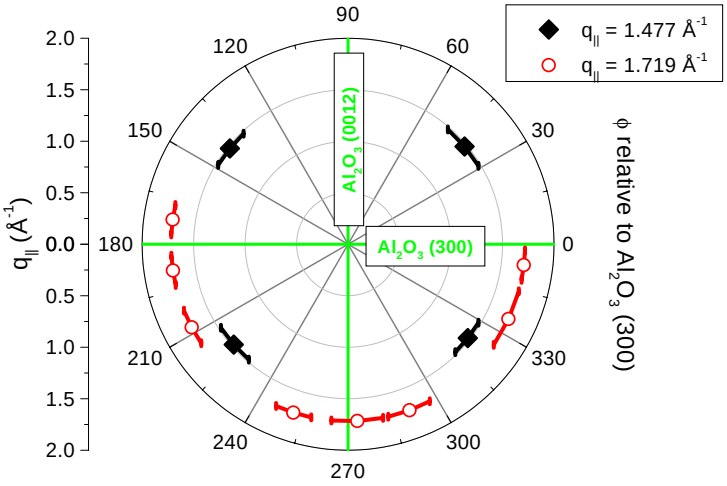

Figure 7.21: Map of DIP-reflections in the plane of the substrate. The azimuthal angle is given with respect to the $Al_2O_3(300)$ direction of the substrate. Filled diamonds are reflections with $q_{\parallel} = 1.477$ Å^{-1}, open circles are reflections with $q_{\parallel} = 1.719$ Å^{-1}. The peak-width along $q_{\parallel}$ is smaller than the size of the symbols. The solid lines through the symbols account for the measured azimuthal peak width, $\Delta\phi$.

$(2\pi/\Delta q_{\parallel})$ is a lower limit for the mean extension of the DIP-grains along the respective momentum transfer. This size was found to be of the order of $\gtrsim 100$ Å for both values of $q_{\parallel}$.

A certain degree of azimuthal order of the DIP-film is confirmed by ellipsometry measurements. Fig. 7.26 exhibits the two ellipsometric quantities $\tan\Psi$ and $\cos\Delta$. A slight optical anisotropy is seen under an azimuthal rotation of the sample 90° even if the anisotropy is not as pronounced as for sample 'IPsap3' (Fig. 7.5).

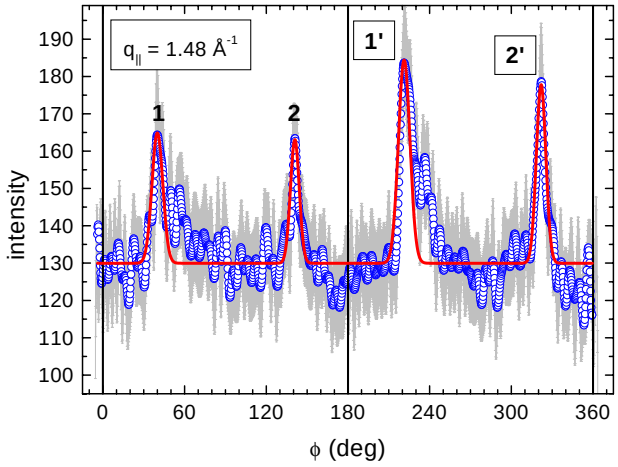

Figure 7.22: Azimuthal distribution of the in-plane peaks with $q_{\|} = 1.477$ Å^{-1}. The grey area displays the zone of statistical error around the data (open circles). The solid line represents a fit to the data with four Gaussians and the solid vertical lines indicate the azimuthal positions of the $Al_2O_3(300)$ and $Al_2O_3(\overline{3}00)$-peaks, respectively. At the azimuthal positions of peaks $1'$ and $2'$, radial scans have been carried out (see Fig. 7.24).

In-plane peak map (Fig. 7.21)

The results of the azimuthal scans are summarized in Fig. 7.21. The angles in ϕ are depicted relative to the axis through the $Al_2O_3(300)$ and $Al_2O_3(\overline{3}00)$-peak (c-axis). The directions of the two substrate's main axes are indicated.

The twofold symmetry of the substrate is mirrored in the DIP-peaks, which are symmetric with respect to the axes. The azimuthal positions of the peaks at $q_{\|} = 1.477$ Å^{-1} are rotated by $\approx 40°$ with respect to the c-axis. This implies a relative distance between the peaks of 80° and 100°, respectively, and the existence of two domains in the plane.

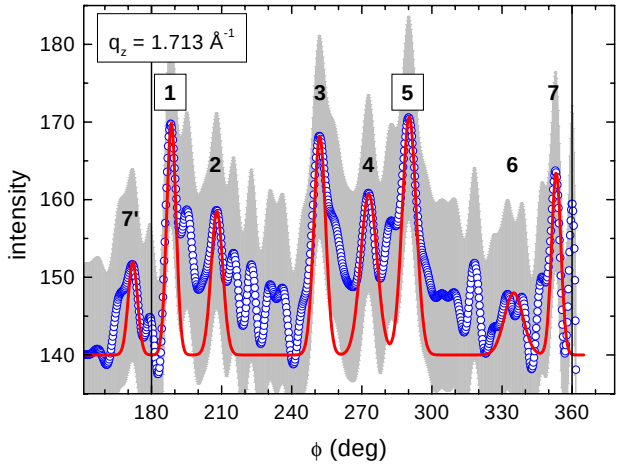

Figure 7.23: Azimuthal distribution of the in-plane peaks with $q_{\|} = 1.719$ Å^{-1}. The grey area displays the zone of statistical error around the data (open circles). The solid line represents a fit to the data with four Gaussians and the solid vertical lines indicate the azimuthal positions of the $Al_2O_3(300)$ and $Al_2O_3(\overline{3}00)$-peaks, respectively. At the azimuthal positions of peaks 1 and 5, radial scans have been carried out (see Fig. 7.25).

For $q_{\|} = 1.477$ Å^{-1} there exist at least 7 peaks although the peaks are quite broad and weak in their signal-to-noise ratio. They can be ordered in 2 groups

1. The peak-pairs (1,2) and (6,7). They are mirror-symmetric with respect to the axis through the $Al_2O_3(0012)$- and $Al_2O_3(00\overline{12})$-peaks.

2. The peak triplet (3,4,5). It is (almost) mirror-symmetric with respect to the axis through the $Al_2O_3(0012)$- and $Al_2O_3(00\overline{12})$-peaks.

Also in the angular distance between these peaks one can find the values $\Delta\phi = 80°$ and $\Delta\phi = 100°$, namely in the peak triplets: (7-4)-(4-7′), (1-4)-

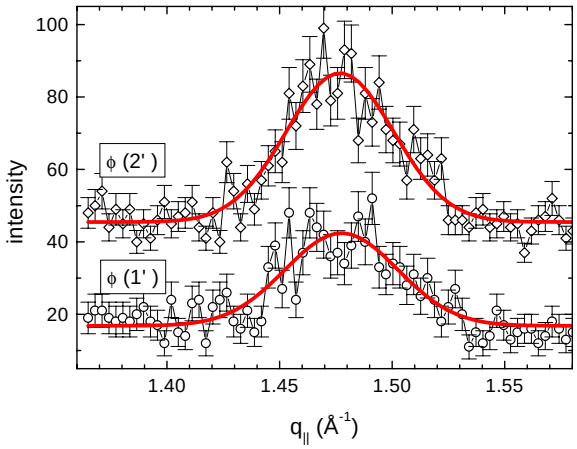

Figure 7.24: Radial scans over the peaks $1'$ and $2'$ of Fig. 7.22, respectively, confirming $q_{\|} = 1.477$ Å^{-1}

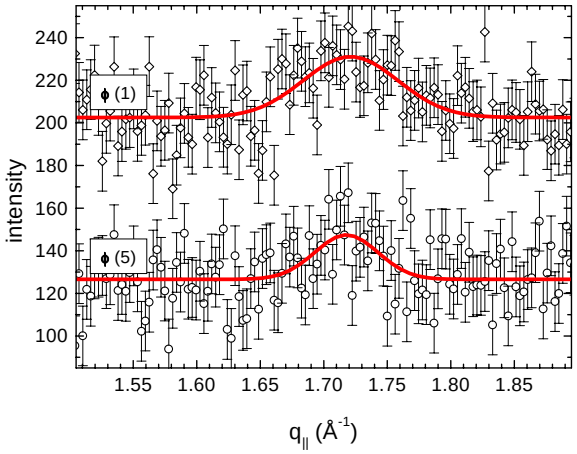

Figure 7.25: Radial scans over the peaks 1 and 5 of Fig. 7.23, respectively, confirming $q_{\|} = 1.719$ Å^{-1}

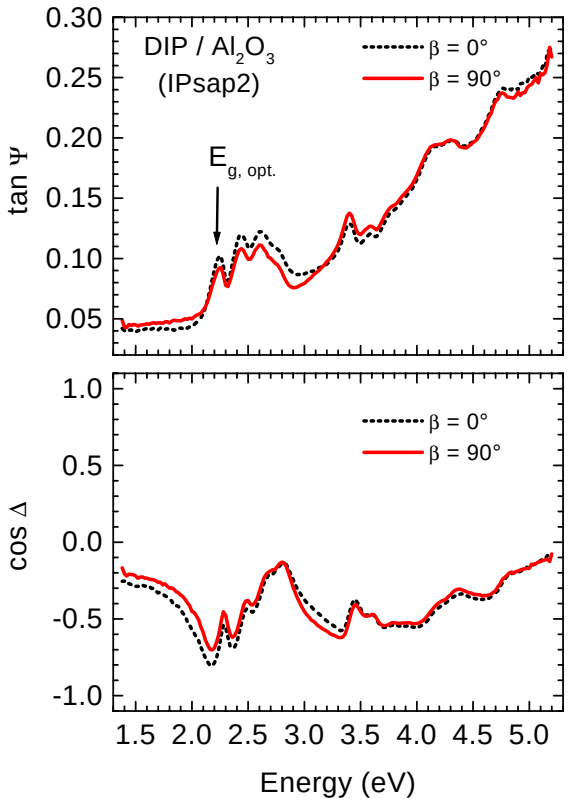

Figure 7.26: Ellipsometry on a DIP-film grown on A-plane sapphire (sample 'IPsap2'). The optical bandgap of $E_{g,opt.} = (2.2 \pm 0.1)$ eV is seen as well as the optical anisotropy under an azimuthal rotation of the sample of 90°. The incidence angle was $\phi = 60°$ (measurements carried out by I. Alonso).

(4-1′), (2-5)-(5-2′), and (6-3)-(3-6′). For the peaks 1′, 2′, and 6′ the values in brackets of peak 1, 2, and 6 of Table 7.6 were taken.

$q_\parallel = 1.719 \pm 0.006$ Å^{-1}			$q_\parallel = 1.477 \pm 0.002$ Å^{-1}		
Peak	ϕ (deg) (rel. to $Al_2O_3(300)$)	$\Delta\phi$ (deg) (FWHM)	Peak	ϕ (deg) (rel. to $Al_2O_3(300)$)	$\Delta\phi$ (deg) (FWHM)
1	188.5 ± 0.3	4.8 ± 0.5	1	40.0 ± 0.3	9.0 ± 0.5
	(8.5 ± 0.3)		2	141.0 ± 0.3	7.6 ± 0.5
2	208.0 ± 0.3	6.0 ± 0.5	$1'$	221.3 ± 0.3	8.0 ± 0.5
	(28.0 ± 0.3)			(41.3 ± 0.3)	
3	252.0 ± 0.3	6.0 ± 0.5	$2'$	321.9 ± 0.3	7.1 ± 0.5
	(72.0 ± 0.3)			(141.9 ± 0.3)	
4	273.0 ± 0.3	8.4 ± 0.5	—	—	—
	(141.9 ± 0.3)				
5	290.3 ± 0.3	7.2 ± 0.5	—	—	—
	(110.3 ± 0.3)				
6	335.0 ± 0.3	9.6 ± 0.5	—	—	—
	(155.0 ± 0.3)				
7	353.2 ± 0.3	4.8 ± 0.5	—	—	—
	(173.2 ± 0.3)				
$7'$	172.0 ± 0.3	4.8 ± 0.5	—	—	—

Table 7.6: Azimuthal position of the in-plane peaks with $q_\parallel = 1.719$ Å^{-1} and $q_\parallel = 1.48$ Å^{-1} relative to the azimuthal position of the $Al_2O_3(300)$ peak. The ϕ-values in brackets denote the positions with respect to the $Al_2O_3(\overline{3}00)$ position. Due to the twofold symmetry of the sapphire substrate in the plane, the primed peaks ($7'$, $1'$, and $2'$) are essentially the same as the unprimed peaks (7, 1, and 2). Underlined peaks mark the azimuthal positions at which radial ($q_{||}$) scans were performed to fix the peak position in $q_\parallel$ (see Figs. 7.24 and 7.25).

7.4.4 Discussion

The GID measurements on DIP-films deposited on silicon-oxide and A-plane sapphire, respectively, clearly show two charcteristic lattice constants of the DIP-film parallel to the surface. The radial peaks at $q_\parallel \approx 1.47$ Å^{-1} and $q_\parallel \approx 1.47$ Å^{-1} correspond to lattice constants of $d_{\parallel,1} = 4.25 \ldots 4.28$ Å and

$d_{\parallel,2} = 3.65 \ldots 3.67$ Å. The latter value often is reported to be the typical 'van-der-Waals'-distance in aromatic organic crystals (normal to the molecular plane) [71].

On a sapphire-substrate with A-plane orientation even orientational order parallel to the substrate was found. The structural anisotropy was confirmed by ellipsometry-measurements on this ('IPsap2', Fig. 7.26) and another DIP-film on A-plane sapphire ('IPsap3', Fig. 7.5). The azimuthal distribution and the number of Bragg-reflections (4 peaks in 360°) with $q_{\parallel} = 1.477$ Å^{-1} points to at least 4 domains of DIP inside the film (2 rotational and 2 mirror domains) that are symmetrically aligned along the main axes of the substrate. However, due to the large peak width in azimuthal scan direction at both observed $q_{\parallel}$-values the presence of additional domains or even of two or more slightly different polymorphs could not be excluded. Such different polymorphs and different domains are often present in the low-symmetry structures of organics in thin films, e.g., PTCDA on Ag(111) [74]. It is quite obvious that the DIP thin-film structure does not show a very high symmetry since the bulk-structure is already complex (as has been pointed out in Chapter 3).

The relatively large azimuthal DIP peak widths (compared to the narrow width of the sapphire reflections of the order of 0.01°) may also suggest a different scenario. Here, the DIP-film does not establish an epitaxial relationship with the substrate. It rather is plausible that the DIP-molecules underlay a kind of 'morphology induced' growth mode where they align along preferred orientations of the substrate (e.g., steps in the surface along the main axes of the sapphire due to the miscut).

However, a full crystallographic analysis of the DIP-films is beyond the scope of this thesis. Nevertheless, combining the out-of-plane lattice constant and the in-plane lattice constants of the DIP-films demonstrates that the film-structure is quite different from the structure found in the bulk of DIP-

crystallites. None of the characteristic lattice constants found in the thin films show up in the bulk structure [33].

Furthermore, a comparison of the lattice parameters with the results of Hoshino *et al.* for the crystallographic structure of DIP thin films on NaCl and on perylene [35] (Sec. 3.3) also shows differences. The out-of-plane lattice constant which was found for DIP/SiO_2, $d_{DIP} \approx 16.6$ Å, is close only to the value $c' = 16.82$ Å for DIP(150 Å)/perylene reported in Ref. [35]. However, the in-plane lattice constants of $d_{||} = 4.27 \pm 0.02$ Å and $d_{||} = 3.66 \pm 0.02$ Å which are found for DIP/SiO_2 as well as for DIP/$Al_2O_3(11\bar{2}0)$ are not consistent with the values of Ref. [35].

In conclusion, the measurements of DIP thin films reveal that the crystallographic structure in DIP thin films deposited on SiO_2 and $Al_2O_3(11\bar{2}0)$ is markedly different from that observed in DIP single-crystals as well as from DIP deposited on NaCl and perylene.

Chapter 8

Scaling Exponents and Growth of DIP Thin Films

Recently it has been shown that the structure (and as a consequence the physical properties) of thin organic layers depend crucially on the conditions employed during growth [78]. Therefore, knowledge of the growth mechanism is necessary to predict structural features and to allow for a better control of the structural order.

In the last two decades a theoretical framework has been established which relates the mechanism involved in the growth of a thin film to a set of scaling exponents describing the dependence of the surface roughness on film thickness and lateral length scale. A lot of effort has been spent to theoretically predict scaling exponents for certain growth models, as well as to determine them experimentally for a large variety of thin film systems [2, 3, 19]. However, detailed studies that independently measure several scaling exponents with complementary techniques are rare (see Refs. [3] and [19]). Moreover, there are only very few studies concerning the scaling exponents of organic thin films and in particular of small molecules deposited under UHV-conditions [4, 5, 7, 79]. In this chapter the independent determi-

nation of the scaling exponents α, β and z is reported for highly ordered thin films of DIP deposited onto silicon-oxide substrates in ultra-high vacuum (UHV) employing non-contact AFM (NC-AFM), specular x-ray-reflectivity and diffuse x-ray scattering.

8.1 Theory

The scaling theory of growth-induced surface roughness is based on the behavior of the height difference correlation function (HDCF), $g(R)$, which has already been defined in Sec. 4.2.3, Eq. 4.23. The HDCF can be evaluated from real space images by a spatial average over one or several regions, which should be much larger than R in order to avoid edge effects. The HDCF displays distinct behaviors for $R \ll \xi$ and $R \gg \xi$, where ξ denotes the correlation length. For $R \ll \xi$ one expects a power law increase as $g(R) \approx a^2 R^{2\alpha}$, where α is the static roughness exponent and the prefactor a is a measure of the typical surface slope. For $R \gg \xi$ the heights at distance R become uncorrelated, hence $g(R)$ saturates at the value $g(R \gg \xi) = 2\sigma^2$, where σ is the rms-width (defined in Chapter 4, Eq. 4.18). Thus, the scaling behavior of $g(R)$ reads:

$$g(R) \quad \sim \quad \begin{cases} a^2 R^{2\alpha} & \text{as} \quad R \longrightarrow 0 \\ 2\sigma^2 & \text{as} \quad R \longrightarrow \infty \end{cases} \tag{8.1}$$

and is schematically displayed in Fig. 8.1.

The three parameters σ, ξ and a evolve with film thickness according to the power laws

$$\sigma \sim D^{\beta}, \tag{8.2}$$

$$\xi \sim D^{1/z}, \tag{8.3}$$

$$a \sim D^{\lambda} \tag{8.4}$$

defining the growth exponent β, the dynamic exponent z and the steepening

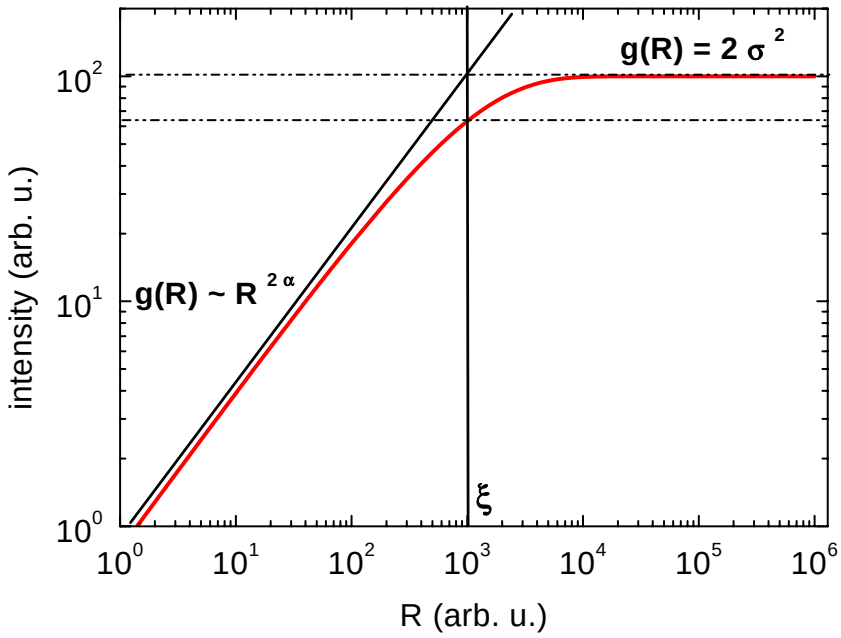

Figure 8.1: Schematic for the scaling behavior of $g(R)$ for real samples.

exponent λ. Assuming that the regimes $R \ll \xi$ and $R \gg \xi$ are connected through a scaling form

$$g(R) = 2\sigma^2 \tilde{g}(R/\xi) \tag{8.5}$$

it follows that the scaling exponents are related by $\beta = \alpha/z + \lambda$. For $\lambda = 0$ (no steepening) one has $\beta = \alpha/z$. Scaling with $\lambda > 0$ is referred to as *anomalous* [19].

The roughness parameters of the surface can also be determined by analyzing diffuse x-ray scattering data. The diffusely scattered intensity is given by Eq. (4.27).

To evaluate the integral (4.27) the scaling function $\tilde{g}(x) = 1 - \exp(-x^{2\alpha})$

inserted in the scaling form (Eq. 8.5) is commonly used[1] [8]. This allows to fit the diffusely scattered intensity of a given sample with only two free parameters, α and ξ, since σ can be determined independently by x-ray reflectivity measurements.

The various methods to determine the roughness exponent α, the inverse dynamic exponent $1/z$, and the growth exponent β are summarized in Table 8.1. The steepening exponent λ can be determined by fitting a straight line to a log-log-plot of a vs. D. The slope gives λ.

α ($g(R)_{R\ll\xi} \propto R^{2\alpha}$) (and a)	$1/z$ ($\xi \propto D^{1/z}$)	β ($\sigma(D) \sim D^{\beta}$)
AFM (several spots) - log-log plot $g(R)$ - slope ($R \ll \xi$): 2α - $y_0 = 2 \log a$	**AFM** (several spots, $L \gg \xi$) - determine ξ from $g(R)$ - log-log plot $\xi(D)$ - slope: $1/z$	**AFM** (samples with different D) - log-log plot $\sigma(D)$ - slope: β
XRD - fit rocking-scan intensity (Eq. 4.26) with analytical form of C(R) - fit parameters: α, $\xi(D)$	**XRD** (samples with different D) - fit rocking-scan intensity - log-log plot $\xi(D)$ - slope: β	**X-ray Reflectivity** - determine σ for various D - log-log plot $\sigma_\infty(D)$ - slope: β

Table 8.1: Experimental methods for the determination of α, $1/z$, and β

8.2 Experimental procedure

DIP-films with various film thicknesses (69 Å $\leq D \leq$ 9000 Å) were prepared on atomically smooth oxidized (4000 Å) Si(100) substrates at a substrate

[1]Note that this simple analytical function fulfills the asymptotical conditions of $g(R)$ of real samples (Eq. 8.1).

temperature of 145±5°C and at a deposition rate of 12±3 Å/min under UHV-conditions (base-pressure better than 2×10^{-10} mbar). Details for the samples 'o69' ... 'o9000' are found in Table C.1. Prepared under these conditions the DIP-molecules adsorb on SiO_2 standing essentially upright ($d_{DIP} \approx 16.55$ Å, see Chapter 7) with a tilt-angle ϕ presumably around 15°-20° which gives rise to the formation of 'tilt-domains' (right-hand side of Fig. 8.2).

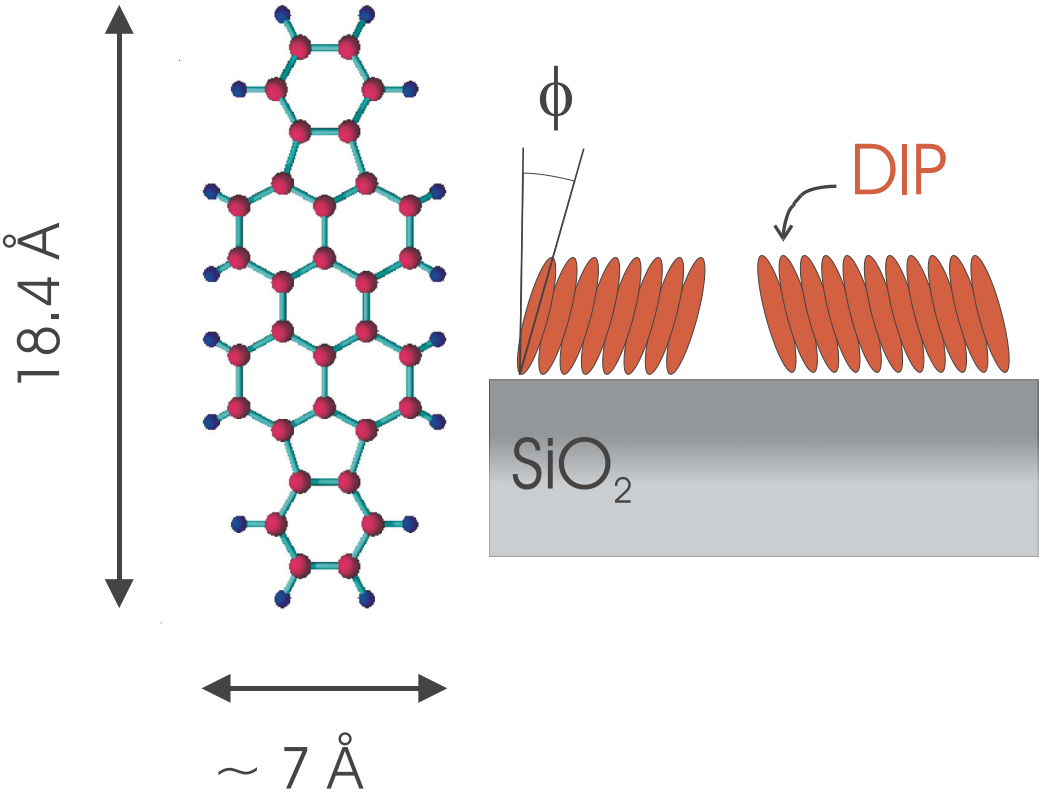

Figure 8.2: Left-hand side: the extensions of a DIP-molecule. Right-hand side: schematic for the formation of 'tilt-domains'.

For most of the samples, NC-AFM measurements were carried out immediately after deposition on several spots of the sample in the analysis chamber (see Sec. 6.1.1) without breaking the UHV (OMICRON-AFM, scan-range

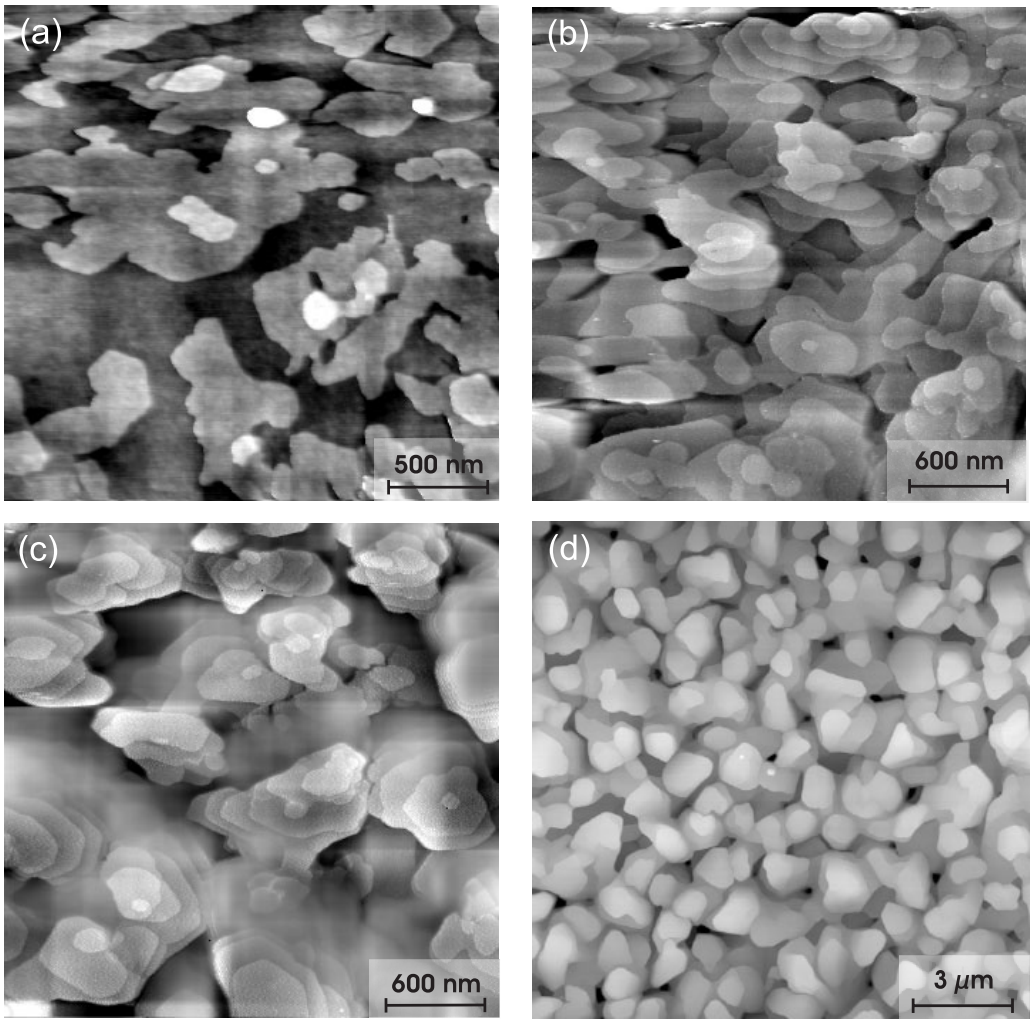

Figure 8.3: Non-contact AFM of DIP/SiO with various film thickness: (a) $D = 126$ Å, (b) $D = 396$ Å, (c) $D = 1100$ Å, (d) $D = 9000$ Å

$L \leq 5\,\mu$m). Measuring the samples once more after several weeks in air did not show any differences in the surface topography. Subsequently, $g(R)$ was calculated for each spot on the sample and the resulting bunch of HDCF's for each sample was averaged. The slope of a linear fit to the small-R region in a log-log-plot of the averaged function $g(R)$ provides an estimate of 2α.

The thickest sample (9000 Å) has been measured in a DI Nanoscope III AFM in air due to its larger lateral scanning range (up to 16 μm). To assure that the true saturation roughness was obtained for this sample, the roughness of several images with different scan-ranges L was determined. It turned out that for $L \geq 10\,\mu$m, σ does not change upon further increasing L.

X-ray measurements were carried out at beamline ID10B at the ESRF in Grenoble, France employing a wavelength $\lambda = 1.563(2)$ Å (see Sec. 6.2.2). The saturation roughness σ of the samples with $D \leq 1100$ Å was characterized by analyzing their specular x-ray-reflectivity (see Sec. 7.2.1 and Table 7.1). Diffuse x-ray scattering data was recorded at several scattering-vectors $2\Theta \leq 2^\circ$ in rocking-scans, where the incident angle, α_i, is varied while $2\Theta = \alpha_i + \alpha_f$ is kept constant (α_f denotes the exit angle). The data was then fitted according to Eq. 4.27 [80] with σ taken from the analysis of the reflectivity data. The resulting values for α and ξ of the different positions in 2Θ for each sample were averaged[2].

8.3 Results

Figure 8.3 displays NC-AFM images of samples with different film thickness D_{DIP}. The increase in surface roughness with increasing film thickness is clearly visible. Figure 8.4 shows the averaged HDCF for five samples with different film thickness, three of which correspond to the samples shown in Fig. 8.3 (a)-(c). The resulting roughness exponent α for the individual samples is displayed in the inset and listed in Table 8.2. An average value of

[2]Note, that the transversal coherence length of the beam is $\chi_{trans,0} \gtrsim 15000$ Å for normal incidence, see Table 6.1. For a beam impinging on the sample under an angle of α_i the transversal coherence length on the sample is $\chi_{trans}(\alpha_i) = \chi_{trans,0}/\sin\alpha_i$. This implies that χ_{trans} at the incident angles employed is much larger than the maximum correlation length ξ determined by analyzing the rocking scans.

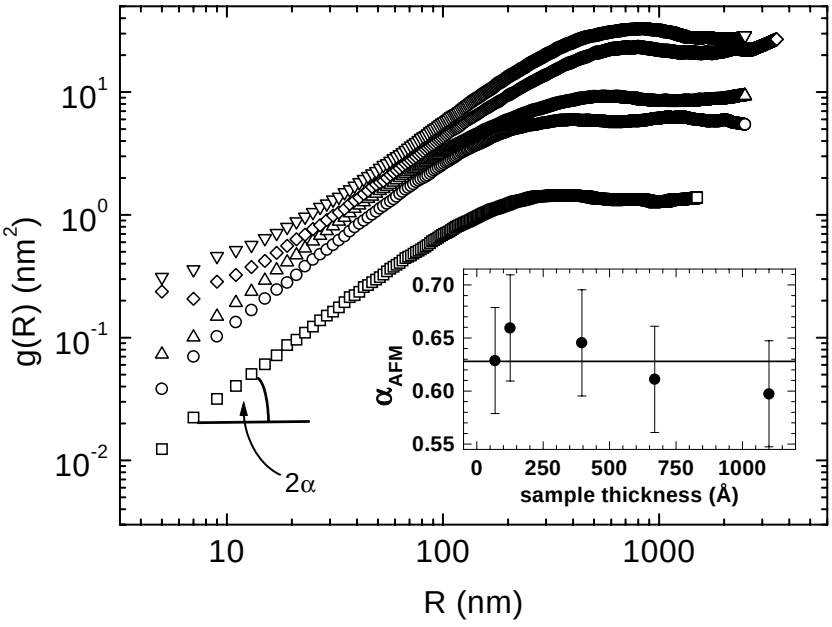

Figure 8.4: Averaged $g(R)$ for five samples with different film thickness D ($\square$ = 69 Å, O = 126 Å, $\triangle$ = 396 Å, ∇ = 670 Å, $\diamondsuit$ = 1100 Å). The inset displays the roughness exponent α obtained by fitting the linear part of $g(R)$ as a function of sample thickness, the solid horizontal line denotes the average of α for the five samples.

$\alpha_{AFM} = 0.628 \pm 0.05$ has been determined.

The roughness exponent as well as the inverse dynamic scaling exponent $1/z$ have additionally been determined by fits of diffuse x-ray scattering in rocking-scan geometry as described above. Inset (a) of Fig. 8.5 shows a typical rocking-scan and a fit to the data. The main plot of Fig. 8.5 displays the correlation length ξ as a function of the film thickness (see also Table 8.2). A linear fit to this log-log-plot gives $1/z = 0.92 \pm 0.20$. The average roughness

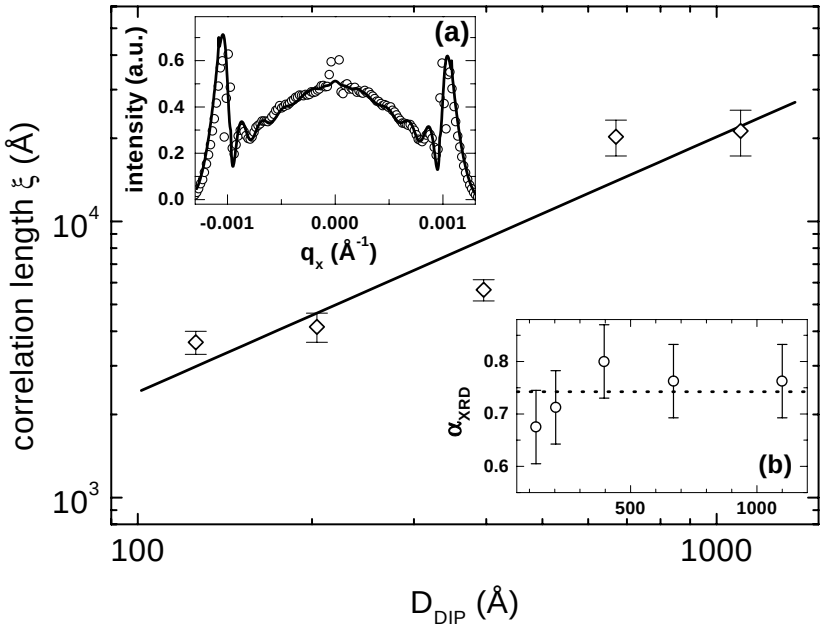

Figure 8.5: Values of ξ as obtained by fits to rocking scans over the specular rod of various samples. The solid line is a linear fit to the data which gives $1/z = \beta/\alpha$. Inset (a) displays a rocking scan (open circles) and a fit (solid line) associated with the data for a DIP-film with $D_{DIP} = 396$ Å recorded at $2\Theta = 1.5°$. Inset (b) displays the values of α as obtained by fits to the rocking scans; the dotted line denotes the average of α for the five investigated samples.

exponent determined by x-ray diffuse scattering (XRD) is denoted in inset (b) of Fig. 8.5 as dotted line; $\alpha_{XRD} = 0.74 \pm 0.07$ was obtained, which is slightly larger than α_{AFM}. The average roughness exponent defined by $\tilde{\alpha} = (\alpha_{AFM} + \alpha_{XRD})/2$ is then given by $\tilde{\alpha} = 0.684 \pm 0.06$.

Figure 8.6 shows the rms-roughness as derived from the analysis of specu-

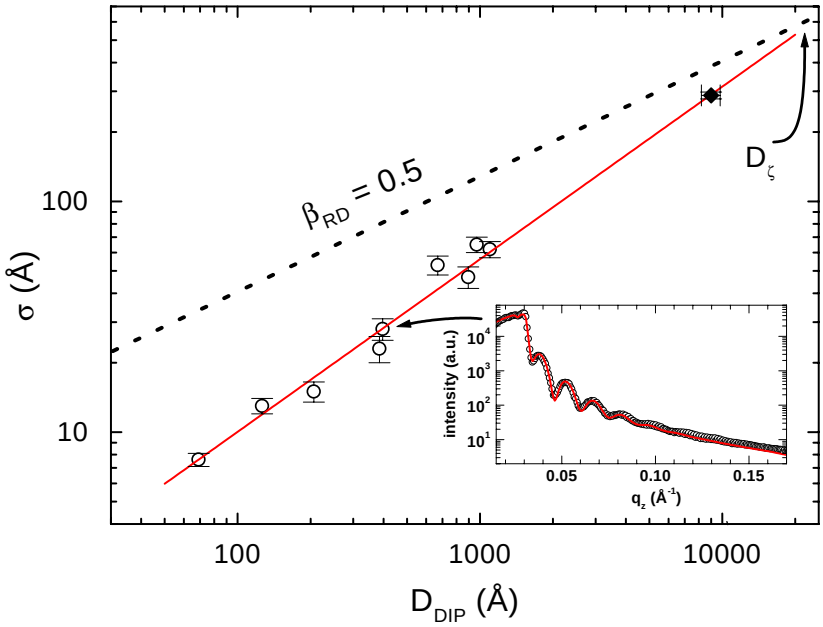

Figure 8.6: Log-log plot of σ vs. D and a linear fit to the data which gives $\beta = 0.748 \pm 0.05$. For $D \leq 1100$ Å, x-ray-reflectivity was used to determine σ (open circles), see inset as a typical example for a sample with $D = 396$ Å. For the thickest sample ($D = 9000$ Å), NC-AFM-images were used to determine σ (filled diamond). The black dotted line with slope $\beta_{RD} = 0.5$ corresponds to the random deposition limit σ_{RD}, which would be reached at $D_{DIP} = D_\zeta$. Details are explained in the text.

lar x-ray reflectivity data and from the analysis of several AFM-images of sample 'o9000'. The values of σ are summarized in Table 8.2. The solid line in the main plot is a linear fit to the data and the growth exponent is obtained as $\beta = 0.748 \pm 0.05$. The dotted line denotes the random deposition limit [2]

$$\sigma_{RD} = d_{DIP}\sqrt{D_{DIP}/d_{DIP}} \tag{8.6}$$

which will be used in the discussion below. Note that the inspected range of film thickness D_{DIP} covers more than two orders of magnitude, and that no systematic deviation from the power law can be detected. The estimate of β is clearly the most reliable among the exponents determined in this experiment.

Using the quoted values for α, β and z, the steepening exponent λ is estimated to be 0.17 (0.07) for $\alpha = \alpha_{AFM}$ ($\alpha = \alpha_{XRD}$). This suggests that some steepening is present, but that the effect is rather weak, consistent with the modest upward shift of the HDCF's displayed in Fig. 8.4 with increasing film thickness.

8.4 Discussion

Two main mechanisms for growth-induced surface roughening have been described in the literature. In *kinetic roughening*, the roughness arises from the competition between the shot noise and surface smoothening through surface diffusion, desorption and related processes. The resulting morphology is self-affine, showing statistical scale invariance on length scales below the correlation length ξ. In contrast, in *mound growth* a pattern with a well-defined characteristic length scale develops as a consequence of a morphological instability, which is usually associated with reduced interlayer transport. The scaling picture sketched above applies in both cases, with the mound size playing the role of the correlation length ξ in the second scenario. The two scenarios differ in the shape of the HDCF, which should display clear oscillations in the case of mound growth [81].

The estimates for α obtained in this work are consistent with kinetic roughening in the conserved KPZ universality class, for which $\alpha \approx 2/3$ [82].

sample	D (Å)	σ_∞ (Å)	α_{AFM}	α_{XRD}	ξ_{XRD} (nm)
'o69'	69.0 ± 1	7.6 ± 0.5	0.63 ± 0.05	—	—
'o126'	126.2 ± 1	13.0 ± 1	0.66 ± 0.05	0.68 ± 0.07	365 ± 35
'o206'	206.3 ± 2	15.0 ± 1.5	—	0.71 ± 0.07	415 ± 50
'o385'	384.7 ± 2	23.0 ± 3	—	—	—
'o396'	396.5 ± 2	28.0 ± 3	0.65 ± 0.05	0.8 ± 0.07	565 ± 50
'o670'	670 ± 4	53 ± 5	0.61 ± 0.05	0.76 ± 0.07	2025 ± 300
'o890'	890 ± 5	47 ± 4	—	—	—
'o970'	970 ± 8	65 ± 5	—	—	—
'o1100'	1100 ± 10	62 ± 5	0.60 ± 0.05	0.76 ± 0.07	2125 ± 400
'o9000'	9000 ± 800	288 ± 10	—	—	—
$\bar{\alpha}_{AFM}$			0.628 ± 0.05		
$\bar{\alpha}_{XRD}$			0.74 ± 0.07		
$1/z$			0.92 ± 0.20		
β			0.748 ± 0.05		

Table 8.2: Summarized results for the scaling exponents

Similar values are commonly reported for inorganic films [3]. For mounds the asymptotic value of the static roughness exponent is $\alpha = 1$, but in practice much lower values may occur [81, 83]. Hence a case of noisy mound growth also cannot be ruled out for the DIP films. By visual inspection, Figs. 1 (a) and (b) suggest an essentially random appearance of the surface, while Fig.1 (d) resembles a mound pattern (compare to Fig. 1 of [83]). However, both scenarios have considerably difficulty in explaining the large values of $1/z$ and β. For conserved KPZ growth $1/z \approx 0.3$ and $\beta \approx 0.2$ due to the scaling relation [19] $z = 2 + 2\alpha$. For mound growth large values of β up to $\beta \approx 0.8$, have been observed in simulations, but this behavior is restricted to

an intermediate regime associated with considerable steepening, where the dynamic exponent takes on a conventionally low value of $1/z \approx 0.2-0.3$ [84].

Both in kinetic roughening and in mound growth the random deposition limit σ_{RD} (Eq. 8.6) is expected to provide an absolute upper bound on the surface roughness. This bound is attained if every particle remains on the height level where it was deposited, a situation that can be realized in metal homoepitaxy at low temperatures [85]. Roughness beyond σ_{RD} can occur only if matter is transported to higher layers, which seems hard to rationalize in the absence of a thermodynamic driving force (e.g., dewetting). Although the DIP data in Fig. 8.6 remain below σ_{RD} for all film thicknesses, the fact that we observe no deviation from the power law suggests that the scaling with $\beta > 1/2$ will continue also beyond the point where the DIP roughness crosses the RD limit (for $D \geq D_\zeta$). *Rapid roughening* [19] with $\beta > 1/2$ has previously been reported for a number of systems [4, 5, 86–89] which will be briefly reviewed in the following. In addition the few studies on organic systems will also be reviewed.

8.4.1 Systems which exhibit $\beta > 0.5$

Fang *et al.* studied the homoepitaxy of Pb/Pb(100) employing high-resolution LEED [86]. They obtained $\beta = 0.77 \pm 0.05$ and suggested that facetting of the surface is responsible for this large value[3].

In an AFM-study, Collins *et al.* investigated the scaling exponents of 'plasma polymer films' [4]. The films were prepared at relatively high rates of ≈ 1 μm/h and $T \approx 320$ K by employing an rf driven plasma discharge and hydrogen and trans-2-butene as reactant gases in a vacuum chamber. Depending on the growth rate, $0.7 \leq \beta \leq 1$ was obtained. The authors

[3]This conclusion is questionable since they derived the reported growth exponent in a range of thickness where facetting was not yet observed

speculate that the bad vacuum conditions might have caused this high values. This explanation is reasonable since bad vacuum, in particular a high partial pressure of hydrogen is supposed to enhance *rapid roughening* at least for metal MBE ([19], p. 265). In a microscopic picture, bad vacuum may lead to lateral inhomogeneities in the local growth rate. The latter is discussed below (Sec. 8.4.3)

Lee *et al.* determined the growth exponent for deposition of aluminum onto silicon and found ($\beta = 1.0 \pm 0.1$) [88]. Also in this study, the large value of β was attributed to bad vacuum conditions during film growth by the authors.

An *ex-situ* STM-study of poly(*o*-toluidine) films deposited electrochemically on polyfaceted Au single crystal spheres was carried out by Ocón *et al.* [5]. They obtained $\beta = 0.73$ but did not provide a concise explanation for this large value.

For homoepitaxy of Si/Si(111), Lanczycki *et al.* obtained $\beta = 0.67 \ldots 0.77$ at a substrate temperature of $T_{Sub} = 360°$C [87]. All other substrate temperatures above and below this temperature resulted in smaller values of β. However, in this study the large value of β could be correlated directly with the growth of isolated pyramidal features on the surface.

König *et al.* reported $\beta = 0.81$ for gold deposition on Ti-buffer layers [90].

Only recently, Schlomka *et al.* published a study of NiMnSb deposited on MgO(100), employing *in situ* x-ray reflectivity and x-ray diffuse scattering [89]. Depending on the substrate temperature during deposition they found $\beta = 0.6$ for $T_{Sub} = 150°C$ and $T_{Sub} = 250°$C, and $\beta = 0.75$ for $T_{Sub} = 300°$. They explained their data by thermally activated crystallization.

To summarize, a growth exponent $\beta > 0.5$ has been observed in various systems investigated by a bunch of methods. The origin of such a large value was speculative and no general mechanism has been identified yet. Bad vacuum conditions seem to be a plausible argument for $\beta > 0.5$. In other

systems, the formation of pyramidal features or facetting clearly excludes a self-affine surface morphology following kinetic roughening mechanisms. However, for the system DIP/SiO_2, neither bad vacuum conditions nor the formation of pyramidal features nor facetting apply as an explanation of $\beta = 0.648$.

8.4.2 Studies on organic thin films

Besides the two studies on polymer thin films by Ocón *et al.* (Ref. [5]) and Collins *et al.* (Ref. [4]) which have already been discussed above, there are only few other studies concerning the determination of scaling exponents of organic thin films.

Gibaud *et al.* examined a Langmuir-Blodgett (LB) film of 8 bilayers of cadmium substituted tricosenoic acid by diffuse x-ray scattering [6]. Analyzing the line-shape and the FWHM of rocking scans over the Bragg-reflections as a function of q_z they solely determined the roughness exponent $\alpha = 0.5$.

A scanning force microscopy study on thin films of $D = 100$ nm of the rodlike conjugated sexithienyl deposited under high vacuum conditions at rates $0.2 \ldots 1$ Å/s has been performed by Biscarini *et al.* [7]. Depending on the substrate temperature they obtained a roughness exponent $0.7 \leq \alpha \leq 1$. This is very close to the roughness exponent observed for DIP in the present thesis.

Polymer-films (linear poly(*p*-xylylene)) of various thickness deposited at rates $1.95\,\mathrm{nm/min} \leq \mathrm{R} \leq 13.9\,\mathrm{nm/min}$ in vacuum (in the order of 1 mbar) were investigated by Zhao *et al.* employing AFM-measurements [79]. They obtained the scaling exponents, $\alpha = 0.72 \pm 0.05$, $\beta = 0.25 \pm 0.03$, and $1/z = 0.31 \pm 0.02$. These findings were interpreted as a result of monomer bulk diffusion and the authors claimed the discovery of a 'new universality class' that has not been discussed previously.

To summarize, there exist only few studies concerning the determination of scaling exponents of organic thin films. The investigated thin films divide into three main classes of organic thin films: (i) polymers (Refs. [4, 5, 79]), (ii) LB-films (Ref. [6]), and (iii) 'small molecules' deposited under (U)HV conditions (Ref. [7]). Moreover, both scaling exponents α and β are independently determined at the same time only in the three studies carried out on polymer thin films. The reported results cover a large range of values for α and β which was already observed in studies of inorganic thin films. Without comparable, well-defined deposition conditions in a clean deposition environment (i.e., UHV) it is impossible to compare the individual results and draw comprehensive conclusions for this class of 'soft' materials.

Now, possible mechanisms leading to the observed scaling exponents for the growth of DIP-thin films are discussed.

8.4.3 Interpretation of the DIP-data

In contrast to most of the reviewed studies, the data for DIP presented in this thesis fulfill the desirable conditions of (a) well-defined deposition conditions in UHV, (b) the independent determination of the scaling exponents α, β, and $1/z$ with (c) complementary methods.

At present, the only model which is consistent with the scaling exponents measured in this work involves spatial inhomogeneities in the local growth rate, which are fixed during the growth process. It is plausible that when certain regions of the surface persistently grow faster than others, the surface will roughen very rapidly. The quantitative analysis [91] shows that the roughness and the correlation length grow subballistically as $\sigma \sim t/(\ln(t))^{\phi}$, $\xi \sim t/(\ln(t))^{\psi}$, where $\phi, \psi \approx 2 - 3$. Thus asymptotically $\beta = 1/z = 1$, but the logarithmic factor implies that smaller effective exponents are measured. The roughness exponent $\alpha = 1$ asymptotically, but again, smaller effective

values are usually observed. For example, for the one-dimensional models studied in [91], effective exponents $\beta = 0.7 - 0.8$ and $\alpha \approx 0.8$ were obtained. The local slope of the surface varies logarithmically with time, which is also consistent with the small steepening exponent found for the DIP films.

The nature of the present system suggests that the spatial inhomogeneities may be related to the tilt domains of the film as sketched in Fig. 8.2. In analogy with the epitaxial growth of inorganic films, one expects the formation of two-dimensional islands during the growth of the first monolayer [78]. The orientation of the molecules is presumably fixed within each island, but different islands chose different in-plane orientations of the tilt vector. If the resulting two-dimensional grain boundaries which form during the coalescence of the first layer propagate to the subsequent layers, they could give rise to the required lateral inhomogeneities. Clearly a better understanding of the early stages of growth is needed to support or refute this picture.

8.5 Conclusions

In conclusion, the three scaling exponents α, β and $1/z$ have been independently determined for highly ordered thin films of the organic semiconductor DIP deposited onto silicon-dioxide substrates under UHV-conditions employing NC-AFM, specular x-ray reflectivity and diffuse x-ray scattering in rocking scan geometry. Whereas the measured roughness exponent α is similar to that observed in many other growth experiments [3], the large values of β and $1/z$ show that DIP films belong to a class of systems which display the (largely unexplained) phenomenon of rapid roughening. It has to be emphasized that these large values have been determined independently of each other, and that the growth exponent β is constant over a large range of film thickness ($69\,\text{Å} \leq D \leq 9000\,\text{Å}$). This behavior has tentatively be attributed

to lateral inhomogeneities, which could be associated with the orientational degrees of freedom of the DIP molecules. Further work is required to test this hypothesis. Interestingly, also for most of the other systems with $\beta > 0.5$ described above (Sec. 8.4.1), the occurence of lateral inhomogeneities in the local growth rate can *not* be excluded. This may open up a reinterpretation of these data on a microscopic level.

Chapter 9

The Metal-Organic Heterosystem Gold on DIP

9.1 Introduction

In addition to high charge-carrier mobilities in the organic layer, the proper function of the contact between the metal and the organic layer is of great importance for the device performance. Thus, knowledge of the associated morphology of the metal-organic interface as well as its thermal stability is essential. Until now, there have been only a few studies conducted on metal-organic interfaces, most of which dealt with disordered polymers used as low dielectric constant material in conventional microelectronic fabrication processes [9–11]; other studies dealt with Langmuir Blodgett films [12], still others investigated UHV-deposited organic thin films [13].

DIP was chosen as the organic material for the present study, since the surface of the DIP films exhibits large terraces (up to several 100 nm) with monomolecular steps with a height of ≈ 16.5 Å. Thus, DIP films are very well-defined and ideally suited for the study of the interfacial structure of metal contacts on organic thin films. Moreover, DIP exhibits excellent crystalline

order (as shown in Sec. 7.2 and in Ref. [67]) and good charge transport properties associated with it [1,92]. Gold is widely used for contacting organic electronic devices and rather inert, hence specific chemical interactions are expected to play only a minor role. This makes it possible to focus on the role of substrate temperature and deposition rate on the morphology of the metal-organic interface.

In this chapter the interface between gold and DIP thin films as a model system for metal-contacts on organic electronic devices is investigated. First, the necessary preparation conditions which lead to a well-defined Au/DIP interface immediately after deposition by cross-sectional TEM are examined. Next, the thermal stability of the DIP thin film in this heterosystem at elevated temperatures and its desorption mechanism is investigated by *in situ* x-ray-scattering. To elucidate the crystallographic changes in the model contact at these elevated temperatures, the gold film is investigated using *in situ* x-ray scattering. Finally, the thermal stability of the metal-organic interface is studied employing *in situ* high-resolution Rutherford backscattering spectrometry (RBS) as a function of temperature. The annealing studies are particularly important to address the issue of thermal stability of devices operating at elevated temperatures. At the end of the chapter the results are discussed and summarized.

9.2 Experimental

Based on a comparison with previous experiments and Monte Carlo simulations of metals on polymers [9–11, 93, 94], one may expect the largest differences in interfacial morphology for metal deposition on crystalline organic films in the as-grown state for the two following extreme growth conditions:

1. low substrate temperature combined with a high deposition rate (sample A1);

2. high substrate temperature combined with a small deposition rate (sample A4).

Although there are important differences between disordered polymer films and crystalline films of comparatively small molecules with respect to the diffusion channels of metals into these films, here the above extreme cases have been used as a starting point.

Therefore, two samples were prepared (denoted as sample A1 and A4; see Table 9.1) under the above-mentioned differing growth conditions to investigate the interfacial morphology in the as-grown state by cross-sectional TEM. To further examine which of the parameters – temperature on the one hand and deposition rate on the other – plays the predominant role for the quality of the metal-organic interface, two other samples were also prepared (denoted as A2 and A3; see Table 9.1)) employing

1. a low substrate temperature combined with a low deposition rate (A2);

2. a high substrate temperature combined with a high deposition rate (A3).

These samples (A1 to A4) were examined by cross-sectional TEM as well as in temperature dependent x-ray scattering studies.

The thermal stability of the Au/DIP interface as probed by RBS will be discussed using sample A5 (Table 9.1). In addition to the samples discussed here, others were studied in complementary experiments, confirming the conclusions presented in this chapter.

All samples were prepared on smooth oxidized (4000 Å) Si(100) substrates. A DIP-layer of typically 400 Å in thickness was grown at a substrate temperature of 145 ± 5°C and at a rate of (12 ± 3) Å/min under UHV-conditions. The gold film was deposited after growth of the DIP film in the same chamber. The deposition conditions for the gold layer on top of

the DIP film are shown in Table 9.1. For a detailed characterization of this multilayer structure, TEM micrographs were taken with a JEOL FX4000 and with a Philips CM200 microscope at 400 kV and 200 kV, respectively. X-ray-measurements were carried out at beamline W1 at HASYLAB with a wavelength of $\lambda = 1.39$ Å. The RBS data were taken at the Stuttgart Pelletron with He^+-ions at 1.3 MeV and a scattering angle of $\theta = 75°$. A high energy resolution spectrometer was used with an energy resolution of $\Delta E = 2.4$ keV, corresponding to a depth resolution of ≈ 10 Å in gold. For the temperature dependent measurements, the samples were mounted on a heater in vacuum, annealed to a given temperature for one hour each[1], and measured *in situ* using x-ray-reflectivity and RBS, respectively, at each temperature step. Note, that samples A1 and A2 were investigated in a different Synchrotron run than samples A3 and A4. The observed differences in thermal stability of the DIP-layer between samples A1 and A2 on the one hand and A3 and A4 on the other hand are due to the precision in absolute temperature measurements of only $\approx 5 \ldots 7°$C. This is evidenced by a sample which was prepared equivalently to A1 and which was measured in the same run as sample A3 and A4 [95].

9.3 Characterization of the 'as grown' State

The interfacial morphology of the samples immediately after deposition ('as grown') was characterized by cross-sectional TEM as well as by specular and offset x-ray measurements with $\Delta\omega = \pm 0.03°$ offset from the specular condition in the offset-scans. The latter value is about twice the rocking

[1]The temperature of $T = 180°$C was applied to sample A1 and A2 for ≈ 15 minutes only; this was the period in which the x-ray reflectivity and the specular DIP(001) reflection were measured. After a significant decrease in intensity at the DIP(001) reflection was noticed, the temperature was set back to room temperature.

sample	T_{Sub}	rate	nominal thickness	methods
	°C	Å/min	Å	
A1	-120	23	120	:
A2	-120	0.35	120	TEM
A3	+70	23	135	X-rays
A4	+70	0.35	135	:
A5	+25	1	70	RBS

Table 9.1: Preparation conditions of the gold layer on top of the DIP film.

width of the DIP(001) reflection (0.013°) and thus offset from the specular contribution of the DIP-film.

9.3.1 Cross-sectional TEM

Fig. 9.1 shows the cross-sectional TEM images for the samples A1 to A4 'as grown'. Large differences are clearly visible for the interfacial morphology in the TEM images depending on the preparation conditions. The images suggest that the temperature of the sample during deposition has the predominant influence on the interface morphology. Low temperature during gold deposition leads to relatively well-defined interfaces with only a small amount of interdiffusion[2], essentially independent of the deposition rate, R, within the inspected range.

High temperature during gold deposition causes a much higher degree

[2]Due to the difficulties in the preparation of high-quality TEM-samples, the TEM image of sample A2 (Fig. 9.1(b)) looks a little bit different than the other TEM-images. In fact, only one good TEM-sample was obtained for A2 which also showed large areas where the metal-organic interface has been destroyed throughout the preparation process. Nevertheless, the displayed image with the well-defined interface is thought to be representative for the sample since also the specular x-ray scattering data can be associated with a well-defined interface.

of interdiffusion of gold into the DIP-layer. The interfacial morphology of the high temperature samples exhibits a certain dependence on R. Here, a high deposition rate leads to a fairly well-defined metal-organic interface (Fig. 9.1(c)) although the quality of this interface is lower than for the low temperature samples (this will be shown in the following subsection). A low deposition rate in combination with high temperature on the other hand results in complete intermixing of gold and DIP.

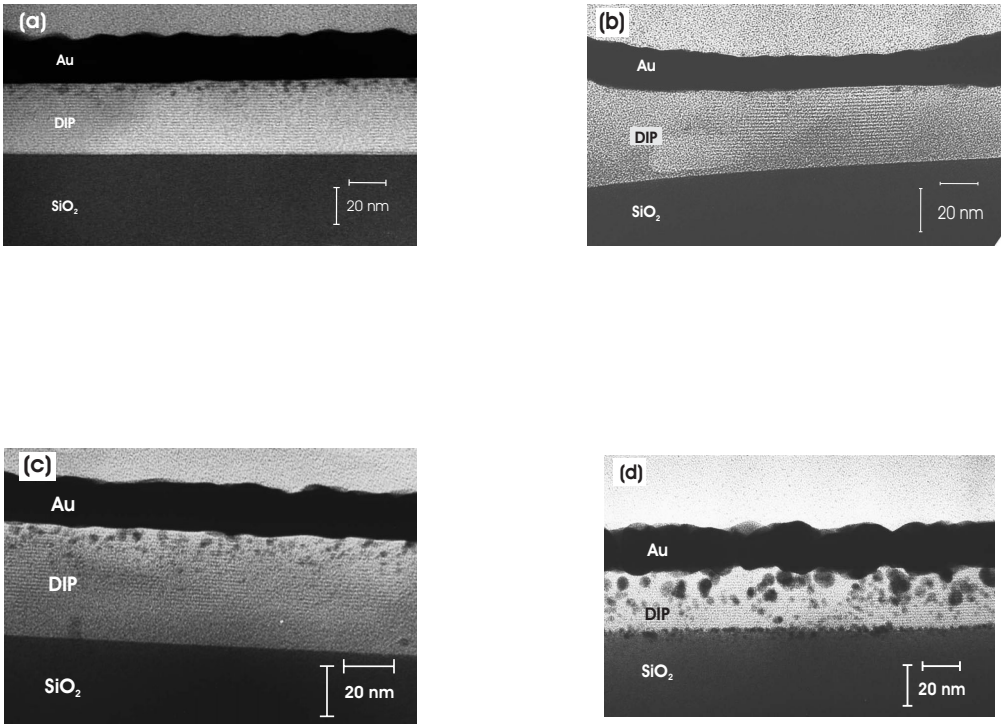

Figure 9.1: Cross sectional TEM-images of the samples (a) A1, (b) A2, (c) A3, and (d) A4.

9.3.2 Specular and diffuse offset x-ray scattering

The distinction between 'low temperature samples' on the one hand and 'high temperature samples' on the other is also supported by the x-ray data (Fig. 9.2). The low temperature samples A1 and A2 display Kiessig fringes with different periodicities associated with the thicknesses of both the gold and the DIP layer. This is evidence for rather homogeneous and well-defined films. Moreover, the offset-scans display essentially undamped Kiessig fringes with a periodicity corresponding to the gold layer thickness. Due to the broad specular width of the gold-layer (in the order of degrees) the offset-scan essentially probes the *specularly reflected intensity* of the Au-film. Thus, this observation is indicative of a markedly smooth gold film with essentially uniform thickness.

On the other hand, for the high temperature samples (strongly damped) Kiessig-fringes are visible only for sample A3. They are damped out after $2 \ldots 3$ periods ($q_z \approx 0.15$ Å^{-1}). Furthermore, also the Kiessig-fringes corresponding to the gold-film in the offset-scan are quickly damped out. For sample A4 Kiessig-fringes are completely absent. These observations support the idea of a rather rough and inhomogeneous interfacial morphology as was seen already in the TEM-images. Moreover, the essential absent Kiessig-fringes for the gold-layer in the offset-scans suggest a fairly high roughness of the Au-layer, i.e., a laterally inhomogeneous thickness.

Note, that the specular and offset-scan intensity are very close to each other. This is due to the largely different widths of the specular components of the DIP-film and the gold-layer, respectively, and it is enhanced due to the large electron-density contrast between the gold and the DIP (in the order of a factor of five). The present sample structure consists of a DIP-film with a small electron-density (i.e., a small scattering cross-section) in combination with a very narrow specular component ($\Delta\omega \approx 0.015°$) and a gold-film with a large electron-density (i.e., a large scattering cross-section)

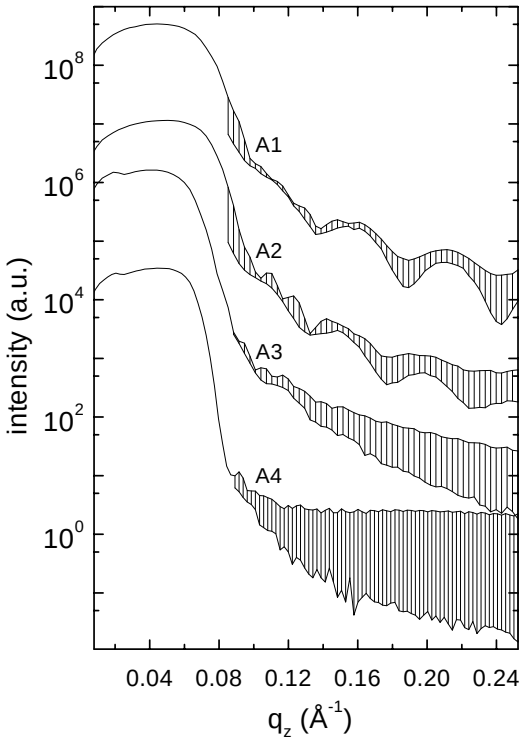

Figure 9.2: Reflectivity and offset-scans for the samples A1 ... A4. The individual data-sets are offset to each other for the sake of clarity.

in combination with a very broad specular component ($\Delta\omega$ = some degrees). This is displayed in Fig. 9.3, where rocking scans at various positions of q_z show the scattering contributions of the DIP (narrow specular component) and of the gold (broad component, almost plateau-like), respectively, for sample A1. Thus, the standard formalism of subtracting an offset-scan from the specular-scan to obtain the 'true' specular intensity fails. Generally, the sketched problem will make it difficult to fit the data with the simple Parratt-

formalism or a semi-kinematic formalism. Rather, it would be necessary to fit the diffuse and the specular intensity simultaneously. Nevertheless, the periodicty of the Kiessig-fringes still allows for a fairly precise estimate of the corresponding film thicknesses, and the degree of damping of the Kiessig-fringes provides at least an indication for the quantity of interfacial roughness.

9.4 Characterization of the Annealing Process: DIP Film

To address the thermal stability of the DIP-film in this heterosystem, the samples were annealed as described in Sec. 9.2. During the annealing *in situ* x-ray measurements of the reflectivity as well as of the DIP(001) reflection were carried out. To compare the intensities of the DIP(001) reflections the integrated peak intensities were normalized to the x-ray intensity at $2\Theta = 0.45^\circ < 2\Theta_c$ (i.e., the x-rays are totally reflected by the gold film) and set to 1 for the measurement in the 'as grown' state. The coherent thickness of the DIP-film was determined by analyzing the position of the minima between the Laue-oscillations around the DIP(001) reflection according to the Laue-function (Eq. 7.20)

$$I \propto \left(\frac{\sin(\frac{N q_z d_{DIP}}{2})}{\sin(\frac{q_z d_{DIP}}{2})} \right)^2 , \tag{9.1}$$

where N is the number of (coherently scattering) monolayers in the film.

9.4.1 Low temperature samples

Comparing the periodicity of the Kiessig-fringes close to the critical angle with the periodicity of the Laue-oscillations around the DIP(001) reflection shows that the DIP-film of the low temperature samples is still well-defined

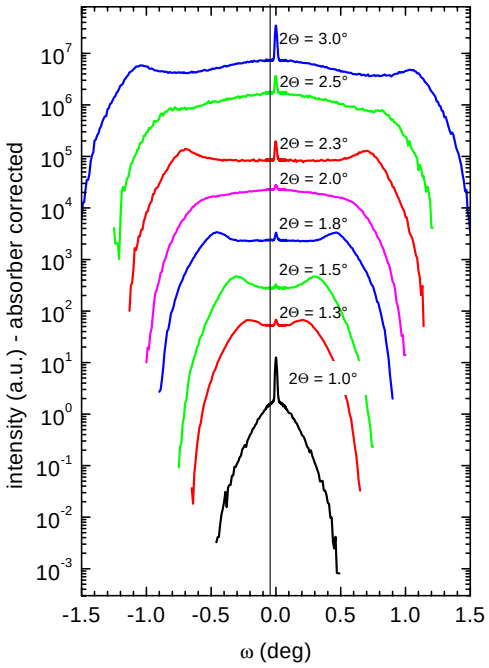

Figure 9.3: Typical set of rocking scans for the system Au/DIP at 8 different positions of 2Θ for sample A1. The vertical line indicates the position where the offset-scans of Fig. 9.2 were taken. It should be pointed out that the set shown above was found for all samples in a very similar manner and that it did not change upon annealing as long as the DIP-layer was stable ($T \lesssim 160°$C).

and coherently ordered across its entire thickness after Au-deposition. Almost undamped Laue-oscillations are evidence for a high degree of homogeneity of the DIP film (Figs. 9.4 (a) and (b)).

Fig. 9.5 shows the thermal behavior of sample A2 which is representative

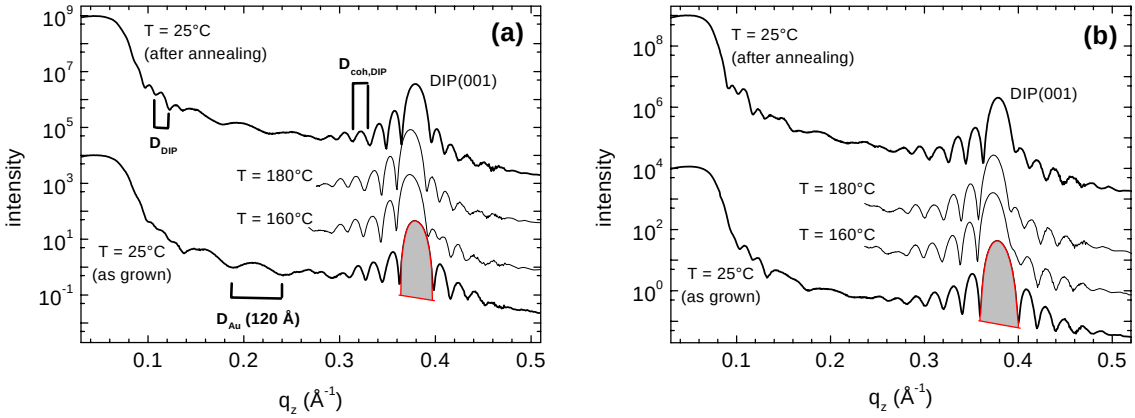

Figure 9.4: DIP(001) reflection of samples A1 (a) and sample A2 (b) at various annealing temperatures. The different scans are offset to each other for clarity. For the samples in the as-grown state and at room temperature after annealing the x-ray-reflectivity data are also plotted.

for all investigated low temperature samples. The intensity of the specular DIP(001) reflection as well as the coherent thickness $D_{coh,DIP}$ of the DIP-film as a function of temperature are displayed.

Up to $T \approx 160°C$ the intensity of the Bragg reflection is essentially stable. This implies a high degree of thermal stability of the DIP layer and is the same temperature as for uncapped DIP-films. The coherent thickness $D_{coh,DIP}$ of the DIP-film remains essentially constant (increase by one monolayer), while the intensity increases by $\approx 20\%$ for sample A2 (and by $\approx 40\%$ for sample A1). The latter observation is indicative of a reordering process in the DIP-film taking place at elevated temperatures.

For $T \geq 160°C$ the intensity of the Bragg reflection decreases while the coherent thickness remains essentially constant (an increase of 3 monolayers DIP compared to the 'as grown' state). Also, the DIP-film thickness does not change during the annealing as probed by the Kiessig-fringes (dotted hori-

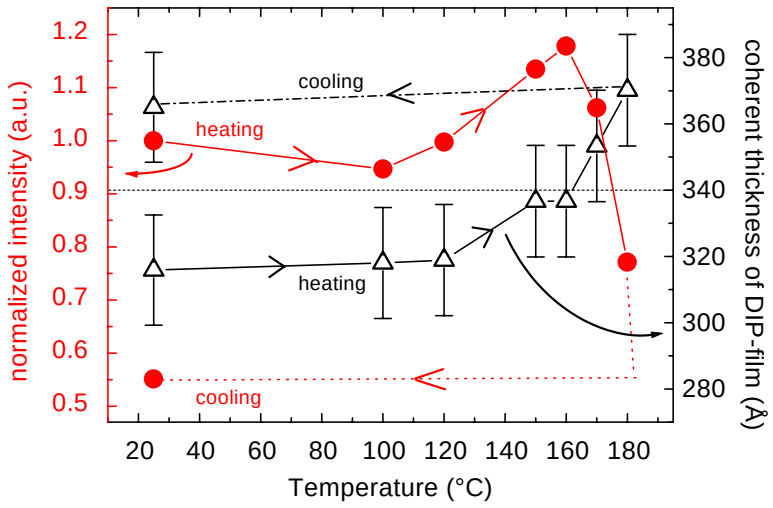

Figure 9.5: Normalized intensity (filled circles) of the DIP(001) reflection of sample A2 (shaded area in Figs. 9.4 (a) and (b)) and coherent thickness, $D_{coh,DIP}$, of the DIP-film (open triangles) as a function of the annealing temperature. The dotted horizontal line reflects the essentially unchanged thickness of the DIP-film, D_{DIP}, as obtained by the Kiessig-fringes.

zontal line in Fig. 9.5). The rocking width of the DIP(001) reflection remains stable throughout the entire annealing procedure. Given that the intensity distribution between the higher order DIP reflection does not change significantly it is unlikely that structural changes cause the intensity decrease. Rather, these observations suggest a laterally inhomogeneous desorption process.

Figure 9.6 displays a cross-sectional TEM-image of a sample prepared similarly to sample A1 after annealing. This sample was investigated in a different series of measurements. It was held at $T = 170 \pm 5$°C until the DIP(001) reflection had decreased to 5% of its original value. At this stage,

the Kiessig-fringes associated with the DIP-layer had vanished. However, the Laue-oscillations around the DIP(001) reflection were still present with essentially the same periodicity compared to the 'as grown' state, thus providing the same coherent thickness of the remaining DIP as of the DIP layer after sample preparation [95]. The TEM-image shows a closed gold layer which is interrupted at some points. The curved edges at the interruption indicate that some material in the void was destroyed during preparation of the TEM-sample (interruption of the gold layer due to TEM-sample preparation usually results in 'sharp' edges). It is plausible to assume that the empty space was filled by a DIP-island prior to TEM-preparation. This scenario matches the model of a laterally inhomogeneous desorption process outlined above.

9.4.2 High temperature samples

A comparison of the periodicity of the Kiessig-fringes with the periodicity of the Laue-oscillations around the DIP(001) reflection shows that the DIP-film of the high temperature samples is still well-defined and coherently ordered across its entire thickness (Figs. 9.7 (a) and (b))[3]. However, the Laue-oscillations around the DIP(001) Bragg reflection are considerably damped. This is evidence for an appreciably inhomogeneous DIP-film. It is plausible to attribute this observation to the interdiffusion of considerable amounts of gold diffused into the DIP-film during deposition which leads to destruction of parts (A3) or large areas (A4) of the DIP-film as was already observed in the TEM images (Fig. 9.1 (c) and (d)).

Fig. 9.8 shows the thermal behavior of sample A3. It is representative for all high temperature samples which were investigated. The intensity of the

[3]Sample A4 does not exhibit Kiessig-fringes. Thus, the statement about the DIP-film thickness was made from the values determined during the DIP-deposition by the quartz-microbalance and from the thickness observed in the TEM image of the film, respectively.

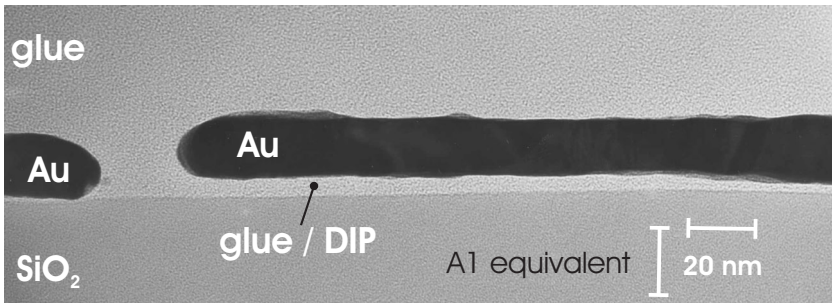

Figure 9.6: Cross sectional TEM-micrograph that shows a sample prepared like A1. The gold layer is separated from the SiO_2 – substrate only by a small organic layer. In lateral direction the gold film exhibits holes with curved edges where presumably DIP islands resisted the thermal treatment.

specular DIP(001) reflection as well as the coherent thickness $D_{coh,DIP}$ of the DIP-film as a function of temperature are displayed.

A closer look to the data shows that samples A3 and A4 essentially exhibit the same thermal stability ($T \approx 150°C$) as the low temperature samples A1 and A2. The deviation in temperature of 10°C is thought to be caused by the experimental setup.

For still higher temperatures, A3 and A4 exhibit a pronounced decrease of the intensity of the DIP(001) reflection while at the same time its rocking width and D_{coh} remain constant. This suggests a laterally inhomogeneous desorption process similar to that of the low temperature samples. However, in contrast to the low temperature samples, at temperatures below

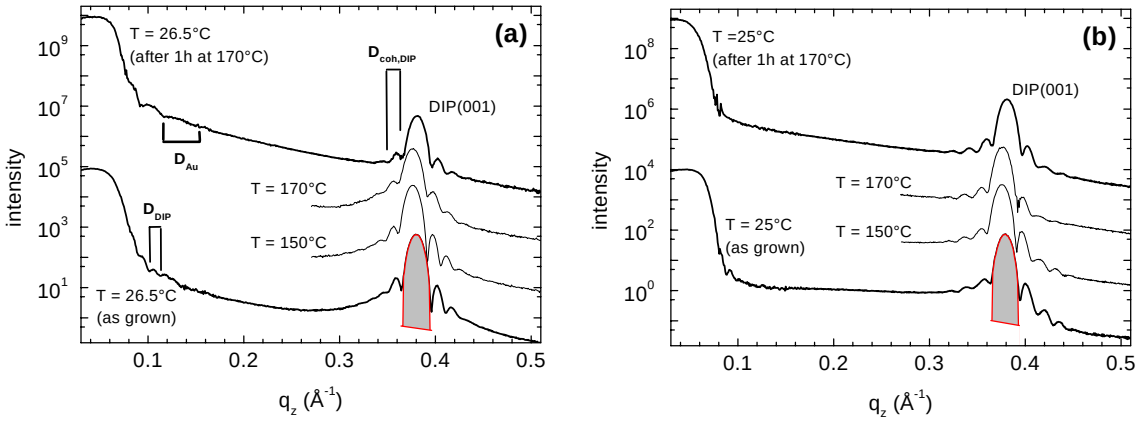

Figure 9.7: DIP(001) reflection of sample A3 (a) and of sample A4 (b) for different annealing temperatures. The different scans are offset to each other for clarity. For the samples in the as-grown state and at room temperature after annealing the x-ray-reflectivity data are also plotted.

onset of desorption the intensity of the DIP(001) reflection remains essentially constant within the experimental error. Thus, no reordering process in the DIP-layer is observed for A3 and A4.

9.5 Characterization of the Annealing Process: Au Film

To characterize the gold layer on top of the DIP-film, Bragg-scattering was used. This allows for the determination of the crystalline orientation of the grains in the gold film with respect to the surface normal. Intensities were determined as the area of a Gaussian fitted to the specular Au(111) reflection. The presented data of all samples were normalized in the same way, thus the intensities of the Au(111) reflection of the various samples could be

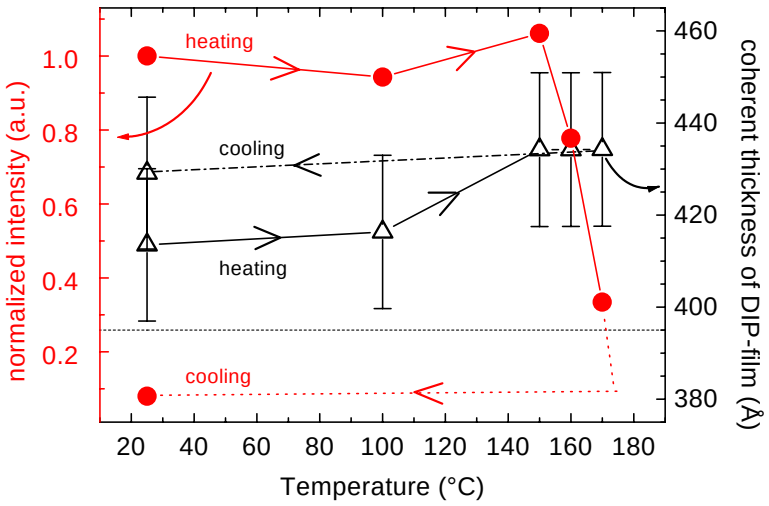

Figure 9.8: Normalized intensity (filled circles) of the DIP(001) reflection of sample A3 (shaded area in Figs. 9.7 (a) and (b)) and coherent thickness, $D_{coh,DIP}$, of the DIP-film (open triangles) as a function of the annealing temperature. The dotted horizontal line reflects the essentially unchanged thickness of the DIP-film, D_{DIP}, as obtained by the Kiessig-fringes.

compared quantitatively. The coherent thickness of the gold grains, $D_{coh,Au}$ was obtained by analyzing the peak width of the Au(111) reflection and its Laue-oscillations according to the Laue-function as described above (Eq. 9.1).

By employing rocking scans at the q_z-position of the Au(111) Bragg-reflection, the mosaicity ($\Delta\Theta$ = FWHM)) of the gold grains with (111)-orientation along the surface normal is probed.

9.5.1 Low temperature samples

Fig. 9.9 (a) shows examples for the specular scan over the Au(111) Bragg reflection 'as grown' and after the annealing procedure, while Fig. 9.9 (b)

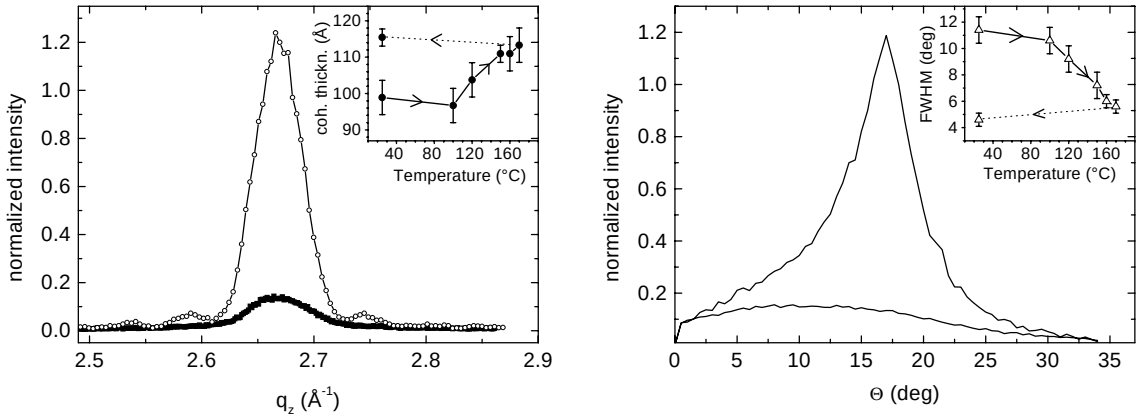

Figure 9.9: (a) Specular scan through the Au(111) Bragg reflection of sample A1'as grown' and after the annealing procedure. The inset displays the coherent thickness of the gold grains as derived from fits with the Laue-function. (b) Rocking scan across the specular Au(111) Bragg reflection of sample A1 'as grown' and after the annealing procedure. The inset shows the FWHM of the rocking width, which is an indicator for the angular distribution (mosaicity) of the gold grains in the film.

displays the corresponding rocking scans at the q_z-position of this peak. Figs. 9.10 (a) and (b) display the evolution of the intensity of the Au(111) reflection and of the FWHM of the rocking peak as a function of temperature for samples A1 and A2, respectively. In the 'as grown' state, the intensity of the Bragg-reflection is fairly low but essentially the same for both samples. At the same time, the mosaicity of the gold grains with (111)-orientation along the surface normal is relatively high (of the order of 10°). However, given that in this system Au is evaporated onto an organic film it may be considered as remarkable that obviously a preferred orientation forms rather than a polycrystalline film.

The behavior of the gold layer upon the subsequent annealing is similar

for both samples A1 and A2.

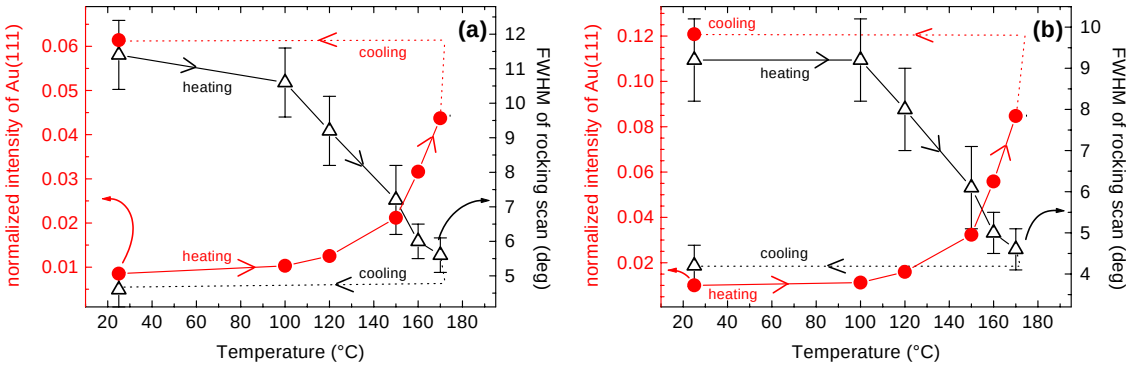

Figure 9.10: Intensity of the specular Au(111) reflection (red closed circles, left axis) and its rocking width, i.e., mosaicity, (black open triangles, right axis) for (a) sample A1, and (b) sample A2.

Up to $T = 100$°C the mosaicity as well as the peak intensity remain almost constant. Further increasing the temperature results initially in a remarkable decrease of the mosaicity, whereas the intensity of the Bragg reflection increases only slightly.

For $T > 120$°C, the intensity of the Bragg-reflection increases largely while the mosaicity of the respective grains continues to decrease.

Both processes continue as the temperature is steadily increased. At the end of the annealing procedure the intensities of the specular Au(111) Bragg reflections for samples A1 and A2 have increased by a factor of 7 and 12, respectively. The mosaicity has decreased from $\approx 10°$ to values of about $4°$ for both samples.

Now the coherent thickness of the gold layer is considered. For $T \gtrsim 100$°C, the FWHM of the Au(111) Bragg reflection of samples A1 and A2 starts to decrease and eventually exhibits pronounced Laue-oscillations for $T \approx 150$°C (Fig. 9.9 (a)). The decrease of FWHM is related to an increase in coherent

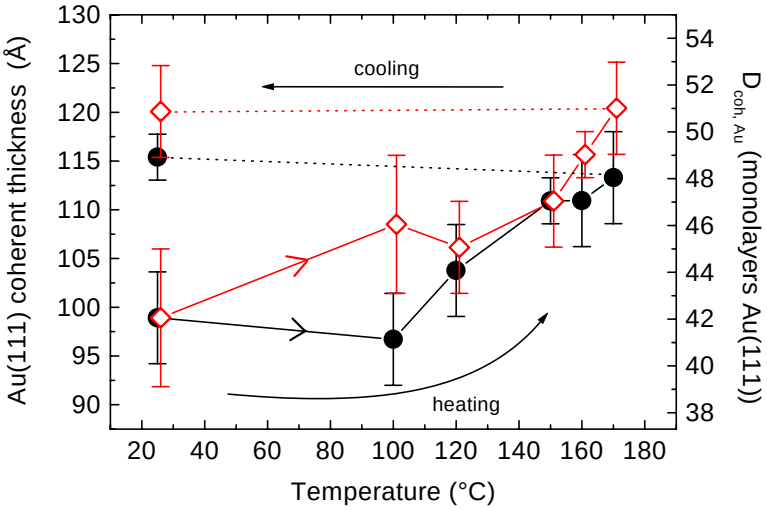

Figure 9.11: Coherent thickness of the Au(111) grains in the gold film of A1 (black closed circles) and A2 (red open diamonds).

thickness of ≈ 20Å (see Fig. 9.11 and inset of Fig. 9.9 (a)). Moreover, the appearance of Laue oscillations is evidence for the existence of well ordered gold grains ((111)-orientation) with homogeneous thickness.

Combining the observations of an increase in intensity of the Au(111) reflection, a decrease of its mosaicity and an increase in the coherent thickness of Au grains with (111)-orientation suggests the occurrence of a pronounced reordering process in the Au-layer for $T \geq 120$°C. This process leads to a preferential (111) orientation of the grains in the film along the z-axis which usually is the energetically favorable orientation for thin gold-films. Additional evidence for this interpretation is given by the continuously decreasing intensity of the non-collinear Au(200) reflection which also has been recorded with increasing temperature.

9.5.2 High temperature samples

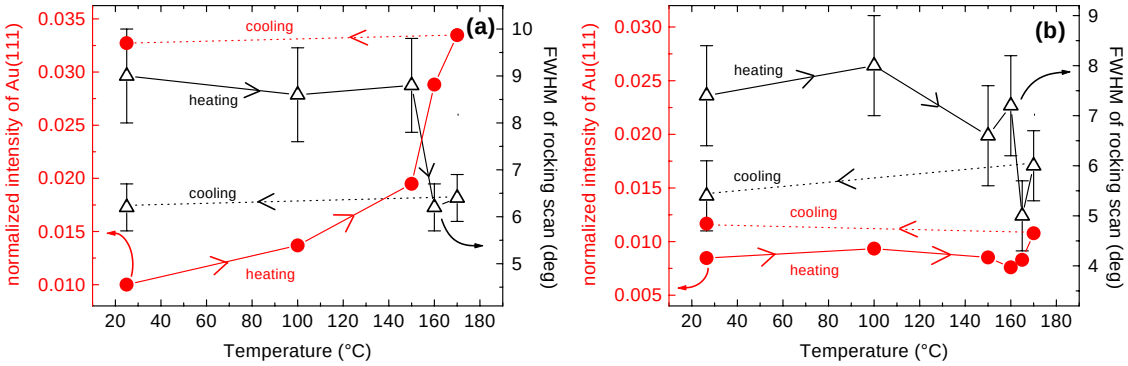

Figure 9.12: Intensity of the specular Au(111) reflection (red closed circles, left axis) and its rocking width, i.e., mosaicity, (black open triangles, right axis) for (a) sample A3, and (b) sample A4.

Figs. 9.12 (a) and (b) display the evolution of the intensity of the Au(111) reflection and of the FWHM of the rocking peak as a function of temperature for samples A3 and A4, respectively.

Remarkably, for both samples, the intensity of the specular Au(111) reflection in the 'as grown' state is essentially the same as for A1 and A2. The rocking width of the Au(111) reflection is slightly smaller for the high temperature samples than for A1 and A2 but still it is of the order of 10 degree. These findings may be seen as a result of a random process in the formation of the Au layer. Here, the number of orientated Au grains and their angular spread in the cap-layer appears to be mainly independent on the substrate temperature (within the inspected range of $-120°\mathrm{C} \leq T \leq +70°\mathrm{C}$).

Compared to the low temperature samples, the behavior of the gold layer upon annealing is somewhat different for samples A3 and A4. First, sample A3 is considered.

Up to $T = 150°C$ the mosaicity remains constant within the experimental error. At the same time, the intensity of the specular Au(111) reflection increases slightly with each temperature step.

At $T = 160°C$, the mosaicity decreases to its saturation value on the one hand. The intensity of the Au(111) reflection shows a pronounced increase which continues as the temperature is further increased indicative of a re-ordering process at the expense of Au grains with (200)-orientation. However, the intensity increases only by a factor of 3.5 compared to a factor of 7 and 12 for the low temperature samples.

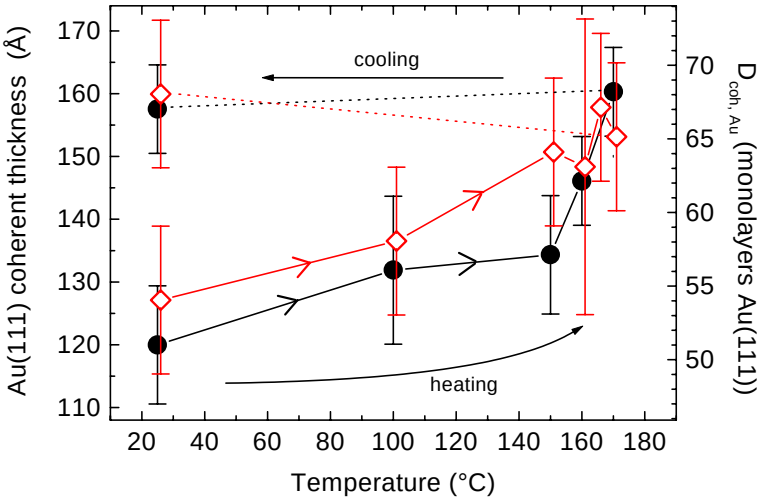

Figure 9.13: Coherent thickness of the Au(111) grains in the gold film of A3 (black closed circles) and A4 (red open diamonds).

Inspection of the coherent thickness shows a pronounced increase of $D_{coh,Au}$ of $\approx 30\%$ (see Fig. 9.13) for $T > 150°C$. However, Laue oscillations appear only after annealing at the highest temperature and are rather smeared out. This implies that the grains inside the film exhibit a fairly broad

distribution in their coherent thickness, i.e., the film shows an inhomogeneous thickness, in contrast to the observations at the low temperature samples. In conclusion, the behavior of sample A3 upon annealing resembles that of the low temperature samples although there remain differences in the crystalline homogeneity of the Au-layer.

The structural behavior of the gold layer of sample A4 upon annealing is not comparable to any of the other samples. This can be explained by the highly intermixed structure of this heterosystem, which itself is not 'well-defined' at all.

9.6 Characterization of the Annealing Process: Au/DIP Interface

At this point, the thermal stability of the Au / DIP-interface will be inspected. For this purpose, *in situ* temperature dependent high energy resolution RBS measurements were carried out on sample A5. In Fig. 9.14 the spline-fitted RBS gold peak is displayed. It was measured just after deposition and after annealing at different temperatures for one hour each. Immediately after deposition the gold peak exhibits a slightly smeared-out shape with relatively steep edges at the high and low energy side, pointing to an essentially homogeneous and well-defined film with only little interdiffusion. The simulation (gray area in Fig. 9.14) gives a film thickness of 70 Å and a thickness fluctuation of 25 Å. The latter equals to the surface roughness of the DIP film as determined by x-ray reflectivity measurements.

Although for technical reasons sample A5 could not be prepared equivalent to sample A1 or A2, the RBS data provide evidence for a well-defined interface between the gold and the DIP layer. Annealing at 100°C does not change the peak significantly, demonstrating that the interface is thermally

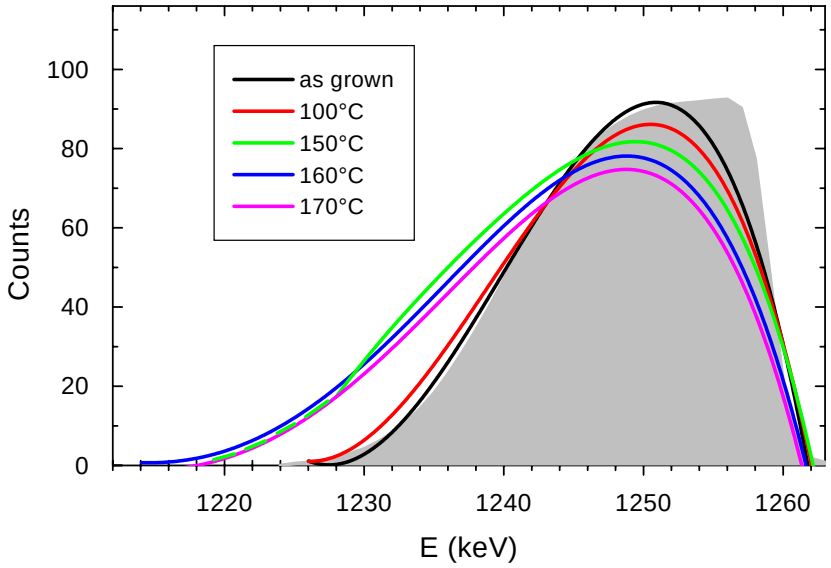

Figure 9.14: RBS-measurements around the gold edge of sample A5. The figure shows the spline-fitted RBS gold peak just after gold deposition (black), and after annealing at $T = 100$°C (red), 150°C (green), 160°C (blue), and 170°C (magenta) for one hour each. The slightly rounded edges on the high energy side are indicative of small amounts of adsorbed material on top of the gold film. For comparison the gray shaded area shows an RBS-simulation for an ideal Au film with 70 Å average thickness and 25 Å thickness fluctuation.

stable against interdiffusion. Further annealing at 150°C results in a noticeable change of the shape of the peak: the FWHM of the peak increases, and the low energy side exhibits a longer tail. This is a clear sign for interdiffusion of gold into the DIP film. Remarkably, the peak shape does not change any more upon further annealing to 160°C and 170°C, which suggests that the gold diffusion process is already completed at 150°C, most likely due to the formation of immobile gold clusters. However, at the two highest anneal-

ing temperatures, the position of the gold edge shifts to lower energies by ≈ 1 keV. This implies that the gold film is covered by a thin film (presumably DIP) of about 15 Å in thickness, indicating that at this stage wetting effects play a role.

9.7 Discussion

At first, the interfacial morphology in the 'as grown state' is discussed. TEM images as well as specular and off-specular x-ray measurements close to the critical angle show that the interfacial morphology is critically dependent on the conditions during gold deposition. Given, that for technical applications a well-defined metal-organic interface morphology is preferable it turns out that a low sample temperature during gold deposition is of greater importance than the deposition rate for the inspected range of substrate temperature and deposition rate. Low sample temperatures ($-120°$C) lead to gold layers of rather homogeneous thickness and quite well-defined interfaces although a small amount of gold interdiffusion into the organic layer seems to be unavoidable without the application of a (reactive) diffusion-barrier layer between DIP and gold. In contrast to the interfacial morphology between Au and DIP, the average crystalline orientation of the Au grains in the cap-layer appears to be largely unaffected by the substrate temperature during deposition. Comparing the intensity of the Au(111) reflection and of its rocking width shows that these quantities are nearly equal for the investigated samples. This suggests, that the formation of the Au grains in the Au film is a random process which is essentially independent of the substrate temperature and of the deposition rate in the range of rate and temperature investigated.

Now, combining the results of x-ray-scattering, RBS, and TEM measurements, a plausible scenario for the changes in the heterostructure upon

annealing is proposed (see also Fig. 9.15).

Figure 9.15: Model for the desorption process of the DIP in a system of Au/DIP. On the left side the system is shown prior to the annealing process. The image on the right hand side depicts the situation during and after the annealing step in which some DIP-islands remain unchanged in some regions.

Up to $T \approx 100°C$ the heterosystem is thermally stable (left hand side of Fig. 9.15).

For $100°C < T \lesssim 150°C$, interdiffusion of gold into the DIP film is facilitated, as is reflected by the RBS-measurements. This may cause the reordering process in the gold-film indicated by a decrease of the mosaicity of grains with Au(111) orientation parallel to the surface normal and a slight increase of the specular Au(111) intensity. In addition, a reordering process in the DIP-film is observed (increasing DIP(001) intensity). However, at this point, the DIP-film and, presumably, also the interface remain essentially stable.

At still higher temperatures ($T \gtrsim 155°C$) the DIP-film becomes thermally unstable. DIP-molecules start to desorb and enhanced gold-interdiffusion sets on, accompagnied by a pronounced reorientation of the gold film as well as by increasing coherent thickness of the gold grains. This points to a dewetting of the gold-film.

The x-ray data of the DIP-film suggest that the DIP-film exhibits a laterally inhomogeneous desorption process: the DIP-film splits into laterally separated islands of homogeneous thickness (constant D_{coh}, D_{DIP}, and DIP(001) rocking width, but decreasing intensity of the DIP(001) reflection). A TEM-

image of a sample after annealing (Fig. 9.6) supports the idea that the islands are separated by 'canyons' which presumably are filled with gold (see sketch on the right hand side of Fig. 9.15). From a technological point of view it is expected, that latest from the onset of DIP-desorption the performance of an electronic device using DIP as organic semiconductor will diminish due to the islanding effect.

It must be pointed out that the finding of a *laterally inhomogeneous* desorption process of the DIP-film in the heterosystem is contrary to the observation of a *laterally homogeneous* desorption process for uncapped DIP-films as has been demonstrated in Sec. 7.3.2. The presence of the gold-film has a large influence on the desorption behavior of the DIP-film. It is plausible to assume that stacks of DIP which are covered by a closed gold-layer resist to a higher temperature than stacks of DIP which are uncapped or can diffuse through cracks in the cap-layer. Thus, in this picture, the gold layer induces a complete change in the desorption process of the DIP-layer.

Chapter 10

Summary

In this thesis, the growth, structure, thermal expansion and desorption of thin films of diindenoperylene (DIP) deposited on SiO_2- and on Al_2O_3-substrates were studied. In addition, the properties of the metal-organic interface depending on the preparation conditions and on annealing were investigated for the heterostructure Au/DIP as a model-system for metal-organic contacts.

10.1 DIP Thin Films

10.1.1 First AFM, high-resolution x-ray-, cross-sectional TEM, and spectroscopic ellipsometry measurements on DIP thin films

High structural order with a mosaicity as small as 0.0087° has been obtained for DIP-films prepared under suitable preparation conditions ($T_{Sub} = 145°C \pm 5°C$, $R = 12 \pm 3$ Å/min) on atomically smooth SiO_2 substrates. The high degree of structural order has been observed by specular x-ray-scattering and by cross-sectional TEM-images where individual lattice-planes could be resolved. The specular x-ray data show Kiessig-fringes and DIP

Bragg-reflections up to the 9th order with Laue-satellites, and a lattice spacing of $d_{DIP} \approx 16.5$ Å has been determined. A comparison of the oscillation period of the Kiessig-fringes and the Laue-oscillations demonstrates that the DIP-films are coherently ordered across their entire thickness ($D_{DIP} = D_{coh,DIP}$). AFM images show large terraces with a lateral extension up to several 100 nm separated from each other by monomolecular steps of 16.5 Å. In addition, ellipsometry-measurements showed an optical band-gap of $E_{g,\,opt.} = 2.2 \pm 0.1$ eV.

10.1.2 Structure of DIP-films

Analysis of the complete specular rod by the Master-formula

Based on kinematic scattering theory, the specular-rod data have been analyzed by fitting the x-ray-data from $q_z = 0$ up to the largest recorded value of q_z. The electron density of a given sample, $\rho_{el}(z)$, was separated into the contributions of the substrate (i.e., a constant part) and the DIP film (i.e., an oscillatory part). The latter contribution was modeled by a Fourier-series where the Fourier-amplitudes correspond to the intensities of the individual DIP Bragg-reflections and the Fourier phases could be reduced to a 'Fourier sign', '+' or '-', due to the mirror-symmetry of the DIP-molecule. This formalism allowed for a fairly good fit of the complete specular rod with only few free parameters. Thus, the oscillatory electron-density profile of the DIP-layer was obtained with high precision.

This model has been applied to a set of data recorded on samples with various film thickness ($69\,\text{Å} \leq D_{DIP} \leq 1100\,\text{Å}$). The main results of the data-analysis are

- The lattice constant d_{DIP} decreases with increasing D_{DIP} up to $D_{DIP} \approx 670$ Å where it remains constant at 16.56 ± 0.02 Å. The relative change between the largest and the smallest lattice constant, d_{DIP}, is 0.54%.

- The mean electron density of the DIP-film, ρ^0_{DIP}, increases with increasing film thickness up to $D_{DIP} \approx 400$ Å where it remains constant at 0.39 el/Å^3. The relative change between the smallest and the largest value of ρ^0_{DIP} is 22.9%. The product of $d_{DIP} \times \rho^0_{DIP}$ is not constant but increases with increasing thickness, thus suggesting a change in structure for larger film thicknesses.

- The electron-density in the DIP-film exhibits pronounced oscillations around ρ^0_{DIP} along one monolayer with a ratio (i.e., electron density contrast) of $\rho^{max}_{DIP}/\rho^{min}_{DIP}$ of up to 1.9.

Temperature dependent measurements

Knowledge about the thermal stability of DIP films about their desorption process, and about their thermal expansion is of fundamental interest. Likewise, it is technologically relevant.

These issues were addressed by annealing DIP-samples to increasing temperatures while measuring their crystallinity by specular x-ray scattering. The main results of these investigations are listed below.

- DIP-films are thermally stable up to $T = 155°\text{C} \pm 10°\text{C}$. Annealing to higher temperatures results in a laterally homogeneous desorption process (e.g., layer-by-layer) which was revealed by comparing the (decaying) intensity of the first specular DIP Bragg-reflection with the (decaying) coherent film thickness, D_{coh}, and with the (decaying) total film-thickness, D_{DIP}.

- The thermal expansion coefficient parallel to the molecular plane (i.e., normal to the surface) in the temperature-range of thermal stability is $\alpha_{\parallel} = (75.8 \pm 4.5) \cdot 10^{-6}$ 1/K. The thermal expansion coefficient normal to the molecular planes (i.e., parallel to the substrate surface) is expected

to be a factor of $2 \ldots 4$ larger than $\alpha_{\|}$, yet, no experimental data have been recorded.

- Annealing to temperatures $T \geq 160°\mathrm{C}$ results in two irreversible structural changes. The first irreversible structural-transition is observed for $160°\mathrm{C} \leq \mathrm{T} \leq 200°\mathrm{C}$. In this temperature interval, the lattice constant d_{DIP} is increasing only slowly with T and eventually saturates. Increasing the temperature further results in a second irreversible structural-transition which is indicated by a jump of d_{DIP} (corresponding to a thermal expansion coefficient of $\alpha_{\|} \approx 1100 \cdot 10^{-6}$ 1/K in this small temperature interval). In addition, a rapid increase of the desorption rate is observed for $T > 200°\mathrm{C}$.

- The desorption rate at $T = 195°\mathrm{C}$ is in the order of 1 ML/min.

In-plane structure

The in-plane structure of DIP-films deposited on SiO_2 as well as on A-plane sapphire substrates has been investigated using x-ray-scattering in GID-geometry. The main results are

- All samples exhibited Bragg-reflections at $q_{\|} \approx 1.47$ Å^{-1} ($d \approx 4.28$ Å) and at $q_{\|} \approx 1.715$ Å^{-1} ($d \approx 3.65$ Å) which could be related to the DIP-film.

- On one DIP-film deposited on A-plane sapphire even azimuthal orientation of these Bragg-reflections could be demonstrated pointing to at least 4 domains in the film. Ellipsometry measurements on this film revealed a weak azimuthal anisotropy (i.e., alignment of the molecules parallel to the substrate). This anisotropy may be due to a 'morphology induced' growth mode where the DIP molecules align along preferred

orientations of the substrate rather than exhibit an epitaxial relation with the substrate.

10.1.3 Growth Behavior and Scaling Exponents

Based on the theory of fractal scaling of the surface roughness of thin film samples, the scaling exponents α, β and $1/z$ have been determined. Two complementary techniques have been applied to determine α (NC-AFM and diffuse x-ray scattering, respectively) and the rms-roughness σ has been measured by x-ray reflectivity and NC-AFM on samples with an unusual large range of thickness ($69\,\text{Å} \leq D_{DIP} \leq 9000\,\text{Å}$) to determine β. The main results are

- $\alpha_{mean} = 0.684 \pm 0.06$, $\beta = 0.748 \pm 0.05$, and $1/z = 0.92 \pm 0.20$. The result is self-consistent because the relation $1/z = \beta/\alpha$ is fulfilled within the erorr margins.

- The growth exponent β exceeds the theoretical limit for kinetic roughening ($\beta_{RD} \leq 0.5$). At present, the only model which is consistent with this kind of 'rapid roughening' involves lateral inhomogeneities in the local growth rate. These are suggested to be related to tilt domains in the present films due to the fixed orientation of the essentially upright-standing but slightly tilted molecules in the individual islands. If the resulting two-dimensional 'grain boundaries', which form during the coalescence of the first layer, propagate to the subsequent layers, they could give rise to the required lateral inhomogeneities.

10.2 The metal-organic heterosystem Au/DIP

The proper function of the metal-organic contact in organic-electronic devices is of great importance for their performance. The former is expected to be closely related to the morphology of the metal-organic interface.

Due to their large terraces and the high structural order, DIP thin films are very suitable for the deposition of metal and the subsequent analysis of the metal-organic interface 'as grown' and upon annealing. Therefore, gold has been deposited under various conditions on crystalline DIP thin films. Following the preparation of these 'model contacts', their interfacial morphology as well as the structure of the DIP-film and of the gold-layer has been investigated. For these inspections immediately after deposition and upon annealing as a function of deposition rate and substrate temperature, the complementary techniques cross-sectional TEM, high energy-resolution RBS and specular x-ray scattering have been employed. The main results are listed below

- It has been shown that the interfacial properties of metal contacts on organic materials in the system gold on DIP are strongly determined by the preparation conditions of the gold film. Gold deposition at low substrate temperatures during deposition ($-120°$C) leads to well-defined interfaces with only a slight amount of interdiffusion. The deposition rate plays only a minor role at these low substrate temperatures but has a pronounced influence on the interfacial morphology when preparing samples at high substrate temperatures ($+70°$C). In the latter case, a low deposition rate (0.35 Å/min vs. 23 Å/min) leads to a complete intermixing of gold and DIP.

- It has been found that the interface is stable against further interdiffu-

sion up to 100°C.

- The thermal stability of the DIP-layer (up to $T = 150$°C) remains unchanged compared to uncapped DIP-films. However, further annealing to still higher temperatures results in a *laterally inhomogeneous* desorption process of the DIP-film. This is contrary to the observation of a laterally homogeneous desorption process for uncapped DIP-films.

- The gold layer immediately after deposition exhibits a fairly high mosaicity of the order of 10 degrees for all samples under investigation. Remarkably, the scattering intensity of grains with (111)-orientation along the surface normal in the 'as grown' state is essentially independent of the substrate temperature during deposition. This observation suggests, that the formation of the Au grains in the Au film is a random process. Gold films deposited at low substrate temperatures (-120°C) start to exhibit a (re-)ordering process upon annealing to $T \geq 120$°C with a preferential (111)-orientation of the gold grains parallel to the surface normal. This process is presumably driven by facilitated diffusion in the DIP-film. For gold-films deposited at high substrate temperatures ($+70$°C) only a slight (re-)ordering process is observed upon annealing at $T \geq 150$°C.

Appendix A

List of Acronyms

AFM	Atomic Force Microscopy
DIP	Diindeno(1,2,3-cd,1',2',3'-Im)perylene, $C_{32}H_{16}$
DWBA	Distorted Wave Born Approximation
erf	Error Function
ESRF	European Synchrotron Radiation Facility
	(Synchrotron source in Grenoble, France)
FWHM	Full Width at Half Maximum
GID	Grazing Incidence Diffraction
HASYLAB	Hamburg Synchrotron Laboratory
	(Synchrotron Facility in Hamburg, Germany)
HDCF	Height-Difference Correlation Function ($g(R)$)
KPZ	Growth model developed by Kardar, Parisi, and Zhang [96]
LEED	Low Energy Electron Diffraction
LN2	Liquid Nitrogen
MBE	Molecular Beam Epitaxy
ML	Monolayer
NC-AFM	Non-Contact Atomic Force Microscopy
OMBE	Organic Molecular Beam Epitaxy

PAH	Polyaromatic Hydrocarbons
PTCDA	3,4,9,10-Perylene-Tetracarboxylic Dianhydride, $C_{24}O_6H_8$
RBS	Rutherford backscattering spectrometry
RD	Random Deposition
SPM	Scanning Probe Microscopy
STM	Scanning Tunneling Microscopy
TDS	Thermal Desorption Spectroscopy
TEM	Transmission Electron Microscopy
UHV	Ultra High Vacuum
XRD	X-Ray Diffuse Scattering
XRR	X-Ray Reflectivity

Appendix B

List of Symbols

α/H	roughness exponent / 'Hurst' parameter
$\alpha_{\parallel}$, $\alpha_{\perp}$	thermal expansion coefficient in stacking direction parallel and normal to the molecular plane, respectively
α_i, α_f	angle of the incident and diffracted/reflected wave
α_i'	incident angle used in semi-kinematical theory (corrected for α_c)
α_c	critical angle (for $\alpha_i \leq \alpha_c$: total reflection)
α_t	angle of the transmitted beam
β	absorption coefficient in refractive index n
β, β_{KL}	growth exponent and its kinetic limit
Δ_{sub}, Δ_{surf}	electron density contrast substrate-film and film-vacuum
δ	dispersion in refractive index n
δ	in-plane diffraction angle ($\hat{=}2\Theta$ in GID-experiments)
ϕ	azimuthal in-plane direction relative to $Al_2O_3(300)$
ϕ_k	Fourier-phase in decomposition of electron density
ϕ	tilt-angle of the DIP-molecules with respect to the surface normal
Λ	penetration depth of the evanescent wave for $\alpha_i \leq \alpha_c$
λ	wavelength of x-ray radiation
λ	steepening-exponent in mound growth; describes the evolution

	of the slope of the mounds with increasing film thickness
μ	mass absorption coefficient
μ	charge carrier mobility
ρ	density of mass
$\rho_{el}(z)$, $\rho_{el,DIP}(z)$	electron density (of DIP) along the surface normal
ρ^0_{DIP}	mean electron density of DIP
ρ^{min}_{DIP}, ρ^{max}_{DIP}	minimum/maximum electron density in one monolayer of DIP
σ_j	roughness between layer j and $j+1$
$\sigma(L,t)$	functional (scaling-)relation of the surface roughness
	in dependence of lateral probed length-scale, L
	and deposition time, t, i.e., film thickness, D
σ_{RD}	random deposition limit for the rms-roughness
$d\sigma/d\Omega$	differential scattering cross-section in scattering experiments
2Θ	scattering angle in x-ray diffraction measurements determining
	the wave vector transfer $\mathbf{q}$
Θ_i	coverage of layer i
Θ	scattering angle of the projectile ions in RBS
θ_1, θ_2	incident and exit angle for ions in RBS
ξ	lateral cut-off or correlation length
ξ_{long}, ξ_{trans}, $\tilde{\xi}_{trans}$	longitudinal, transversal, and the projected transversal
	coherence length of the x-ray-beam
$\Delta\omega$	mosaicity of a sample
$\Delta\Omega$	solid angle of the detector
$\Delta\omega_{off}$	offset-angle in offset-scans
$A(\mathbf{q})$	scattered amplitude as a function of $\mathbf{q}$
A_{film}, $A_{Substrate}$	scattered amplitude from the film and from the substrate
A_0	amplitude of the incident plane x-ray wave
A_j	j-th Fourier-coefficient of an oscillatory electron density
$\overline{A_j}$	*effective* j-th Fourier-coefficient of an oscillatory electron density

$\mathbf{a_x}$, $\mathbf{a_y}$, $\mathbf{a_z}$	lattice vectors of a 3D-crystal, parallel to the x-, y-, and z-axis
$C(R)$	height-height correlation function
c	speed of light
D_{coh}	coherent thickness
D_j, D_{DIP}	thickness of the j-th layer and of the DIP-film
D_ζ	cross-over thickness in the determination of the growth exponent β
$d_\parallel$	in-plane lattice parameter
d_0	lattice spacing between substrate surface and the beginning of the film
d_{DIP}	lattice parameter of DIP normal to the substrate
$E(\mathbf{r})$	amplitude of the electric field at point $\mathbf{r}$
E_0, E_1	energy of the incident and scattered ions in RBS
E_{edge}	highest recorded energy for ions-scattering at a specific element ($K_{M_T}E_0$)
$E_{g,opt.}$	optical band-gap energy determined for example by ellipsometry
dE/dx	specific energy loss in matter per unit length for ions
$F(q)$	structure factor
$F(q_z)$	structure factor projected to the z-axis (in the Master formula)
$f(q)$, f', f''	atomic scattering factor and the real and imaginary part of its correction terms
$f(q_z)$	'reflectivity form factor' in the Master-formula
$G(q_z)$	term that takes into account geometrical corrections in the Master-formula
$g(R)$	height-difference correlation function (HDCF)
$h_{j,0}$	mean height of the j-th layer
$h_j(x,y)$	height of interface j at the lateral position (x,y)
I_0	intensity of the beam
I_{tot}	measured intensity

I_S, I_D	specular and diffuse scattered intensity
I_{MF}, $I_{Parratt}$	intensity computed using the Master-formula and the Parratt-formalism, respectively
K_{M_T}	kinematic factor for scattering of ions at atoms with mass M_T
$\mathbf{k_i}$, $\mathbf{k_f}$	wave vectors of the incident and diffracted/reflected beam
$k_{i,z}$, $k_{t,z}$	z-components of the incident and transmitted wave-vector
L	probed lateral length-scale in an SPM measurement
L_xL_y	illuminated area of the sample in x- and y-direction (footprint) in x-ray diffraction experiments
l_1, l_2	length of path in the sample for the projectile-ion before and after being scattered (RBS experiments)
M	number of Bragg reflections on the specular rod
M_P, M_T	mass of the projectil ion and of the target atom
m_e	mass of an electron
N	number of monolayers
N_1, N_2, N_3	number of atoms in the direction of $\mathbf{a_x}$, $\mathbf{a_y}$, and $\mathbf{a_z}$
n, $n(z)$	index of refraction (along the sample normal)
p	pressure
$q_\perp$, q_z	momentum transfer perpendicular to the sample surface
$q_\parallel$, q_x, q_y	momentum transfer parallel to the sample surface
R_0	distance between scattering center and detector
R	deposition rate
R	lateral distance from the origin or between two points
R_F	Fresnel reflectivity
R_j	wave-amplitude of the beam reflected at the interface between layer j and layer $j+1$
$\mathbf{r_n}$	atomic arrangement in the unit cell with n atoms
r_A, r_B, r_C	contributions of substrate film and film-vacuum-interface to the integral of $F(q_z)$ in the Master-formula

r_e	classical electron radius (2.8×10^{-15} m)
$S(q_\parallel, q_z)$	function to calculate the diffusely scattered intensity
$s(q_z)$	structure factor in the Master-formula
T, T_{Sub}	temperature and Substrate temperature during film deposition
t	deposition time (proportional to D_{film} for constant deposition rate R)
T_F, $T(\mathbf{k})$	Fresnel transmission coefficient
T_j,	wave-amplitude of the beam transmitted into the j-th layer
v	velocity of the projectile ions in RBS-measurements
v_j	'+' or '-' – reduced Fourier-phase in oscillatory electron density due to mirror-plane symmetry of the molecules
X_j	ratio between R_j and T_j
Z_P, Z_T	atomic number of the projectile ion and of the target atom
$\tilde{z}_j$	height fluctuation of layer j around mean height $h_{j,0}$
$1/z$	scaling exponent, which should be given by β/α and relates the correlation length ξ to the film thickness D

Appendix C

List of Samples

The last column of Table C.1 shows the methods that were used to characterize the individual samples, namely x-ray reflectivity (XRR), x-ray diffuse scattering (XRD), grazing-incidence diffraction (GID), and non-contact AFM (NC-AFM). The thermal expansion was measured in the direction perpendicular to the substrate surface exploiting the shift of the first DIP Bragg reflection in q_z as a function of temperature.

All samples 'oXYZ' were deposited on thermally grown silicon oxide (4000Å) on a Si-wafers with (100) orientation and a miscut of $\approx 0.5°$. Pairs of samples labeled with ^{1},^{2} ,^{3} were grown in one run, using a shutter in front of the substrate to yield a different thickness on each part of it.

Sample 'IPsi' was prepared on thermally grown silicon-oxide (4300Å) on a Si-wafer with (111)-orientation and a miscut of $\approx 4°$.

Samples 'IPsap1'-'IPsap3' were deposited on sapphire substrates with A-plane $(11\overline{2}0)$-orientation. The substrate of sample 'IPsap3' was annealed in air at 1500°C for 24 hours prior to deposition.

† Samples were prepared by Michael Münch at Stuttgart University.

sample	D_{DIP} (Å)	T_{Sub} (°C)	Rate (Å/min)	Measurements
o69[1]	69	⋮	⋮	⋮
o126[1]	126	⋮	⋮	⋮
o206[2]	206	⋮	⋮	XRR
o385	385	⋮	⋮	XRD
o396[2]	396	145 ± 5	12 ± 3	Braggscattering
o670[3]	670	⋮	⋮	NC-AFM (OMICRON)
o970	970	⋮	⋮	⋮
o1100[3]	1100	⋮	⋮	⋮
o9000	9000	⋮	⋮	NC-AFM (DI)
o890	890	145 ± 5	12 ± 3	XRR, Thermal Exp.
IPsi[†]	390	160	60	XRR, GID
IPsap1[†]	460	(160)	(60)	XRR, GID
IPsap2	350	150 ± 5	9 ± 2	XRR, GID, Ellips.
IPsap3	285	145 ± 5	7 ± 2	Ellips.

Table C.1: Names of the samples used in the text and their growth parameters.

List of Figures

List of Tables

Bibliography

[1] M. Münch, Ph.D. thesis, Stuttgart, 2001.

[2] A.-L. Barabási and H. E. Stanley, *Fractal Concepts in Surface Growth* (Cambridge University Press, Cambridge, 1995).

[3] J. Krim and G. Palasantzas, Int. J. Mod. Phys. B **9**, 599 (1995)
Experimental Observations of Self-Affine Scaling and Kinetic Roughening at Sub-Micron Lengthscales.

[4] G. W. Collins, S. A. Letts, E. M. Fearon, R. L. McEachern, and T. P. Bernat, Phys. Rev. Lett. **73**, 708 (1994)
Surface Roughness Scaling of Plasma Polymer Films.

[5] P. Ocón, P. Herrasti, J. Vara, L. Vazquez, R. Salvarezza, and A. Arvia, J. Phys. Chem. **98**, 2418 (1994)
Scanning Tunneling Microscopy Fractal Characterization of Poly(o-toluidine) Films Produced Electrochemically on Polyfaceted Gold Single Crystal Spheres.

[6] A. Gibaud, N. Cowlam, G. Vignaud, and T. Richardson, Phys. Rev. Lett. **74**, 3205 (1995)
Evidence of Self-Affine Rough Interfaces in a Langmuir-Blodgett Film from X-Ray Reflectometry.

[7] F. Biscarini, P. Samori, O. Greco, and R. Zamboni, Phys. Rev Lett. **78**, 2389 (1997)
Scaling Behavior of Anisotropic Organic Thin Films Grown in High Vacuum.

[8] S. K. Sinha, E. B. Sirota, S. Garoff, and H. E. Stanley, Phys. Rev. B **38**, 2297 (1988)
X-ray and Neutron Scattering from Rough Surfaces.

[9] F. Faupel, R. Willecke, and A. Thran, Mat. Sci. Eng. **R22**, 1 (1998)
Diffusion of Metals in Polymers.

[10] D. Gupta, F. Faupel, and R. Willecke, in *Diffusion in Amorphous Materials*, (The Minerals, Metals and Materials Society, Pitsburgh, 1994).

[11] R. Tromp, F. LeGoues, and P. Ho, J. Vac. Sci. Tech. A **3**, 782 (1985)
Interdiffusion at the Polyimide-Cu Interface.

[12] G. Philipp, C. Müller-Schwanneke, M. Burghard, S. Roth, and K. v. Klitzing, J. Appl. Phys. **85**, 3374 (1999)
Gold cluster formation at the interface of a gold/Langmuir-Blodgett film/gold microsandwich resulting in Coulomb charging phenomena.

[13] Y. Hirose, A. Kahn, V. Aristov, P. Soukiassian, V. Bulovic, and S. R. Forrest, Phys. Rev. B **54**, 13748 (1996)
Chemistry and electronic properties of metal-organic semiconductor interfaces: Al, Ti, In, Sn, Ag, and Au on PTCDA.

[14] S. R. Forrest, Chem. Rev. **97**, 1793 (1997)
Ultrathin Organic Films Grown by Organic Molecular Beam Deposition and Related Techniques.

[15] A. Brown, C. Jarrett, D. de Leeuw, and M. Matters, Synth. Met. **88**, 37 (1997)
Field-effect transistors made from solution processed organic semiconductors.

[16] G. Horowitz, Adv. Mat. **10**, 365 (1998)
Organic Field-Effect Transistors.

[17] A. Ullmann, J. Ficker, W. Fix, H. Rost, W. Clemens, and M. Giles, Mat. Res. Soc. Symp. Proc. **665**, C7.5.1 (2001)
High Performance Organic Field-Effect Transistors and Integrated Inverters.

[18] F. Family and T. Vicsek, J. Phys. A **18**, L75 (1985)
Scaling of the Active Zone in the Eden Process on Percolation Networks and the Ballsitic Deposition Model.

[19] J. Krug, Adv. Phys. **46**, 139 (1997)
Origins of scale invariance in growth processes.

[20] J. von Braun and G. Manz, *Patent-Nr.: 595 024: Verfahren zur Herstellung von Kondensationsprodukten des Fluoranthens* (Deutsches Reichspatentamt, Berlin, 1934).

[21] E. Clar, *Aromatische Kohlenwasserstoffe - Polycyclische Systeme* (Springer-Verlag, Berlin, 1952).

[22] E. Clar, *Polycyclic Hydrocarbons* (Academic Press, London, 1964).

[23] P. S. Leung and G. J. Safford, Carbon **8**, 527 (1970)
An Investigation of the Early Stage Graphitization Process by Neutron Inelastic Scattering.

[24] C. Moutou, A. Léger, and L. d'Hendecourt, Astron. Astrophys. **310**, 297 (1996)
Far-infrared emission of PAH molecules (14-40μm): a preparation for ISO spectroscopy.

[25] A. Lacassagne, N. P. Buu-Hoi, F. Zajdela, and G. Saint-Ruf, C. R. Acad. Sc. Paris **266**, 301 (1968)
CANCÉROLOGIE — Sur le pouvoir cancérogène de deux hydrocarbures aromatiques à sept cycles.

[26] M. S.-S. Sung and M. L. de Broglie, C. R. Acad. Sc. Paris **275**, 1307 (1972)
BIOPHYSIQUE. — Mise au point de la theéorie des régions K et L relative aux mécanismes d'action moléculaires de la carcinogenèse chimique.

[27] D. D. Morgan and D. Warshawsky, Photochem. Photobio. **25**, 39 (1977)
The Photodynamic Immobilisation of ARTEMIA SALINA Nauplii by Polycyclic Aromatic Hydrocarbons and its Relationship to Carcinogenic Activity.

[28] J. W. Flesher, J. Horn, and A. F. Lehner, J. Mol. Struct. (Theochem) **362**, 29 (1996)
Molecular modeling of carcinogenic potential in polycyclic hydrocarbons.

[29] D. Meruelo, G. Lavie, and Y. Mazur, *Patent-Nr.: 6 150 414: Compositions and Methods for Treating Viral Infections: Erteilung: 21.11.2000, Antrag: 2.11.1992* (Unitet States Patent and Trademark Office, Washington, 2000).

[30] L. J. E. Hofer and W. C. Peebles, Anal. Chem. **23**, 690 (1951)
X-Ray Diffraction Patterns of Solid Aromatic Hydrocarbons.

[31] L. J. E. Hofer and W. C. Peebles, Anal. Chem. **24**, 822 (1952)
X-Ray Diffraction Patterns of 2,4,7-Trinitrofluorenone Derivatives of Aromatic Hydrocarbons.

[32] L. J. E. Hofer, W. C. Peebles, and E. H. Bean, Bureau of Mines, Bulletin 613 **613**, 1 (1963)
X-Ray Powder Diffraction Patterns of Solid Hydrocarbons, Derivatives of Hydrocarbons, Phenols and Organic Bases.

[33] W. Frey and N. Karl, unpublished results, 2001.

[34] R. Strohmaier, J. Petersen, B. Gompf, and W. Eisenmenger, Surf. Sci **418**, 91 (1998)
A systematic STM study of planar aromatic molecules on inorganic substrates I. Submolecular image contrast.

[35] A. Hoshino, S. Isoda, and T. Kobayashi, J. Cryst. Growth **115**, 826 (1991)
Epitaxial growth of organic crystals on organic substrates - polynuclear aromatic hydrocarbons.

[36] B. Warren, *X-Ray Diffraction* (Dover Publications, New York, 1990).

[37] H. Dosch, *Critical Phenomena at Surfaces and Interfaces*, Vol. 126 of *Springer Tracts in Modern Physics* (Springer, Berlin, 1992).

[38] M. Tolan, *X-Ray Scattering from Soft-Matter Thin Films*, Vol. 148 of *Springer Tracts in Modern Physics* (Springer, Berlin, 1999).

[39] M. Born and E. Wolf, *Principles of Optics: Electromagnetic Theory of Propagation, Interference and Diffraction of Light*, 6 ed. (Cambridge University Press, Cambridge, 1999).

[40] L. G. Parratt, Physical Review **95**, 359 (1954)
Surface Studies of Solids by Total Reflection of X-Rays.

[41] L. Névot and P. Croche, Revue de Physique Appliquée **15**, 761 (1980)
Characterization Of Surfaces By Grazing X-Ray Reflection - Application To Study Of Polishing Of Some Silicate-Glasses.

[42] I. W. Hamley and J. S. Pedersen, J. Appl. Cryst. **27**, 29 (1994)
Analysis of Neutron and X-ray Reflectivity Data. I. Theory.

[43] J. S. Pedersen and I. W. Hamley, J. Appl. Cryst. **27**, 36 (1994)
Analysis of Neutron and X-ray Reflectivity Data. II. Constrained Least-Squares Methods.

[44] V. Holý, J. Kubena, I. Ohlidal, K. Lischka, and W. Plotz, Phys. Rev. B **47**, 15896 (1993)
X-Ray Reflection from Rough Layered Systems.

[45] V. Holý, C. Giannini, L. Tapfer, T. Marschner, and W. Stolz, Phys. Rev. B **55**, 9960 (1997)
Diffuse X-Ray Reflection from Multilayers with Stepped Interfaces.

[46] V. Holý, U. Pietsch, and T. Baumbach, *High-Resolution X-Ray Scattering From Thin Films and Multilayers*, Vol. 149 of *Springer Tracts in Modern Physics* (Springer, Berlin, 1999).

[47] J. Daillant and M. Alba, Rep. Prog. Phys. **63**, 1725 (2000)
High-Resolution X-Ray Scattering Measurements: I. Surfaces.

[48] J. Kasper and K. Lonsdale, *Physical and Chemical Tables*, Vol. 3 of *International Tables for X-Ray Crystallography* (Kynoch Press, Birmingham, 1985).

[49] B. Henke, E. Gullikson, and J. Davis, Atomic and Nuclear Data Tables **54**, 181 (1993)
X-ray interactions: photoabsorption, scattering, transmission, and reflection at E=50-30000 eV.

[50] WWW-Address, http://www-cxro.lbl.gov/ optical_constants .

[51] B. Nickel, W. Donner, H. Dosch, C. Detlefs, and G. Grübel, Phys. Rev. Lett. **85**, 134 (2001)
Critical Adsorption and Dimensional Crossover in Epitaxial FeCo Films.

[52] F. Schreiber, M. Gerstenberg, B. Edinger, B. Toperverg, S. Forrest, G. Scoles, and H. Dosch, Physica B **283**, 75 (2000)
Phase-Sensitive Surface X-Ray Scattering Study of a Crystalline Organic-Organic Heterostructure.

[53] R. Feidenhans'l, Surf. Sci. Rep. **10**, 105 (1989)
Surface Structure Determination by X-Ray Diffraction.

[54] I. Robinson and D. Tweet, Rep. Prog. Phys. **55**, 599 (1992)
Surface X-Ray Diffraction.

[55] W.-K. Chu, J. W. Mayer, and M.-A. Nicolet, *Backscattering Spectrometry* (Academic Press, San Diego, 1978).

[56] L. C. Feldman and J. W. Mayer, *Fundamentals of surface and thin film analysis* (North-Holland, New York, 1986).

[57] J. R. Tesmer, *Handbook of modern ion beam materials analysis* (Materials Research Society, Pittsburgh, 1995).

[58] E. Rutherford, Phil. Mag. **21**, 669 (1911)
The Scattering of α and β Particles by Matter and the Structure of the Atom.

[59] L. R. Doolittle, Nucl. Instr. Meth. B **9**, 344 (1985)
Algorithms for the Rapid Simulation of Rutherford Backscattering Spectra.

[60] L. R. Doolittle, Nucl. Instr. Meth. B **15**, 227 (1986)
A Semiautomatic Algorithm for Rutherford Backscattering Analysis.

[61] D. B. Williams and C. B. Carter, *Transmission Electron Microscopy I - Basics* (Plenum Press, New York, 1996).

[62] D. B. Williams and C. B. Carter, *Transmission Electron Microscopy III - Imaging* (Plenum Press, New York, 1996).

[63] P. J. Goodhew and F. Humphreys, *Electron Microscopy and Analysis*, 2 ed. (McGraw Hill, New York, 1988).

[64] H. D. Carstanjen, W. Decker, and H. Stoll, Z. Metallkd. **84**, 368 (1993)
The 6 MV Pelletron at Stuttgart – an Accelerator for Ions, Positrons and Electrons.

[65] H. D. Carstanjen, Nucl. Instr. Meth. B **136-138**, 1183 (1998)
Ion beam analysis with monolayer depth resolution.

[66] T. Enders, M. Rilli, and H. D. Carstanjen, Nucl. Instr. Meth. B **64**, 817 (1992)
A high-resolution electrostatic spectrometer for the investigation of near-surface layers in solids by high-resolution Rutherford backscattering with MeV ions.

[67] A. C. Dürr, F. Schreiber, M. Münch, N. Karl, B. Krause, V. Kruppa, and H. Dosch, Appl. Phys. Lett. **81**, 2276 (2002)
High structural order in thin films of the organic semiconductor diindenoperylene.

[68] R. M. A. Azzam and N. M. Bashara, *Ellipsometry and Polarized Light* (North Holland, Amsterdam, 1977).

[69] M. I. Alonso, M. Garriga, F. Alsina, and S. Piñol, Appl. Phys. Lett. **67**, 596 (1995)
Determination of the Dielectric Tensor in Anisotropic Materials.

[70] I. Hill, A. Kahn, Z. Soos, and R. Pascal, Chem. Phys. Lett. **327**, 181 (2000)
Charge-separation Energy in Films of p-conjugated Organic Molecules.

[71] K. Londsdale, Z. Kristallogr. **112**, 188 (1959)
Experimental Studies of Atomic Vibrations in Crystals and their Relationship to Thermal Expansion.

[72] S. van Smaalen, J. L. de Boer, C. Haas, and J. Kommandeur, Phys. Rev. B **31**, 3496 (1985)
Anisotropic Thermal Expansion in Crystals with Stacks of Planar Molecules, such as Tetracyanoquinodimethanide (TCQN) salts.

[73] Y. S. Touloukian, R. K. Kirby, R. E. Taylor, and P. D. Desai, *Thermal Expansion – Metallic Elements and Alloys*, Vol. 12 of *Thermophysical Properties of Matter* (IFI/Plenum, New York, 1975).

[74] B. Krause, Ph.D. thesis, Stuttgart, 2002.

[75] S. Haussühl, Z. Kristallogr. **216**, 339 (2001)
Elastic and Thermoelastic Properties of Selected Organic Crystals: Acenaphthene, Trans-Azobenzene, Benzophenone, Tolane, Trans-Stilbene, Dibenzyl, Diphenyl Sulfone, 2,2'-Biphenol, Urea, Melamine, Hexogen, Succinimide, Petaerythritol, Urotropine, Malonic Acid, Dimethyl Malonic Acid, Maleic Acid, Hippuric Acid, Aluminium Acetylacetonate, Iron Acetylacetonat, and Tetraphenyl Silicon.

[76] A. Müller, Proc. Roy. Soc. A **127**, 417 (1930)
The Crystal Structure of the Normal Paraffins at Temperatures Ranging from that of Liquid Air to the Melting Points.

[77] A. Müller, Proc. Roy. Soc. A **138**, 514 (1932)
An X-ray Investigation of Normal Paraffins Near their Melting-Points.

[78] F.-J. Meyer zu Heringdorf, M. C. Reuter, and R. M. Tromp, Nature **412**, 517 (2001)
Growth Dynamics of Pentacene Thin Films.

[79] Y.-P. Zhao, J. Fortin, G. Bonvallet, G.-C. Wang, and T.-M. Lu, Phys. Rev. Lett. **85**, 3229 (2000)
Kinetic Roughening in Polymer Film Growth by Vapor Deposition.

[80] The program to calculate $I_{diffuse}$ has been provided by V. Holý.

[81] M. Siegert and M. Plischke, Phys. Rev. E **53**, 307 (1996).

[82] H. K. Janssen, Phys. Rev. Lett. **78**, 1082 (1997).

[83] G. Lengel, R. Phaneuf, E. Williams, S. Das Sarma, W. Beard, and F. Johnson, Phys. Rev. B **60**, R8469 (1999).

[84] K. Caspersen, A. Layson, C. Stoldt, V. Fournee, P. Thiel, and J. Evans, Phys. Rev. B **65**, 193407 (2002).

[85] M. Kalff, P. Šmilauer, G. Comsa, and T. Michely, Surf. Sci. **426**, L447 (1999).

[86] K. Fang, T.-M. Lu, and G.-C. Wang, Phys. Rev. B **49**, 8331 (1994)
Roughening and Faceting in a Pb Thin Film Growing on the Pb(110) Surface.

[87] C. Lanczycki, R. Kotlyar, E. Fu, Y.-N. Yang, E. Williams, and S. Das Sarma, Phys. Rev. B **57**, 13132 (1998)
Growth of Si on the Si(111) surface.

[88] C.-H. Lee and S.-Y. Tseng, Appl. Surf. Sci. **92**, 282 (1996)
In situ X-ray reflectivity measurement of thin film growth during vacuum deposition.

[89] J.-P. Schlomka, M. Tolan, and W. Press, Appl. Phys. Lett. **76**, 2005 (2000)
In Situ Growth Study of NiMnSb Films on MgO(001) and Si(001).

[90] F. König, KFA Jülich Report **No. 3092**, (1995)
Einfluss der Herstellungsparameter auf die Oberflächenrauhigkeit dünner Goldfilme, ermittelt aus der Streuung harter Röntgenstrahlen unter streifenden Winkeln.

[91] J. Krug, Phys. Rev. Lett. **75**, 1795 (1995).

[92] N. Karl, *Charge Carrier Mobility in Organic Molecular Crystals*, *Organic Electronic Materials* (Springer, Berlin, 2001).

[93] F. K. LeGoues, B. D. Silverman, and P. S. Ho, J. Vac. Sci. Tech. A **6**, 2200 (1988)
The microstructure of metal-polyimide interfaces.

[94] B. Silverman, Macromolecules **24**, 2467 (1991)
Single-Particle Diffusion into a Disordered Matrix: Simulation of a Metal-Polymer Interface.

[95] A. C. Dürr, F. Schreiber, M. Kelsch, H. D. Carstanjen, and H. Dosch, Adv. Mat. **14**, 961 (2002)

Morphology and Thermal Stability of Metal Contacts on Crystalline Organic Thin Films.

[96] M. Kardar, G. Parisi, and Y.-C. Zhang, Phys. Rev. Lett. **56**, 889 (1986) *Dynamic Scaling of Growing Interfaces.*

Danksagung

An erster Stelle gilt mein Dank Herrn Prof. Dr. H. Dosch, der es ermöglichte, die interessante Themenstellung der vorliegenden Arbeit in einem internationalen Umfeld unter exzellenten experimentellen Bedingungen zu bearbeiten.

Herrn Prof. Dr. D. Schweitzer danke ich für die Übernahme des Koreferats.

Für die Einführung in das Gebiet der OMBE, sowie für zahlreiche Diskussionen 'der dritten Art' danke ich Herrn Dr. habil. F. Schreiber, der darüber hinaus zum Gelingen der Arbeit durch seine stets rasche Korrektur von Manuskripten beigetragen hat.

Ohne die tatkräftige Mithilfe auf einem Dutzend Strahlzeiten, bei Arbeiten im Labor, an der OMBE, am AFM, oder bei der Aufbereitung von Daten wäre diese Arbeit nicht möglich gewesen. Dafür danke ich (in alphabetischer Reihenfolge) Dr. Esther Barrena, Helmar Bender, Dr. Christian Ern, Bärbel Krause, Dr. Volker Kruppa, Oriol Osso, Dr. Ken A. Ritley, Stefan Sellner, Vyom Sharma und Ulrike Täffner. In diesem Zusammenhang gilt mein besonderer Dank Frau Marion Kelsch für ihren unermüdlichen Einsatz bei der Preparation von TEM-Proben, ihren 'unerschütterlichen Pessimismus' vor den Messungen und die darauf doch stets folgenden hervorragenden Ergebnisse bei den TEM-Messungen.

Herr Frank Adams und die Mitarbeiter der Werkstätten von MPI und ITAP haben durch ihre flexible und kompetente Hilfe so manches technische Problem in kürzester Zeit gelöst, wofür ich mich bei ihnen bedanken möchte.

Bei der Röntgenstrahlzeit an der ESRF in Grenoble haben Dr. Bernd Struth und Dr. Oleg Konovalov an der Beamline ID10B für einen reibungslosen Messablauf gesorgt. Dr. Oliver H. Seeck war bei den Röntgenstrahlzeiten am W1 in Hamburg ein sehr kompetenter Ansprech-

partner. Dafür möchte ich den genannten Personen danken.

Prof. Dr. H-D. Carstanjen, sowie die Mannschaft vom Pelletron Stuttgart haben mich bei den RBS-Messungen sehr tatkräftig unterstützt, wofür ich ebenfalls sehr dankbar bin.

Prof. Dr. N. Karl, Dr. M. Münch, S. Hirschmann und C. Herb vom Kristallabor der Universität Stuttgart danke ich für die Gradientensublimation der DIP-Moleküle und anregende Diskussionen über das Gebiet organischer Halbleiter.

Bei Frau U. Mennicke möchte ich mich für fruchtbare Diskussionen zu Fits des gesamten spekulären Rods im Rahmen des semi-kinematischen Formalismus' bedanken.

Herrn Prof. Dr. V. Holý danke ich für die Bereitstellung des Programms XRR3 zur Berechnung der diffusen Streuintensität und für zahlreiche Diskussionen der Ergebnisse aus diesem Programm.

Besonders möchte ich mich bedanken bei Herrn Prof. Dr. J. Krug für die ausgiebige und sehr fruchtbare Diskussion der Wachstumsexponenten in DIP. Seine langjährige Erfahrung auf diesem Gebiet ermöglichte eine in sich schlüssige Interpretation der zunächst ungewöhnlichen Daten.

Last but not least danke ich denjenigen Personen, die das englische Manuskript zu dieser Arbeit (teilweise mehrmals) auf Rechtschreibfehler und 'typisch deutsche' Ausdrucksweise hin akribisch unter die Lupe genommen haben. Seine Qualität hat sich durch die Arbeit von Gerd und Rudolf von Glinsky, Anke und Mark McCown, sowie Earl Rosenbaum entscheidend verbessert. Um die deutschen Teile haben sich ferner Prof. Dr. G. H.-K. Dürr und Claudia Kutter verdient gemacht.